ACTIONNEURS EN POLYMÈRE CRISTALLINS LIQUIDES POREUX

Par

Jie Jiang

Thèse présentée au Département de chimie en vue

de l'obtention du grade de docteur ès sciences (Ph.D.)

FACULTÉ DES SCIENCES

UNIVERSITÉ DE SHERBROOKE

Sherbrooke, Québec, Canada, Septembre 2023

POROUS LIQUID CRYSTAL POLYMER ACTUATORS

by

Jie Jiang

A Thesis

Presented to the Département de Chimie

in Partial Fulfillment of the Requirements for the Degree of

Doctor of Philosophy (Ph.D.)

FACULTÉ DES SCIENCES

UNIVERSITÉ DE SHERBROOKE

Sherbrooke, Québec, Canada, 29th Septembre 2023

September 2023

le jury a accepté la thèse de madame Jie Jiang

dans sa version finale

Membres du jury

Professeur Yue Zhao

Directeur de recherche

Département de chimie, Université de Sherbrooke

Professeure Audrey Laventure

Évaluatrice externe

Département de chimie, Université de Montréal

Professeur Patrick Ayotte

Évaluateur interne

Département de chimie, Université de Sherbrooke

Professeur Pierre Harvey

Évaluateur interne

Département de chimie, Université de Sherbrooke

Professeur Jean-Philippe Bellenger

Président-rapporteur

Département de chimie, Université de Sherbrooke

SOMMAIRE

Les actionneurs en matériaux souples possèdent des caractéristiques distinctives qui les rendent utiles pour de nombreuses applications. Parmi les matériaux souples à des fins d'actionnement, les élastomères cristallins liquides (LCE - abréviation en anglais) sont particulièrement prometteurs en raison de leur grande déformation réversible, de leur importante force mécanique lors de l'actionnement, et de leurs mouvements diversifiés déclenchés par des stimuli. Dans ce domaine de recherche, la plupart des efforts ont été consacrés à la conception de nouvelles structures moléculaires de LCE, au contrôle de l'alignement LC qui est crucial pour la déformation, et à l'ingénierie des structures ou architectures d'actionneurs. Toutefois, tant pour la recherche fondamentale que pour les applications, il est important de développer de nouvelles approches qui, sans changer les structures du LCE et de l'actionneur et en utilisant le même alignement LC, peuvent donner lieu à de nouvelles fonctions d'actionnement. C'est le but de la présente thèse qui porte sur le développant d'un nouveau type d'actionneurs, à savoir, actionneurs poreux en LCE.

Afin de fabriquer des actionneurs LCE poreux, nous avons développé une méthode simple et efficace qui consiste à, successivement, disperser des nanoparticules inorganiques (celles du $CaCO_3$ et du MOF : metal-organic framework) dans un film LCE, préparer l'actionneur par étirement mécanique pour l'alignement des mésogènes et irradiation à la lumière UV pour la réticulation du polymère, et enlever les nanoparticules inorganiques de la matrice LCE par voie de gravure chimique. Nos études sur les actionneurs LCE poreux résultants ont non seulement révélé de nouvelles fonctions ou fonctionnalités d'actionnement, mais aussi démontré leur potentiel pour des applications.

Premièrement, bien que le LCE utilisé soit hydrophobe, son actionneur poreux est capable d'absorber une grande quantité d'eau et gonfler comme un hydrogel. L'étude montre que ce changement de propriété est probablement causé par des ions restants dans l'actionneur

gravé, ce qui améliore l'affinité entre les surfaces des pores et les molécules d'eau. Malgré la présence d'eau, l'alignement des mésogènes peut être préservé en grande partie. Par conséquent, l'actionneur LCE poreux gonflé peut présenter une déformation réversible par changement de volume lors de l'absorption et de la désorption d'eau (comme un hydrogel) ou par une transition de phase ordre-désordre des mésogènes induite thermiquement (une caractéristique de LCE). Des comportements en actionnement particuliers peuvent être obtenus en combinant ces deux mécanismes d'actionnement différents. Cette nouvelle fonctionnalité est abordée dans les chapitres 2 et 4.

Deuxièmement, le gonflement important de l'actionneur poreux dans l'eau offre un moyen efficace pour introduire dans l'actionneur un additif dissous dans l'eau, et après séchage, l'additive ainsi encapsulé par les canaux de pores peut doter l'actionneur d'une fonction au-delà de l'actionnement. Nous avons démontré une nouvelle fonctionnalité dite « reconfigurabilité des fonctions » en chargeant, lavant et rechargeant trois différents additifs fonctionnels dans un même actionneur LCE poreux : un liquide ionique (IL) pour la conductivité ionique, un colorant photothermique pour le mouvement piloté par la lumière et un fluorophore pour l'émission de couleur. Cette nouvelle fonctionnalité est rapportée au chapitre 2. De plus, nous avons utilisé un actionneur LCE poreux contenant un liquide ionique (PLCE-IL) pour démontrer séparément la détection et l'actionnement qui sont normalement deux fonctions obtenues avec deux classes de matériaux : matériaux déformables pour détection par voir électrique et matériaux souples pour actionnement déclenché par des stimuli. D'une part, lors de la transition de phase ordre-désordre des mésogènes alignés, le PLCE-IL se comporte comme un actionneur typique capable de changer sa forme de manière réversible et peut être utilisé pour assembler un robot souple alimenté par la lumière. D'autre part, à des températures en-dessous de la transition de phase, le PLCE-IL est un élastomère qui peut supporter et détecter de grandes déformations de divers modes ainsi que des changements de conditions environnementales en signalant la variation de

résistance électrique correspondante. L'utilisation collective de ces deux fonctions intégrées dans un dispositif a également été montrée. Ce travail est discuté au chapitre 3.

Finalement, rapporté au chapitre 4, nous avons fait une découverte inattendue en étudiant les actionneurs LCE chargés de MOF (LCE-MOF). Après gravure chimique pour le retrait des cristaux MIL-88A, l'actionneur poreux devient magnétiquement sensible, réagissant à un aimant proche. L'analyse suggère la formation in situ de nanoparticules magnétiques de Fe_3O_4 due à la gravure chimique et à l'irradiation par la lumière UV. En plus des fonctionnalités susmentionnées, un actionneur poreux magnétique peut être dirigé par un aimant d'entreprendre des mouvements multidirectionnels à la surface de l'eau. En plus, la présence des nanoparticules de Fe_3O_4 donne un important effet photothermique qui peut être mis à profit pour obtenir un mouvement efficace de l'actionneur poreux alimenté par la lumière.

Mots-clés : Élastomère cristallins liquides, polymère poreux, actionneurs souples, changement de forme réversible, matériau stimulables, capteurs déformables, hydrogel.

ABSTRACT

Soft materials-based actuators possess distinctive characteristics making them useful for applications in many fields. Among the soft materials for actuation, liquid crystalline elastomers (LCEs) stand out owing to their unique actuation features including large shape deformation, high mechanical forces, and diversiform movements driven by variety of stimuli. In terms of material research in the field of LCE actuators, understandably, most effort has been dedicated to designing new molecular structures of LCE, controlling LC alignment, and engineering actuator structures or architectures. However, it is of fundamental interest to develop new approaches that, without changing the LCE and actuator structures and using the same LC alignment, can give rise to new actuation functions. The purpose of the present thesis is to address this important issue by developing porous LCE actuators.

To fabricate porous LCE actuators, we developed a simple and efficient direct templating method that consists in dispersing inorganic nanoparticles, like $CaCO_3$ and MIL-88A (metal-organic framework, MOF) in LCE film, preparing the actuator through mechanical stretching for alignment of mesogens and UV light irradiation for polymer chain crosslinking, and subsequently removing inorganic nanoparticles from the LCE matrix by means of chemical etching. Our studies of porous LCE actuators not only revealed a number of new actuation functions but also demonstrated the potential for applications.

First, although the LCE used is hydrophobic, porous LCE actuators can absorb large amounts of water and swell like hydrogel, which is likely due to ions remained in the etched actuator leading to improved affinity between pore surfaces and water molecules. Despite the presence of water, the alignment of mesogens can be preserved to a great extent. Consequently, swollen porous LCE actuator can exhibit reversible deformation through either volume change upon water absorption and desorption (like hydrogel) or thermally induced order-disorder phase transition of the mesogens (characteristic of LCE). Unusual actuation

behaviors can be obtained by combining these two different actuation mechanisms. This new feature is discussed in Chapters 2 and 4.

Secondly, by dissolving a given active additive in water, the large swelling of porous LCE actuator in water provides an effective means to introduce this additive in the actuator and thus endow it with a beyond-actuation function enabled by the additive embedded in pore channels after drying. We demonstrated the new feature of function reconfigurability by loading, washing out and reloading different functional additives in a same porous LCE actuator: an ionic liquid (IL) for ionic conductivity, a photothermal dye for light-driven movement and a fluorophore for color emission. This new feature is reported in Chapter 2. Furthermore, we went on to use porous LCE actuator containing ionic liquid (PLCE-IL) for separate sensing and actuation that are normally two functions obtained with two classes of materials: electrically responsive and deformable materials for sensing and soft active materials for stimuli-triggered actuation. On one hand, upon the order–disorder phase transition of aligned mesogens, PLCE-IL behaves like a typical actuator capable of reversible shape change and can be used to assemble light-fueled soft robot. On the other hand, at temperatures below the phase transition, PLCE-IL is an elastomer that can sustain and sense large deformations of various modes as well as environmental condition changes by reporting the corresponding electrical resistance variation. The collective use of the two functions integrated in one device was also shown. This work, discussed in Chapter 3, shows that electrically responsive porous LCEs are a potential materials platform that offers possibilities for merging deformable electronic and actuation applications.

Finally, reported in Chapter 4, we made an unexpected finding in studying MOF-loaded LCE actuators (LCE-MOF). After chemical etching for removal of MIL-88A crystals, the porous LCE-MOF actuator becomes magnetically responsive. The characterization results suggest the in-situ formation of magnetic Fe_3O_4 nanoparticles due to acid etching and UV light irradiation. In addition to the aforementioned features of porous LCE actuators, with

a magnetic LCE actuator, a magnet can be used to drive its multi-directional movement on water surface, and the enhanced photothermal effect due to light absorption of Fe_3O_4 nanoparticles can be taken advantage to achieve efficient light-driven locomotion of the porous actuator.

Keywords: Liquid crystalline elastomer, porous polymer, soft actuators, reversible shape change, Multi-stimuli-responsive material, deformable sensors, hydrogel-like swelling

ACKNOWLEDGMENTS

PhD's career is coming to an end. Every step I have taken in these years could not have been achieved without the support and encouragement of my supervisors, friends, colleagues, and family.

First and foremost, I would like to express my sincere gratitude to my supervisor, Prof. Yue Zhao, for his continuous support, invaluable advice and tutelage during my graduate study. I am privileged to have the opportunity to pursue my study under his supervision. His profound knowledge, keen insight and enthusiasm for scientific research, as well as his patience and charming personality, have benefited me greatly in all time of my academic research and further development.

I would also like to offer my sincere gratitude and respect to Prof. Jean-Philippe Bellenger, Prof. Patrick Ayotte, and Prof. Pierre Harvey for being my committee members and serving in the jury. I also want to offer my sincere appreciation to Prof. Audrey Laventure (Université de Montréal) for being my external expert in my thesis jury. I would like to thank all the professors and staff of the Department of Chemistry at the Université de Sherbrooke, for their kind help and great support. I would like to acknowledge Dr. Daniel Fortin for his assistance in conducting XRD measurements.

I would like to acknowledge all my group members and colleagues who helped me in various ways in both life and study: Mrs. Xia Tong, Dr. Feijie Ge, Dr. Liangliang Dong, Dr. Li Han, Prof. Feng Li, Dr. Farhad Farnia, Dr. Lu Yin, Dr. Shuyun Zhuo, Mr. Ruidong Cheng, Ms. Yaoyu Xiao, Mr. Zhichao Jiang, Mr. Yiming Chen, Ms. Nina Ravandi, Ms. Yaru Ma, Mr. Junbo Hou, Ms. Niloofar Zamanian, Ms. Xinshi Chen, Ms. Meng Liu, Mr. Zepin Liu, Mr. Long Xu, Mr. Xiaofeng Zheng, Ms. Xinyi Wan, Mr. Jérémy Baribeault-St-Germain and Mr. Mohamed Azmi Ben Kmicha.

I am deeply grateful to acknowledge the financial support from China Scholarship Council (CSC), Natural Sciences and Engineering Research Council of Canada (NSERC), le Fonds de recherche du Québec: nature et technologies (FRQNT), and Université de Sherbrooke for awarding me scholarships that support my study and encourage me in life. I also thank the staff of the Education Office of the Consulate General of China in Montreal for their assistance.

Finally, my sincere thanks also go to my parents, and relatives for their unconditional love and invaluable encouragement throughout my study these years.

TABLE OF CONTENTS

LIST OF ABBREVIATIONS

LC: liquid crystal

LCP: liquid crystal polymer

LCNs: liquid crystal networks

LCEs: liquid crystal elastomers

PLCE: porous liquid crystal elastomer

T_{LC-iso}: liquid crystal-isotropic phase-transition temperature

T_{NI}: nematic-isotropic phase transition temperature

T_g: glass transition temperature

$\triangle H_{NI}$: nematic-isotropic phase transition enthalpy

AZO: azobenzene

UV: ultraviolet

NIR: near infrared

CNTs: carbon nanotubes

LMs: liquid metals

ILs: ionic liquids

TPE: tetraphenylethylene

AIE: aggregation-induced emission

MOF: metal-organic frameworks

RH: relative humidity

BCPs: block copolymers

IPN: interpenetrating polymer network

PS: polystyrene

PEO: polyethylene oxide

THF: tetrahydrofuran

PE: polyethylene

PP: polypropylene

PLLA: poly(L-lactide)

PLGA: poly(lactide-co-glycolide)

PNaSS: poly(styrene/sodium pstyrene sulfonate)

PC: polycarbonate

PCL: polycaprolactone

PMMA: poly(methyl methacrylate)

PMAA: poly(methacrylic acid)

MF: melamine formaldehyde

$CaCO_3$: calcium carbonate

ZnO: zinc oxide

NaCl: sodium chloride

TiO_2: titanium dioxide

Fe_3O_4: iron oxide black

PAA: peracetic acid

5CB: 4-cyano-4’-pentylbiphenyl

8CB: 4-octyl-4'-cyanobiphenyl

$BMIMBF_4$: 1-butyl-3-methylimidazolium tetrafluoroborate

BHHBP: 4,4’-bis(6-hydroxyhexyloxy)-biphenyl

6HCA: 4-(6-hydroxy-hexyloxy) cinnamic acid

PSA: phenylsuccinic acid

PTFE: polytetrafluoroethylene

XRD: X-ray diffraction

DSC: differential scanning calorimetry

FTIR-ATR: Fourier transform infrared-Attenuated total reflectance

DMA: dynamic mechanical analysis

EDX: energy-dispersive X-ray

EDS: energy-dispersive spectroscopy

SEM: scanning electron microscopy

EIS: electrochemical impedance spectroscopy

TGA: thermogravimetric analysis

LIST OF FIGURES

Figure 1a shows the chemical structures of the materials used for the MOF-loaded LCE actuator main chain liquid crystal elastomer (LCE). The MIL-88A was synthesized using a surfactant-assisted method.[21] Elongated hexagonal bipyramidal MIL-88A nanocrystals were prepared by heating a mixture of $FeCl_3 \cdot 6H_2O$, fumaric acid and poly(vinylpyrrolidone) (PVP) as surfactant in N,N-dimethylformamide (DMF) at 85 ºC for 2 h. The characterization results are shown in Figure S1. As analyzed from SEM images, the crystals have an average size of 680 ±100 nm in length and 540 ± 80 nm in width. As expected, XRD and infrared spectroscopic measurements show swelling of the crystals when immersed in water, corresponding to the characteristic transition from closed to the open form of MIL-88A.[22] Their porosity was measured through BET isothermal adsorption and desorption of nitrogen gas, and the results indicate a distribution of pore sizes in the synthesized MIL-88A ranging from 9 nm to 83 nm and around 47 nm for the majority. As for the LCE bearing biphenyl mesogens and cinnamyl comonomer units for photo-

LIST OF TABLES

Chapter 2

LIST OF EQUATIONS

CHAPTER 1. INTRODUCTION

In living system, vivid examples range from plants to animal world, possess the ability to react to naturally varying environmental conditions, adapting their structure and functionality to suit these changes by using complex sensing mechanisms, actuating and regulating functions, and feedback control systems. These natural systems have inspired researcher to develop new materials and applications, and to create materials with dynamic and tunable properties, mimicking the active microenvironment. (1) Smart materials or stimuli-responsive materials becomes the most blossoming fields in material science, because these materials can change their shape in response to various types of stimuli and thus perform mechanical motions and produce interesting and useful work nano-, micro-, and macroscales, making them used in potential applications in numerous fields. (2, 3) To match the performance of actuators, sensors, and displays in practical applications, the smart materials have to meet the certain requirements, including the ability of controllable and rapid deformation in response to external stimuli, safe and flexible textile for human-machine interaction.

Among all smart materials, liquid crystalline polymers (LCPs) are promising candidate to construct complex control systems. Liquid crystalline networks (LCNs) or liquid crystalline elastomers (LCEs) are materials where a macroscopically oriented liquid crystal (LC) phase is fixed within a crosslinked polymer network. These LCEs (including LCNs hereafter) have the ability to perform stimuli-induced LC-isotropic (ordered-to-disordered) phase transition and, as a result, exhibit large, reversible, and highly robust reversible shape changes. Based on the well-established chemistry for building LCE and actuation mechanisms, many ideas and design of LCE-based actuators are derived from bio-inspired, mimicking the sophisticated movements of natural creatures, which further transfers the dynamitic and reversible shape deformations into macroscopic motions. (4-7) In this regard,

studies in this field have sought to explore novel intelligent actuators with new actuation behaviors, functions, and applications.

To this end, porous polymers, combining advantages of porous structures and polymeric materials, gained significant attention as they offer a wide spectrum of application, such as separation membrane, battery separator, solid catalyst and sensor supports. (8, 9) Therefore, these high-value applications drive the recent emphasis on the development of reliable methods for preparation of porous polymers, with designed pore structures. Throughout the literatures, porous polymers are in many cases more advantages than solid materials. Moreover, porous structure provides an easy incorporation of multiple functional materials with different properties in three-dimensional space.

This thesis deals with porous LCE actuators. We expected that the presence of pores could generate novel actuation behaviors and functions compared with their non-porous counterparts. This approach, essentially unknown in the literature, involves no LCE design and synthesis and no actuator structure engineering either, to which most research efforts have dedicated in the field. If the approach is successful, it is of fundamental interest by opening a new avenue towards the development of LCE actuators. In what follows, we will give a brief introduction to the various topics and subjects involved in the thesis.

1.1 Dielectric Elastomer Actuator

An actuator is a functional element that connects the information processing part of an electronic control system. Generally, an actuator can be made as a mechanical device used to move or control the motion of a mechanic system. Traditional actuators include pneumatic actuators, electronic actuators, motors, and hydraulic cylinders. (10) To meet the requirements of light weight, small size, and multiple-shape for emerging application applications, new alternative actuating technologies and materials need to be developed. (11) Among the many types of actuators based on different materials and mechanisms, actuators on elastomer (soft polymer with crosslinked chains or a network structure) have been

attracting broad and growing interest in recent years, since they are the best candidates for applications in biomedical, artificial muscle and soft robotics fields. To date, most actuators utilize dielectric elastomers (DE), which are a type of electroactive polymers (EAP, defined as polymers with the ability to change the mechanical properties in response to an electrical stimulation). (12) The working mechanism of dielectric elastomer actuator (DEA) is illustrated in Figure 1. A dielectric elastomer film is sandwiched by two complaint electrodes coated on it, forming a plate capacitor. When a high voltage (thousands of volts) is applied across the complaint electrodes, the electrostatic attraction between the opposite charges on the two electrodes generates an electrostatic stress or pressure acting on the elastomer, resulting in its contraction in thickness and expansion in plane. Due to the rubbery (entropic) elasticity, the deformation is reversible, meaning that the elastomer returns to its original shape after removing voltage. When an AC field is used, the DEA can execute cyclic deformation at a high frequency.

The electrostatic pressure, also known as the Maxwell stress p, generated under the effect of a high voltage, is defined as the change in electrostatic energy U, per unit area, A, per unit displacement of the film in the thickness direction, z (the negative sign indicates that the generated stress is compressive):(13, 14)

$$p = (\frac{1}{A})(-\frac{dU}{dz}) \qquad 1.1$$

Since the elastomers are largely incompressible (*i.e.*, deformation results in no volume variation, with Poisson's ratio (the ratio of transverse contraction strain to longitudinal extension strain in the direction of the stretching force) close to 0.5), any decrease in thickness leads to a concomitant increase in planar area. From analysis of the interaction between the two electrodes in plate capacitor, the electrostatic pressure acting on the elastomer film in an DEA is related to the electric field strength E through:

$$p = \varepsilon_0 \varepsilon_r (\frac{V}{z})^2 = \varepsilon_0 \varepsilon_r E^2 \qquad 1.2$$

Equation 1.2 relates the actuation pressure p to the relative electric permittivity (*i.e.*, dielectric constant) $\mathcal{E}_r$ of the elastomer, the permittivity of volume $\mathcal{E}_0$, the applied voltage V, and the film thickness z.

Using Hooke's Law to describe the length change of an elastomer with Young's modulus (a measure of the ability of a material to withstand changes in length when under lengthwise tension or compression) Y in response to external stress, the electrostatic pressure includes a compressive strain in thickness s_z of the elastomer:

$$s_z = -\frac{p}{Y} = -\frac{\varepsilon_0 \varepsilon_r E^2}{Y} = -\frac{\varepsilon_0 \varepsilon_r}{Y}\left(\frac{V}{z}\right)^2 \qquad 1.3$$

Although the equation for actuation stress is based on a simple case under a linear elasticity and small strain (< 20%), it shows the influence of the electrical and mechanical properties of elastomer film on the performance of DEAs. In principle, low elastic moduli, combined with low viscosity and electrical conductivity, high dielectric constant and breakdown strength lead to large actuation strain of DEA. (15, 16)

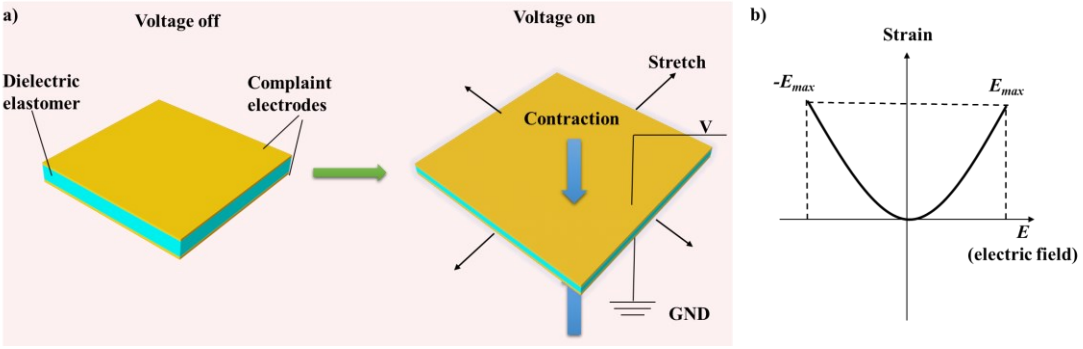

Figure 1. a) Schematic showing the working principle of dielectric elastomer actuators (DEAs). Dielectric elastomer layer contracts in thickness and expands in area when a voltage is applied across the film. b) Typical thickness or planar strain in response to applied electric field for a film with no external loads. (E_{max}: maximum field before breakdown or saturation) Reproduced with permission. (13) Copyright 2009, Wiley-VCH.

1.2 Liquid Crystal Elastomer Actuator

More recently, another type of elastomer actuator has emerged, called liquid crystal elastomers (LCEs) actuator, which combines the characteristic rubbery elasticity of elastomers and molecular order of liquid crystals (LCs). The working mechanism of LCE actuator is based on polymer chain conformation change associated with order-disorder phase transition, which is totally different from DEA. Before discussing the parameters or factors that determine the reversible actuation deformation of LCE, a brief introduction to LCs is given below using Figure 2, where the difference between LC and crystal, the typical LC phases, and the incorporation of mesogens (moieties forming the LC phases) in the polymer (elastomer) structure are depicted.

A liquid crystal (LC) is identified as a state of matter that exhibits both the order of solid crystals and the fluidity of liquids, possessing a degree of long-range molecular order (Figure 2a). It is also referred as mesophase or intermediate phase.(17, 18) The LC states are true thermodynamic stable states of matter like solids, liquids and gases. For this reason, their specific state endows them with anisotropic optical, electrical, magnetic, and mechanical properties. Normally, the fundamental structures of LCs are comprised of rigid molecules (aromatic rings), called mesogens referring to self-organized properties, and flexible ends contributing to liquid crystallinity by allowing mesogens to reorient themselves easily while flowing. (19) In ordered states, mesogens self-organize into the orientated arrangement, showing anisotropic properties. Conversely, in disordered states, mesogens are randomly aligned, resulting in an isotropic behavior. This transition phase takes place at the LC-to-isotropic phase transition temperature, denoted by T_{LC-I}, also called clearing temperature. How this order-disorder transition happens depends in part on the general category the liquid crystal falls into. The common classification is based on how the LC phase is formed, and has LCs divided into two categories: 1) thermotropic LCs, for which the LC phase is formed upon temperature change, either by heating the crystalline solid or by

cooling an isotropic liquid, and 2) lyotropic, where the LC order is obtained by dissolving amphiphilic compounds in appropriate solvents over a range of concentrations and temperatures. Most of the research related to LCs is carried out around thermotropic LCs of rod-like molecules, although disc-like and bent-core compounds are also of great interest. Schematically depicted in Figure 2 are three common LC phase: nematic, smectic and cholesteric phase. In the nematic phases, the mesogens show long-range orientational order at one dimension (1D), with their long molecular axes trending to be parallel to the director ***n***, without position order. The smectic phases exhibit both 1D orientational and 2D positional order, that is, mesogens are packed in layers in addition to the nematic order. Although there are various smectic phases with different extents of order, the most common is the sematic A phase shown in Figure 2b. (20, 21) As for the cholesteric phase, also called chiral nematic phase, the mesogens form nematic order in layers, with their directors rotating from layer to layer to form a helical suprastructure that can reflect light through a photonic crystal. The reflected wavelength of light (λ) is given by the following equation, (22)

$$\lambda = nP \sin \alpha \qquad 1.4$$

where n is the average refractive index of the material, P is the pitch of the helix, and α is the angle between the reflected light and the helical axis.

Obviously, combining the low-molecular-mass LCs and the long-chain polymers through chemical coupling may give rise to interesting materials. Indeed, liquid crystal polymers (LCPs) have been extensively studied over the past decades. LCE is crosslinked LCP with a low T_g (around or below room temperature), whose use as actuator is subject of this thesis. To make LCE, mesogens can be introduced in the polymer structure in different manners according to their position (Figure 2c). In main-chain LCE, the mesogens are part of the chain backbone and are separated by flexible segments, whereas in side-chain LCE, the mesogens are grafted to chain backbone via a flexible spacer either at their ends (end-on) or their sides (side-on). (17, 23) The way of attachment between the mesogens and polymer

chain backbone may affect the LC phase of mesogens in LCE as well as its chain conformation. (20)

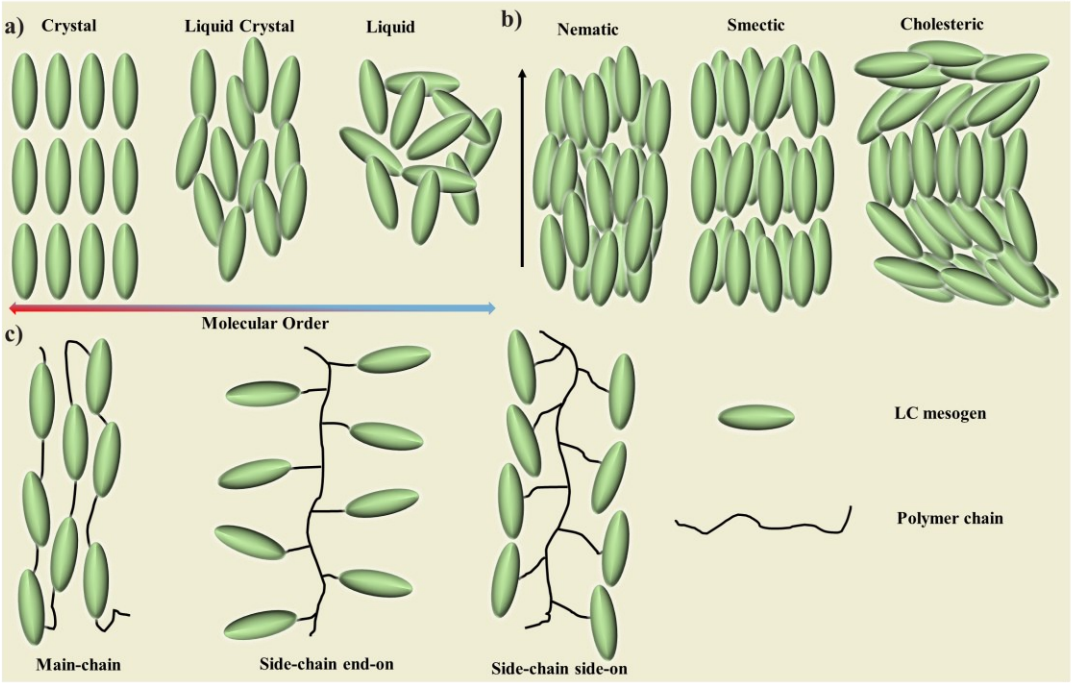

Figure 2. a) Schematic showing the orientation of molecules in the crystal, liquid crystal, and liquid state of a material with elongated molecular shape. b) Schematic showing the orientation of mesogens in nematic phases, smectic phases, and cholesteric phases. The arrow (director) shows the direction of preferred orientation. c) Schematic showing the attachment architectures of the LC phase-forming mesogens in LCE: main-chain, side-chain end-on, side-chain side-on. Reproduced with permission. (17) Copyright 2018, Taylor & Francis.

The actuation mechanism of LCE is shown in Figure 3. A crosslinked LCE with macroscopically oriented mesogens has a stable shape (rectangular strip in the example) in the LC phase, on heating to the isotropic phase, the disordering of mesogens induces a contraction along the mesogen alignment direction and concomitant extension in width and thickness of the strip. Subsequently, on cooling to the LC phase, the mesogens recover their oriented state, which brings the LCE strip back to the initial shape. This actuation

deformation is reversible, as it is determined by the reversible order-disorder phase transition of the mesogens, and can be very large (up to 500% strain) due to the conformational change of polymer chains coupled to mesogens. As depicted in Figure 3b, the schematic shows the global polymer chain conformations for main-chain LCEs. In isotropic phase the mesogens of LCE are aligned in random direction, the polymer chain backbone has a spherical random coil conformation, (24, 25) (20, 26) so that the average radii along the three axes in a coordinate system are the same ($R_x = R_y = R_z$). While in LC phase, the anisotropy of the macroscopic mesogen orientation translates into polymer chain conformation change, generating different radii of gyration parallel ($R_{/\!/}$) and perpendicular ($R_{\perp}$) to the LC director. In the prolate conformation ($R_z > R_x, R_y$), where the long axis is the radius of gyration parallel to the LC director and the two short axes are the radii of gyration perpendicular to the LC director. The polymer chain backbone orients along the LC director, meaning $R_{/\!/} / R_{\perp} > 1$. This situation is usually encountered when the main-chain LCE is uniaxially stretched to have mesogens and chain backbone orient in the same direction. Upon heating to isotropic phase, the prolate conformation undergoes a uniaxial contraction along R_z or the LC director, resulting in a random coil conformation due to the entropy elasticity of the polymer network. In the oblate conformation ($R_z < R_x, R_y$), the short axis is the radius of gyration parallel to the elongated chain backbone and the two long axes are the radii of gyration along the LC director, i.e., $R_{/\!/} / R_{\perp} < 1$. This situation usually is observed with some side-chain LCEs whose mesogens form smectic phases. Mechanical stretching of these LCEs induces alignment of mesogens perpendicular to the stretching direction. Nevertheless, there is a rare example about the oblate conformation for main-chain LCEs. (17, 20, 24) Figure 3c schematically shows the drop of order parameter across the boundaries in a nematic-isotropic phase transition. Order parameter S is a measure of the average orientation of LCs mesogens given by: (27)

$$S = \langle P_2(\cos\theta)\rangle = \langle \frac{3\cos^2\theta - 1}{2} \rangle \qquad 1.5$$

where θ is the angle between the director ***n*** and the long axis of a single LC molecule. The order parameter has values between -0.5 for perfect perpendicular orientation and 1 for perfect parallel orientation, compared to the main axis, while the absence of any macroscopic orientation corresponds to S=0 (in isotropic state or polydomain LC phase). Typically, the order parameter of nematic LCs is between 0.4 to 0.7.

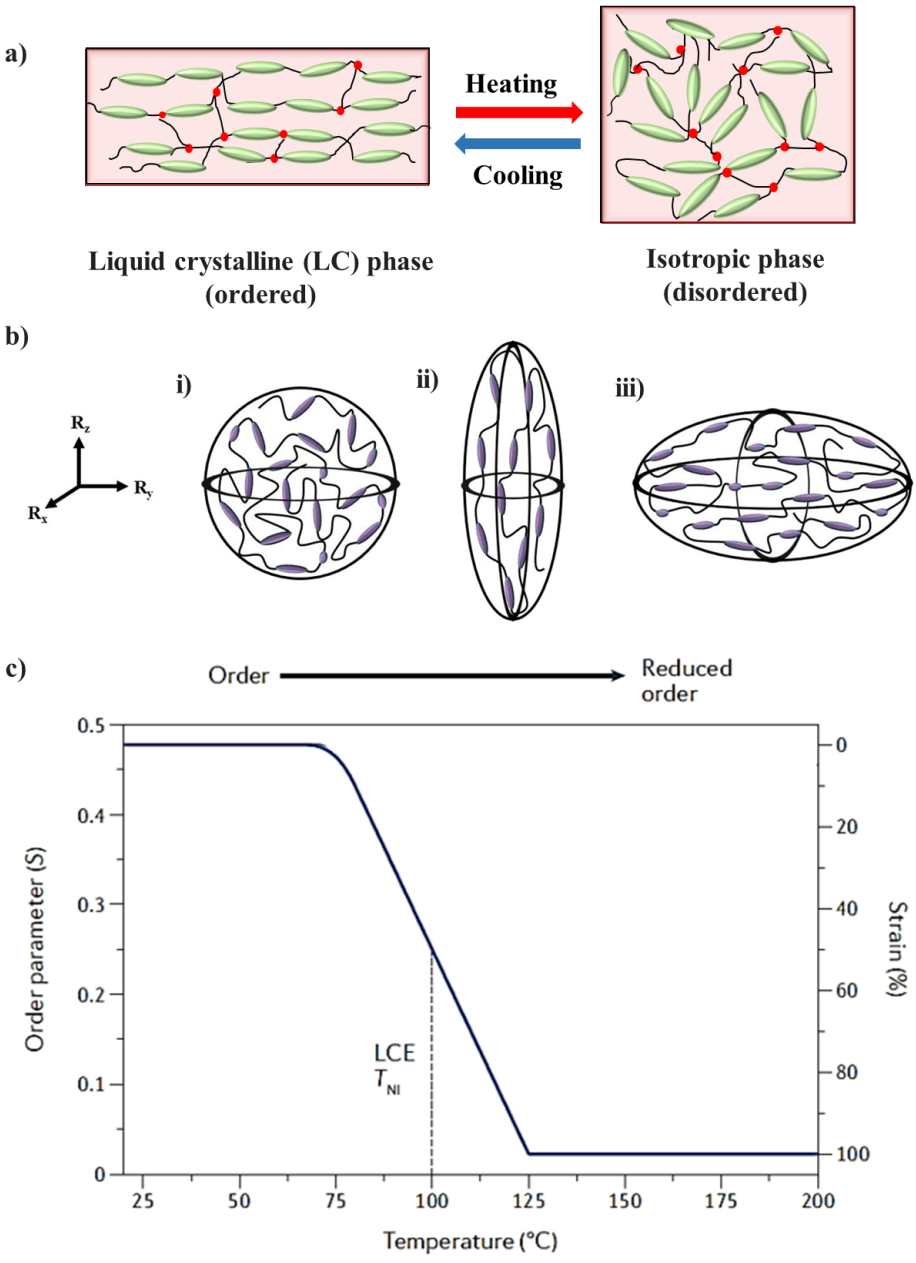

Figure 3. a) Schematic showing the thermal LC-to-isotropic phase transition (or order-to-disorder transition) of a nematic main-chain LCE. b) Polymer chain conformations for main-chain LCEs. (i) Isotropic, where $R_x = R_y = R_z$. In this conformation, mesogens may be oriented in any direction. (ii) Prolate, where $R_z > R_x, R_y$. In this conformation, the mesogens can only be oriented along R_z. (iii) Oblate, where $R_z < R_x, R_y$. Mesogens cannot be oriented along R_z, but may be randomly oriented in the R_x and R_y directions. Reprinted with permission (17) c) The relative increase in mobility increases the extent of and rate at which the order parameter is affected by the stimulus (temperature). Reprinted by permission from Springer Nature, copyright 2021. (27)

To prepare an LCE actuator, two conditions need to be fulfilled. First, mesogens must be aligned at macroscopic scale. Secondly, LCE must be crosslinked with the mesogens in aligned state, which fixes or memorizes the shape of LCE in the ordered state. Without either condition (no chain crosslinking or no mesogen alignment), no reversible deformation occurs. Generally, a freshly prepared LCE film without any treatment has a polydomain arrangement, in which a large number of submicrometric or micrometer-sized domains exist and their LC director varies from domain to domain, leading to the absence of macroscopic alignment of mesogens. (28, 29) Several methods can be employed to obtain a macroscopic alignment of mesogens like the uniaxial alignment shown in Figure 3a, called monodomain. Among them, mechanical stretching is commonly used to transform a polydomain to a monodomain arrangement of LC director. (30, 31) On the other hand, the chain crosslinking can be realized using different methods as shown in Figure 4. Figure 4a,b show the procedures for preparing the mechanical alignment of LCEs: 1) LCE compositions are first partially polymerized and applied to align the LC mesogens; 2) under strain, they are fully polymerized to fix the orientation of LC mesogens. Figure 4c shows the initial procedure to prepare aligned LCEs involved a two-step hydrosilylation reaction, which takes place through hydrosilylation of liquid crystal monomers and crosslinkers with a linear polysiloxane, using a platinum catalyst. (30) In addition, both approaches shown

in Figure 4d,e are based on chain-extension reactions, including aza- and thiol-Michael addition. These reactions are used to prepare LCEs, due to the excess of diacrylate liquid crystalline monomers, followed by a further reaction by mechanical stretching to fix the pre-alignment of LCEs. (32-34)

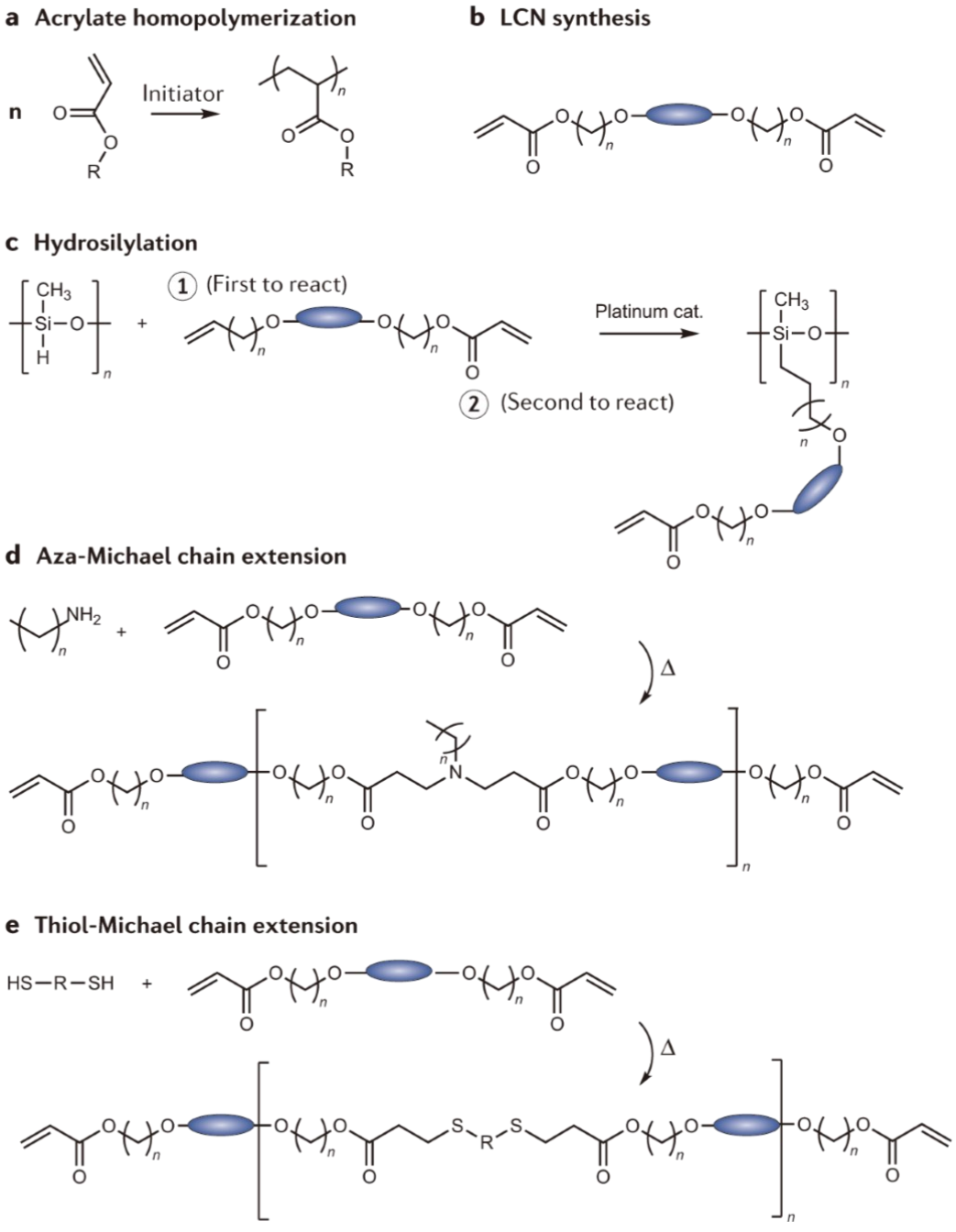

Figure 4. Synthetic approaches for the preparation of crosslinked liquid crystalline polymers and elastomers: a) and b) photoinitiated acrylate homopolymerization to prepare LCEs; c) the two-step crosslinking method consisting of a platinum-catalyzed hydrosilylation and a subsequent photoinitiated radical crosslinking, d) aza-michael oligomerization and successive photocrosslinking; e) thiol-michael chain extension and subsequent photopolymerization of residual groups. Reproduced by permission from Springer Nature, copyright 2021. (27)

Compared with conventional DEA, LCE-based actuator exhibits large strain under external stimuli-induced order-disorder phase transition and can be processed to have complex shapes used in various applications. (35) While DEA is activated only by electric field (high voltage), the actuation of LCE is governed by the thermal order-disorder phase transition that can be triggered by a variety of stimuli, including direct heating, light (via photothermal effect), electric field (Joule effect) and magnetic field (magnetothermal effect). Indeed, to efficiently drive the order-disorder phase transition of the aligned mesogens in LCE actuator, the choice of stimuli is of great importance and depends on the target application. In addition to the many choices of stimuli to drive the actuation, some of which can provide a spatial control of actuation regions in the LCE actuator (regions exposed to light spot or regions containing conducting wires or fillers for Joule heating under electric current), chain crosslinking can also be made to occur in spatially selected regions to pattern or organized the actuations domains. All these unique features of LCE actuators can be applied or combined to achieve complex shape changes and stimuli-driven movements, as shown by the few examples in Figure 5. An example shown in Figure 5a, our group firstly synthesized LCPs containing photodimerizable cinnamic acid moieties for photocrosslinking. By using photomasks to pattern crosslinking regions of the uniaxially oriented LCE sample, the nonuniform optical inscription LCE film can be transformed into versatile 2D-to-3D shape transformations via thermally induced order-to-disorder phase transition. (36) Additionally, Figure 5b shows a summary of actuation mechanisms of photo-responsive

LCEs: 1) photochemical mechanism, by introducing photoswithes or photosensitive chromophores into LCP which can undergo light-induced macroscopic shape change, for example, azobenzene derivatives exhibiting *trans-cis* photoisomerization under ultraviolet (UV)/visible light (Vis); (6, 37-40) 2) photothermal effect, by doping highly photothermal conversion agents, such as, gold nanoparticles, carbon nanotubes (CNT), graphene, and organic dyes, they convert light energy into thermal energy, releasing heat that raises the LCEs' temperature above T_{NI}, and induces mechanical shape deformation. (41-45) Moreover, photothermal and photochemical effects can be utilized simultaneously to develop light-driven bimorph liquid crystalline actuators, and both mechanisms have their own strengths. (46, 47) Among the known stimuli for actuator, moisture/humidity, as a non-polluting, renewable, convenient and efficient external actuation, Figure 5c shows a common fabrication process of humidity-responsive LCEs actuator. In this case, generally, by introducing typically hydrophilic hydrogen-bonded carboxylic acid dimers, the LCEs were pretreated by alkaline solution, forming a hydroscopic polymer salt. The active LCEs film can easily absorb water, resulting in anisotropic swelling mostly perpendicular to the alignment director. To obtain large shape deformation of humidity-responsive actuator, one side of LCEs treated by base solution faces the humidity, the anisotropic swelling of LCEs film induces bending toward the non-treated side. (48-50) Additionally, there is another type of electric-responsive LCEs, as shown in Figure 5d. In this example, electrically powered LCN actuator prepared by embedding thin resistive wire between LCE strip and a laminated Kapton layer. Using Joule heating effect to induce order-to-disorder phase transition, LCEs actuator can undergo reversible shape deformation or motion. It also can be served as an electrically powered soft robot, human-like two-leg, which can walk and push a load forward. (51) Among this example, by patterning the way of the implement of soft heaters (52, 53) or loading conductive nano-/macro-fillers, (54-56) conductive LCEs actuators were obtained, which can exhibit multi-functional shape deformation or accomplish sort of mechanical works.

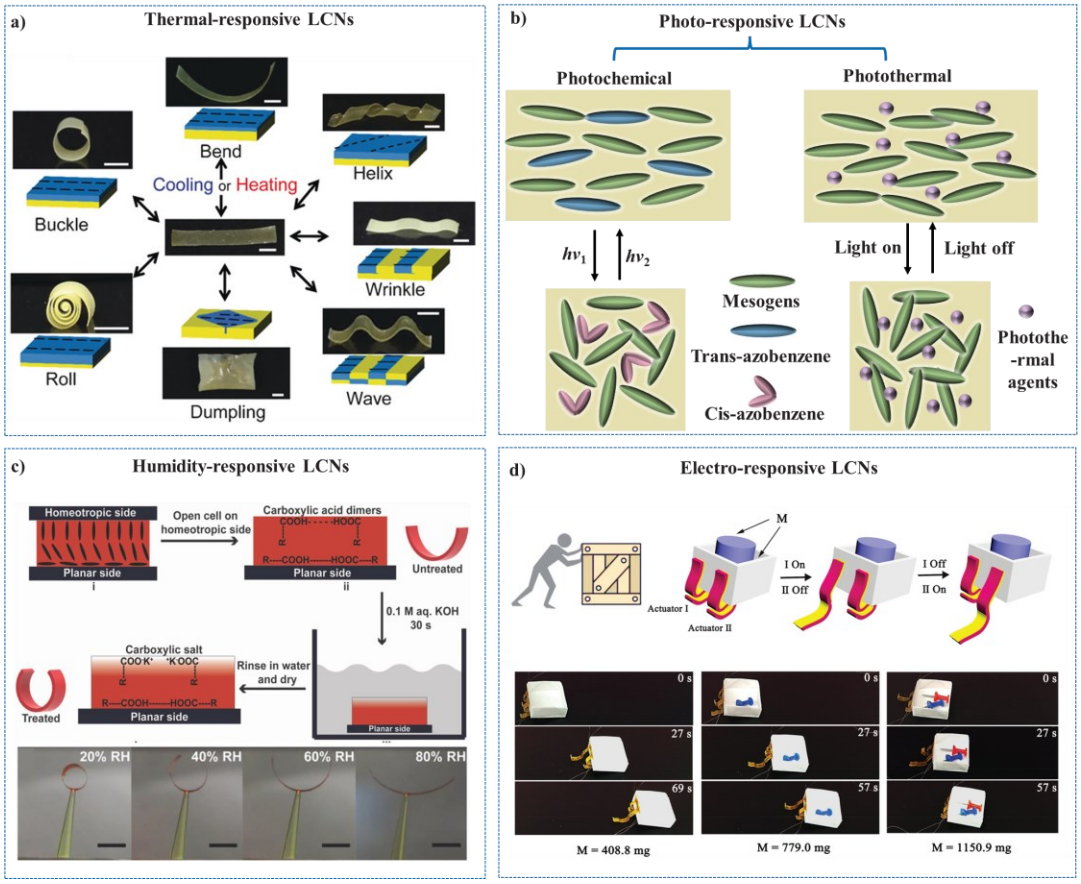

Figure 5. a) Photo showing the thermally induced complex shape morphing of LCEs with uniaxial alignment of mesogens. Reprinted with permission. (36) Copyright 2015, Spring Nature. b) Schematic showing the photochemical and photothermal actuation mechanisms of photo-responsive LCEs. c) The fabrication process of humidity-responsive LCEs actuator (Top): i) the mixture is polymerized in splay molecular alignment inside an LC cell, ii, iii) the cell is opened from the homeotropic side and dipped in 0.1 m KOH solution for 30 s, to perform base treatment selectively on the homeotropic side, and iv) the sample is rinsed with water and then dried in air. The insets in (c–ii) and (c–iv) show the schematic representation of the LCE strips, cut along the director on the planar side, at corresponding stage of fabrication under ambient conditions. Change in curvature of treated LCE strip with increasing RH (bottom). Reprinted with permission. (48) Copyright 2019, Wiley-VCH. d) Bottom: Schematic showing a conveyer that pushes an object forward by

alternating activation of two “leg”-like actuators. Top: Photographs showing the locomotion of the two-leg conveyor moving three different loads at different speeds. Reprinted with permission. (52) Copyright 2017, Wiley-VCH.

1.3 Translating Reversible Deformation and Movement

As mentioned above, if the reversible deformation of LCE actuator can be made to occur repeatedly under cyclic, on/off stimulation that induces the back-and-forth order-disorder phase transition (e.g., heating/cooling, light on/off, voltage on/off), a movement or locomotion of the actuator can be achieved. This feature has sparked the interest of using LCE actuator for soft robotics applications. To translate stimuli-triggered reversible deformation into movement, a friction bias is always required. In addition to the involved materials, LCE and the substrate in contact with the LCE, the initial geometry (shape, structure or architecture) of the actuator plays an important role. A common locomotion is the light-driven caterpillar or inchworm-like motion of LCE actuator that is enabled by reversible shape change controlled by light-driven order-disorder phase transition. The walking gaits of microwalker are influenced by various factors, including the geometry of body materials, as well as the control of friction of the film. (57, 58) Considering the strip-shaped materials commonly used in LCE-based actuator systems, the effective locomotion is mostly depending on manipulating friction, namely, the changing contact between the body materials and its environment. The friction often exerts the primary influence over the forces necessary to initiate or sustain relative motion between surfaces in contact. The gripping system of caterpillars is remarkably efficient. Each proleg's tip features a flexible membrane known as the planta, equipped with a double row of scimitar-shaped hooks called crochets, which face the center. These hooks passively grasp the surface and can be actively withdrawn during locomotion, resulting in a two-state switch that alters friction levels between low and high. (59)

Examples of soft microwalkers known in the literature are shown in Figure 6 and used to explain the basic mechanism of caterpillar locomotion. (60) Figure 6a shows a 3D-printed soft robot that mimics the movement of a caterpillar. It has a bilayer structure made of two types of soft materials, top curved surface with low friction coefficient (M_2) and bottom surface with high friction coefficient (M_1). Figure 6b depicts the variable-friction mechanism. As the soft robot deforms and lifts away from the substrate (light on), the contact angle (ψ) of foot alters, causing the slippery material M_2 to encounter the substrate (Figure 6b i-iii). When the tilt exceeds the threshold angle (ψ^*), friction decreases, allowing the rear foot to move forward (Figure 6b iii-v). After deactivating the actuator (light off), the body returns to its original shape using elastic and gravitational potential energies. As the body straightens and the foot tilt decreases below the threshold angle, friction force increases, transmitting a counteracting force forward (Figure 6b vi). If the front foot is inclined enough, this force causes the foot to slide forward. On flat or slightly inclined surfaces, the recovery phase combines gravitational potential energy and elastic recoil. This model also can be employed to multi-state, multi-material (with different friction coefficient) friction manipulation mechanisms. (60) In the LCE-based system, a bilayer structure consisting of hard passive layer (transparent polymer) and active layer (LCE actuator) is often used to achieve reversible bending away from the light upon light on and unbending after the light is turn off or moved away. For a strip LCE actuator, asymmetric bending generates different frictional force f at the two ends according to (61)

$$f = \mu F \tag{1.6}$$

where μ is the friction coefficient, F is the normal contact force. As shown in Figure 6c, when the actuator arches up by contraction, the normal force at one end is greater than at other end ($F_1 > F_2$); conversely, as the actuator relaxes, the push force parallel to the surface is greater at one side as compared to the other side ($F_4 > F_3$), causing the forward motion. It should be mentioned that light-induced order-disorder phase transition could be obtained

either through the aforementioned photothermal effect or photochemically. Figure 6d shows an example of the latter. (62) The film moves forward with alternating UV and visible light exposure at room temperature. It extends forward under UV light due to the sharp edge acting as a stationary point, and retracts from the rear side under visible light with the flat edge as the stationary point, enabling unidirectional motion. In this case, the isothermal order-disorder phase transition is induced by the reversible trans-cis photoisomerization of azobenzene mesogens upon adsorption of UV and visible light, respectively.

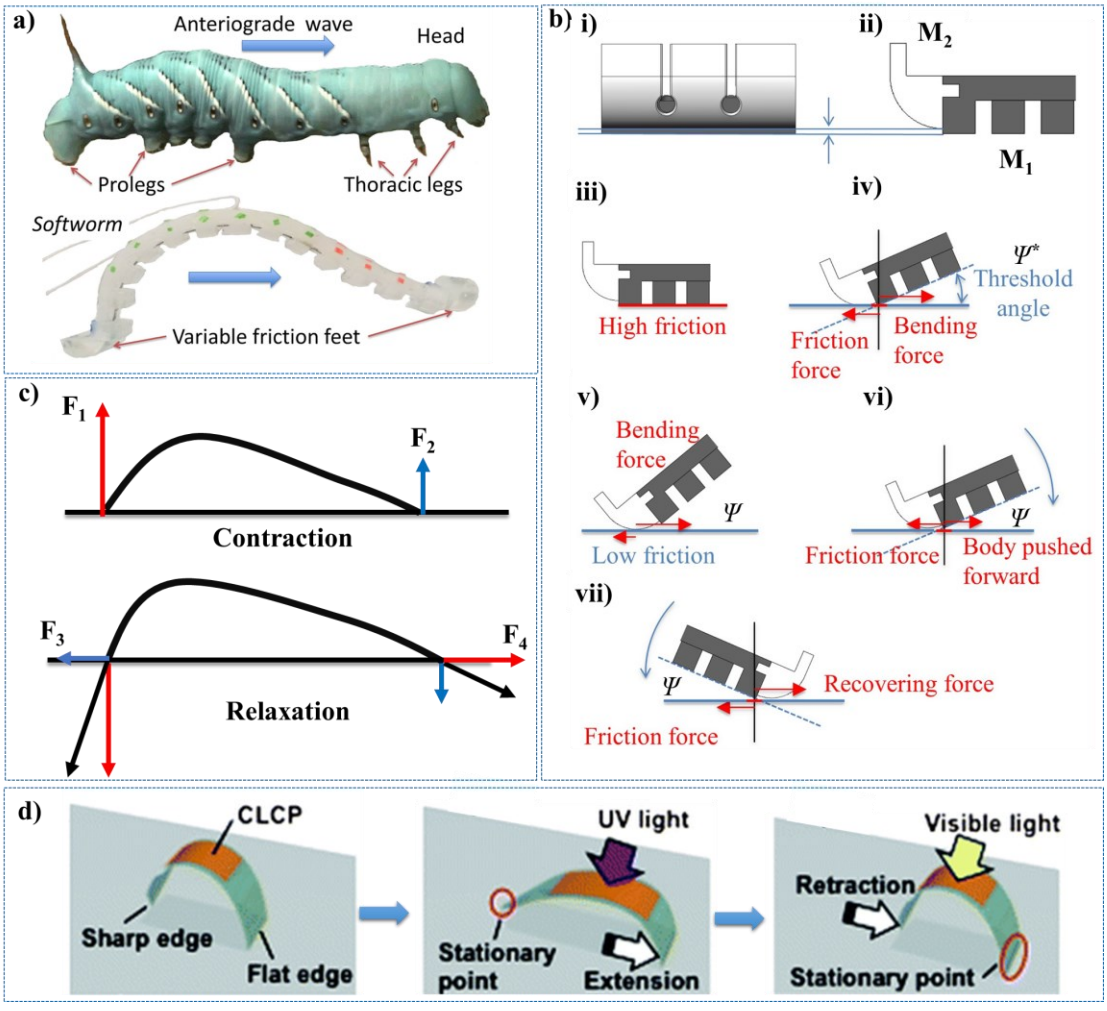

Figure 6. a) Schematic showing 3D-printed soft robots inspired by caterpillar. b) Schematic illustration of the variable friction mechanism. i) Front and ii) side view of the gripping mechanism. M_1 (black part): higher friction. M_2 (white part): made of hard material

with low friction. iii)-vi) Sequence of the friction changes to produce a crawling gait in the rear and (vii) in the front. Reprinted with permission. (60) Copyright 2016, IOP Publishing Ltd. c) Asymmetric bending and unbending of a LCE strip actuator and the corresponding normal forces and forces in the substrate plane. d) Schematic illustrations showing a mechanism of the photoinduced inchworm walk of the CLCP laminated film. Reproduced with permission. (62) Copyright 2009, Royal Society of Chemistry.

1.4 LCE Actuators with Functions beyond Deformation and Movement

As we discussed above, the primary function of LCE actuators is the reversible deformation and stimuli-controlled movement. However, recent advancements have expanded their properties beyond these core features. Researchers have been exploring and developing new functionalities that are added to the order-disorder phase transition induced deformation. Here, we discuss some of the interesting emerging functions.

The first function is self-sensing through electrical response, which is different from Joule heating induced shape change upon order-disorder phase transition. The mechanism of self-sensing of LCE actuator is the resistance-based sensing that involves detecting the variations in electrical resistance as the actuator deforms. That is, the deformation of the LCE actuator can be coupled with an electrical response due to the conductive nature of the material. As the actuator undergoes reversible shape change, the conductive fillers or metal wires embedded in the LCE materials experience variations in electrical resistance. These changes can be measured and correlated with the deformation state of the actuator, enabling a self-sensing capability. Among the notable examples, 3D printing was used to assemble liquid metal (LM) into LCE actuator with core (LM)-shell (LCE) structure (Figure 7), obtaining the LCE actuator for electrical response. (54) This conductive LCE actuator exhibits its large thermally induced actuation strain, up to 50%, while possessing self-sensing capability and closed-loop control. More specifically, Joule Heating was first obtained by applying a voltage to the LCE actuator is measured and quantitatively related to the length

variation (L/L_0) of actuator, that is, a greater contractile strain results in a greater decrease in resistance, enabling the self-sensing capability. The relative resistance change R/R_0 is determined by both the length and temperature of the actuator according to:

$$\frac{R}{R_0} = [1 + \alpha(T - T_0)](\frac{L}{L_0})^2 \quad 1.7$$

where α and T_0 are the temperature coefficient of resistivity and the initial temperature prior to voltage application, respectively. To this regard, when a control system is programmed at target R/R_0, the given current can automatically regulate in real time to adjust the real R/R_0 to conform to the programmed value versus time, which is called closed-loop control. Although different large voltages are applied on the actuator, this self-sensing and autoregulation of actuation response can resist perturbations. Apart from self-sensing properties, a recent report demonstrates another interesting function based on using an LM-loaded LCE tubular actuator, called perception, which offers possibilities for soft robots to intelligently interact with humans. (53) Therefore, by integrating self-sensing or perception capabilities into LCE actuators, it becomes possible to create autonomous systems that can perceive and adapt to their environment. This opens up avenues for applications in robotics, artificial muscles, and biomedical devices, where the actuators can not only deform and move but also sense and respond to changes in their surroundings. The combination of actuation and self-sensing in LCE actuators represents a significant step towards the development of advanced and intelligent soft materials for a wide range of technological applications.

Another intriguing function of LCE actuators is the humidity sensibility or hygroscopicity. Such actuator can detect and respond to changes in ambient humidity. In general, the mechanism for humidity sensing is based on the absorption or desorption of water vapor inducing a change in the volume or shape of LCE actuator. This deformation is a result of the swelling or contraction of the elastomer matrix in response to the varying amount of absorbed water molecules. The magnitude and direction of deformation depends on many

factors such as the LCE chemical structure, the humidity gradient, and the time of exposure. From the literature, the preparation of LCE actuators capable of humidity sensing can be divided into two categories based on the composition of LC molecules and material structure. First, LCE actuator can be made hygroscopic by introducing hydrophilic groups into the mesogens, typically using hydrogen-bonded benzoic acid mesogens.(48, 49) For example, through alkaline treatment, carboxylic acid groups are converted into carboxylates, forming a hygroscopic polymer salt (Figure 8). When the film is exposed to water vapor, the activated side of film quickly absorbs water and then expands, leading the film to bend away from the source of water vapor due to an anisotropic swelling mainly perpendicular to the LC alignment director due to weaker intermolecular interactions. (63) In another case, (50) the humidity sensitivity in LCE actuator is shown to stem from the hydration of the C=O and C-O-C groups present in the mesogens. This hydration leads to a swelling on the surface of the LCE film, which alters the alignment of the mesogens within the material and, consequently, results in the bending of the entire film along a direction perpendicular to the initial alignment direction. Moreover, it is worth mentioning a bilayer strategy developed to show various advantages such as deformation programmability and superior stability of the actuator. In this case, the hydrophilic layers are generally made with a hydrophilic polymer, like polyethyleneimine (PEI) (64) and polyamide (PA) (65, 66), while the LCE layer is not hygroscopic. Although the bilayer design is easy to understand, the delamination between two layers at the interface is a common problem that limits the use of bilayer actuators. To address this issue, a robust crosslinked system consisting of azobenzene-containing 4-arm block copolymers and high molecular weight branched PEI is designed to enhance the adhesion between LCE and PEI layers. This interface-bound bilayer actuator can bear bending driven by water absorption from PEI. The multi-H-bonds within PEI matrix also endows the actuator with self-welding ability. The humidity sensing by LCE actuator is a functionality that, combined with actuation, offers more potential applications in smart soft robots, advanced sensors, and self-adaptive actuators. (67, 68)

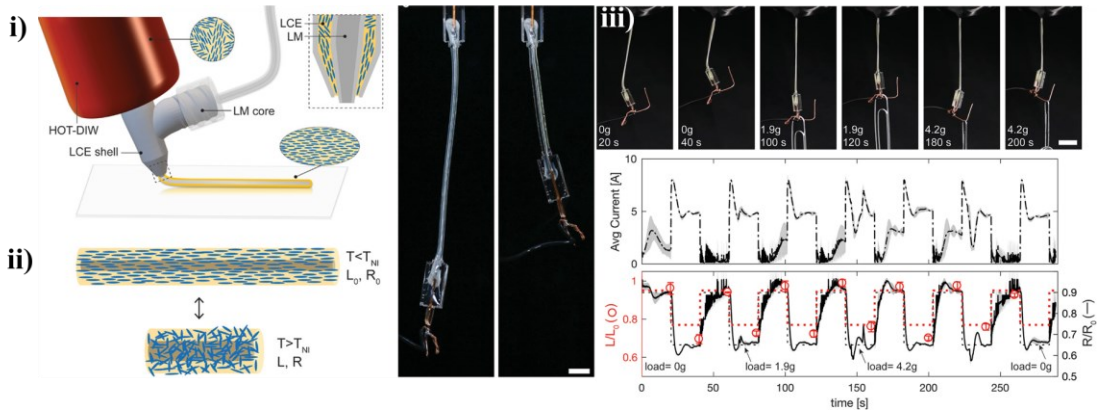

Figure 7. i) Schematic illustration of 3D printing core–shell LCE fibers composed of a liquid metal (LM) core surrounded by a LCE shell, the LC director is aligned along the print path. ii) Schematic illustration and photos showing the actuation of an LCE fiber before (left) and after (right) Joule heating above the nematic-to-isotropic transition temperature, T_{NI}. (scale bar = 5 mm). iii) Closed loop control of LCE fiber actuation. Top: photos showing the LCE fiber with self-adjusting actuation under several loading conditions (scale bar = 10 mm). Bottom: self-adjusting current profile (top) and change in resistance and actuator length (bottom) as a function of time for LCE fibers that are perturbed with bias loads, while reaching target values of resistance (black, dashed) and corresponding length (red, dashed). Reprinted with permission. Copyright 2021, Wiley-VCH. (54)

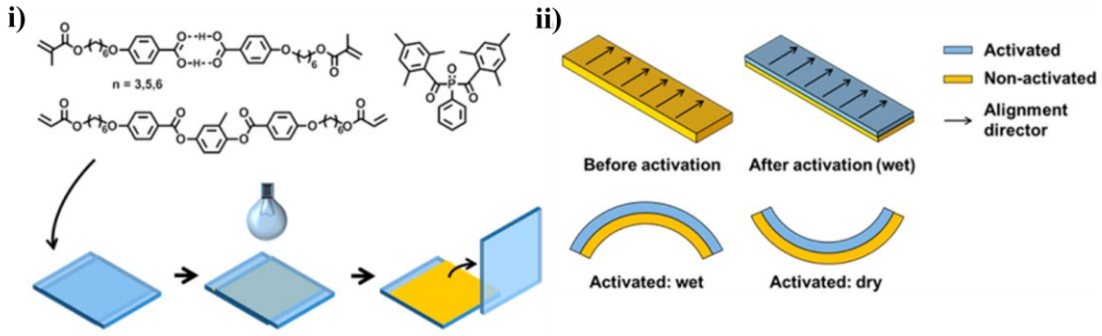

Figure 8. i) Chemical composition of the LCE with hydrogen-bonded mesogens and preparation procedure of bilayer LCE actuator. (ii) Schematic showing the bending behavior of the bilayer LCE ribbon upon water absorption (actuator initially dry) or desorption

(actuator initially swollen by water), the alignment director being perpendicular to the long axis of the ribbon. Reprinted with permission. Copyright 2014, American Chemical Society. (63)

The third smart function beyond actuation is that LCE actuator can dynamically change their color in response to external stimuli (heat, light, humidity, pressure), or to mesogen or LCE structural change (bond breaking, crosslinking). (69-72) While the color change, generally it is due to a change in the ordering of the mesogens and subsequent changes in light transmission, reflection, or absorption or emission. Early works reported a change of the reflection color in response to pH or humidity derives from specific composition of LCE. (19) Generally speaking, a LCE film displaying reflection color is a cholesteric LCE with supramolecular helixes aligned in the film thickness direction. As pointed out in section 1.2, this is a photonic crystal that reflects light with wavelength matching the pitch of the helix (equation 4). For example, in a work reported by Schenning et al, patterned photonic coating of cholesteric LCE comprising commonly used chiral dopant and benzoic acid derivatives, can change the color under exposure to water (Figure 9a). (73) After base solution treatment to break H-bonded benzoic acid dimers (mesogens), the LCE becomes hygroscopic and swells in water, which leads to an increase of the helix pitch and thus causes a red-shift in the wavelength of reflected light. More interesting, by varying the quantity of chiral dopant in the monomer mixture, coatings with different regions reflecting distinct colors can be achieved (Figure 9b). Apart from humidity-induced pitch change, mechanical force is another stimulus that can cause reflection color change of cholesteric LCE (Figure 9c). (74) In this case, with increasing the stretching ratio at room temperature, the color of the LCE film changes continuously from red to blue due to continuous decrease in the helical pitch as a result of the elongation-induced compression in the film thickness direction. This stretching process is totally reversible even after 100 times of stretching-relaxation cycles. Furthermore, the thermally activated dynamic B-O bond exchange allows the strain-induced mesogen alignment to be memorized, enabling self-healing and

reprocessing actuators with 2D or 3D shape. A color-changing actuator is shown in Figure 9c: upon cyclic heating and cooling at 25 °C and 100 °C, a green-reflecting strip at room temperature can lift up a load 300 times heavier than its own weight upon heating to 100 °C, with the green color disappeared concomitantly. In addition to cholesteric LCE for structured colors, Li et al. developed a LCE actuator by introducing a multi-stimuli-responsive tetraarylsuccinonitrile (TASN) chromophore in the polymer structure, enabling reversible color-change and shape deformation in response to heat and mechanical pressure (Figure 9d). (75) In the example, TASN units in the polymer network act as dynamic covalent mechano-chrompphores and in the form of colorless dimers, in which the central carbon-carbon bond can be dissociated by heat and mechanical compression, and the resulting radical monomeric from species are pink colored induced. In the same vein, Yang et al. reported a LCE actuator with colors from both aggregation-induced emission (AIE) and photochromic luminescence through incorporating tetraphenylethene (TPE), an AIEgen, and spiropyran, a photochromic switch, in the LCE structure, in addition to the loading of a near-infrared (NIR) dye (Figure 9e). (76) First, the presence of NIR dye ensures light-triggered reversible actuation deformation through photothermal effect. Secondly, the fluorescence colors are tuned by the UV and visible light irradiation that induce reversible photoisomerization of spiropyran to merocyanine and vice versa. By using these synergetic color-changing and shape-morphing, the LCE actuator can be processed into Miura folding origami. Under NIR light, the Miura-folded actuator expands in all directions, weakening the red fluorescence, while the fluorescent color and shape of the actuator can be simultaneously restored to their original state after removal of NIR irradiation. Moreover, the fluorescent color shifts to blue-green under visible light (530 nm) and subsequently changes to dull red during NIR exposure (Figure 9e). Recently, our group also designed a dynamic LCE actuator using the Diels-Alder (DA) reaction-based crosslinker that bears an AIEgen (TPE derivative) (Figure 9f). (77) We showed that the fluorescence emission intensity is directly related to the crosslinking degree and thus to the actuation performance. In other

words, the dynamic AIE crosslinker is a fluorescence probe that can report the LCE cross-linking and actuation state through real-time visualization of the emitted color.

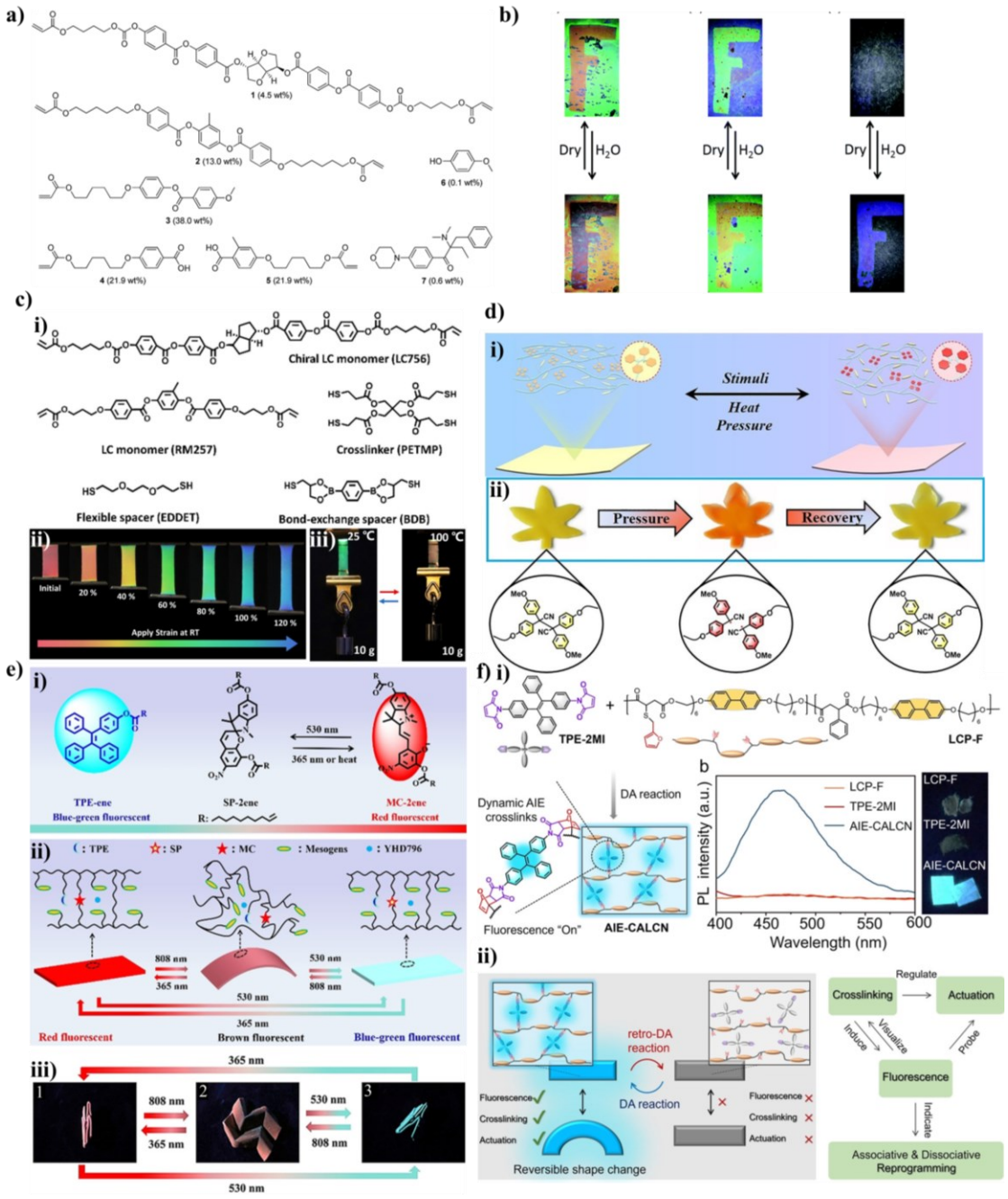

Figure 9. a) The chemical components used for the preparation of water-responsive cholesteric LCE. The mixture consists of chiral dopant, nematic mesogens and benzoic acid derivatives. b) Optical images showing the color change of three LCE patterns with the

letter “F” in ambient conditions (dry) and wet state (H_2O). Reprinted with permission. (73) Copyright 2015 The Royal Society of Chemistry. c): i) Molecular structures of the components used for fabricating color-changing LCE actuator. ii) Photos showing continuous color change of a red-reflecting actuator upon mechanical stretching. iii) Photos showing the load lifting by a colorful actuator, the load being 300 times heavier than the weight of the actuator. Reproduced with permission. (74) Copyright 2021, Wiley-VCH. d): i) Schematic illustration showing the heat and pressure-induced color change of an LCE actuator. ii) Photos of the maple leaf-shaped LCE sample recorded before and after mechanical squeezing. Reproduced with permission. (75) Copyright 2021, Wiley-VCH. e): i) Chemical structures of the used AIE-type fluorophore (TPE) and the functionalized spiropyran (SP), a photochromic dye with the reversible conversion between the open form merocyanine (MC, red fluorescence) and the close form SP (nonfluorescent). ii) Schematic showing the mechanism of simultaneously controlling the fluorescence changes and deformation. iii) Simultaneous multicolor fluorescence change and complex shape-morphing of 3D LCE actuator: “Miura fold” under light stimulations (UV, visible and NIR). Reproduced with permission. (76) Copyright 2021, Wiley-VCH. f): i) Chemical structures of the used bismaleimide bearing AIEgen (TPE-2MI) and furan-grafted liquid crystal polymer (LCP-F), as well as the preparation of the LCE actuator (AIE-CALCN) through the Diels-Alder (DA) reaction between maleimide and furan groups. Photoluminescence (PL) spectra of LCP-F, TPE-2MI, and AIE-CALCN (λ_{ex}=340 nm), and their photographs taken under a 365 nm UV lamp. ii) Schematics showing the DA chemistry-based reversible tuning of material crosslinking, fluorescence emission and actuation capability of the actuator made with dynamic AIE crosslinks (left panel), and a recapitulation of the LCE properties and functions (right panel). Reprinted with permission. (77) Copyright 2022, Wiley-VCH.

1.5 Porous Polymers

Porous materials consist of voids, channels, holes, or basically pores. Thanks to this characteristic property, they have always attracted a lot of attention. In nature, there are many porous materials, such as tissue and bone in the human body and animals, rocks, fruits and so on. In addition, porous materials are synthesized or produced in the laboratory for use in practical applications in many fields, such as concrete road, paper, chalk, and artificial sponges. (78) Porous polymers combined advantages of porous and polymeric materials, and have garnered much attention as they offer a wide spectrum of application, including separation membrane, battery separator, solid catalyst and sensor supports. (79-81) Therefore, these high-value applications drive the recent emphasis on the development of reliable methods for preparation of porous polymers, with designed pore architectures. According to the range of pore sizes, porous polymers can be categorized into three classes: microporous with pore size < 2 nm, mesoporous with pore size in the range of 2-50 nm, macroporous with pore size > 50 nm. (82) Among the characterizations of porous polymers, the specific surface area is an important parameter that is used to evaluate the pore size and structure, which is analyzed by Brunauer-Emmett-Teller (BET) theory.

To produce the porous polymer films with precisely controlled pore sizes, various methods have been developed, including direct templating (or hard templating), block copolymer (BCP) self-assembly (soft templating) and direct synthesis methodologies, each of which has its own advantages and limitations. The block copolymer self-assembly method is used to produce mesoporous or macroporous polymers, especially for materials with long-range order due to microphase separation of incompatible blocks to generating mesoscale structures. (83, 84) In this method, the self-assembly of BCPs serves either as a pore template (removable component) (85) or, most often, a source of the polymer framework (creating pore inside). The mechanism for formation of pore in BCPs is generally one of the following: 1) etching one of the constituent blocks, 2) removal of additional components, 3)

physical reconstruction of the morphology, 4) selective cross-linking of dynamic self-assembled BCP vesicles. Porous polymers prepared using BCP self-assembly have precise and controllable pore structure (Figure 10a, left). (86, 87) For example, following the self-assembly of an A-B deblock copolymer, removal of the B block creates ordered pores whose diameter is determined by the chain length of the B block. If a third polymer is added as the middle block to form an A-B-C triblock copolymer, after the same process of self-assembly and removal of one end block, the wall of pore is covered by the third polymer (Figure 10a, right). (88). Furthermore, microporous polymers can be obtained through solution polymerization with controlling the solvent removal. (89-95) And the reaction-induced phase separation procedures are also commonly used to prepare the mesoporous or macroporous polymers (Figure 10b, left). (96, 97) An example is shown in Figure 10b (right). Using PS-b-PEO diblock copolymer and tungsten chloride (WCl_6) as soft template and tungsten precursor, the formation of ordered mesoporous WO_3 materials proceeds through four steps: 1) with the evaporation of THF, spherical composite micelles with PS core surrounded by a shell of hybrid PEO-AcAc (acetylacetone)-stabilized tungsten species are formed; 2) upon further evaporation of THF, ordered 3D meso-structure is formed and fixed through annealing at 100 °C for 24 h; 3) the as-made inorganic-polymer hybrid is calcined in N_2 at 350 °C, leading to carbon-supported mesoporous WO_3 materials; 4) ordered mesoporous WO_3 materials are finally obtained after removal of the supporting carbon in the pore channel via calcination in air at 500 °C. (98)

The direct templating method, however, is probably the simplest and most versatile for fabricating porous polymers, including casting and molding techniques. (99-103) Various types of templates, such as porogenic solvents, (91, 96, 104) gas-forming templates, (105, 106) micelle templates, and sacrificial particles or fillers, and degradable segments in self-assembled BCPs (83, 84) can be employed. Basically, the procedure of direct templating contains three main and consecutive steps (Figure 10c, left): 1) infiltration or adsorption of the raw materials (monomers, *etc.*) required for the preparation of the polymeric framework

onto the surfaces or into interstitial voids of the templates; 2) in situ polymerization or solidification of the distributed raw materials; and 3) removal of the templates. For example, 3D macroporous polyethylene has been successfully prepared via coordination reaction after infiltration of gaseous ethylene into a catalyst-functionalized silica template (Figure 10c, right). (107) Figure 11 provides a summary figure showing a large number of examples of templates and their removal conditions that can be applied to prepare porous polymers through the direct templating method. (87) Among them, the most used templates include the nanoparticles or crystals of silica, $CaCO_3$, ZnO, NaCl, and PS since they are very easily removed by wet chemical etching with HF, HCl, water or organic solvents. The choice of the template also depends on the specific application requirements.

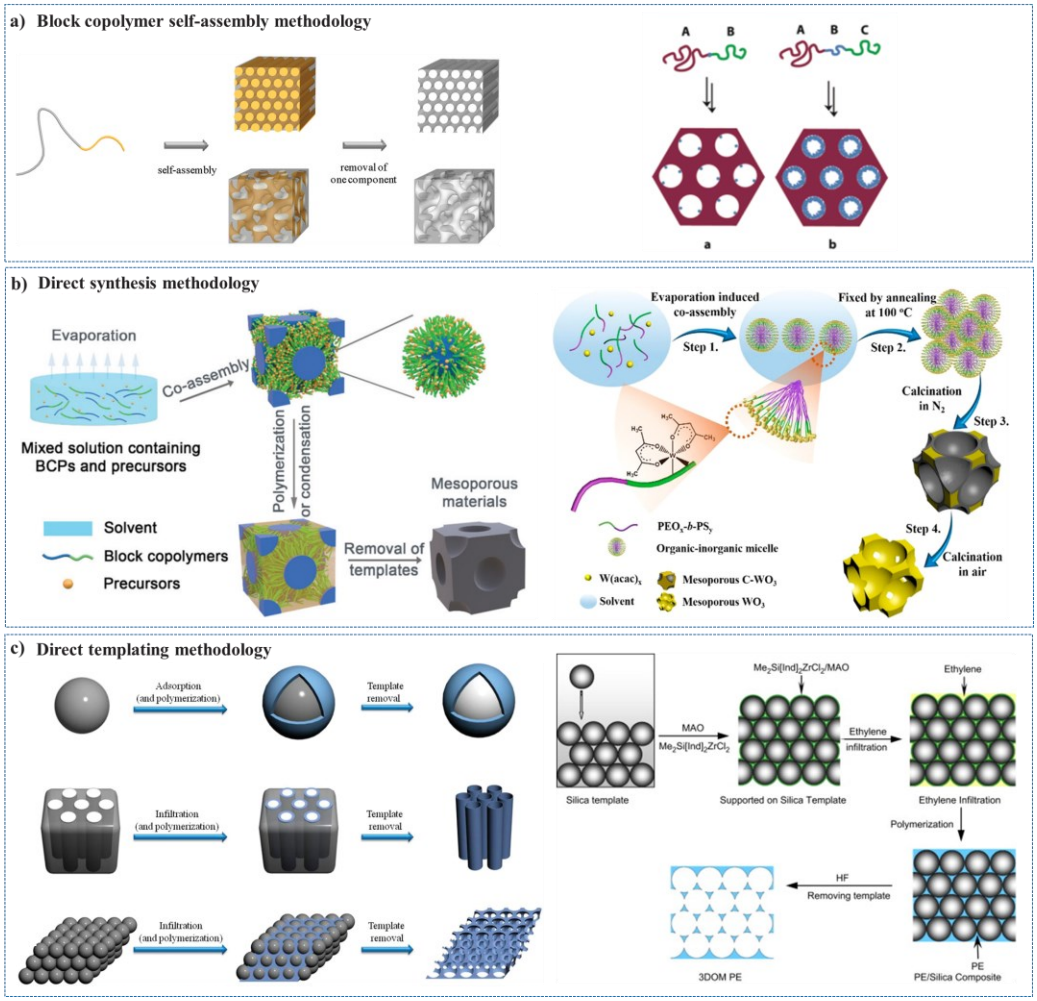

Figure 10. a) Left: Self-assembly of BCPs with sacrificial components for the generation of pores. Reprinted with permission from ref (87), Copyright 2012, American Chemical Society. Right: Schematic representation of a nanoporous material obtained from an AB diblock (a) and an ABC triblock (b) copolymer precursors, each with one degradable block (green). Reprinted with permission from ref (88). Copyright 2005, American Chemical Society. b) Left: Schematic illustration of a typical process for the direct synthesis of mesoporous materials using BCPs as the soft template. Reprinted with permission from ref (108), Copyright 2020, Royal Society of Chemistry. Right: Schematic illustration of the formation of ordered mesoporous WO_3 materials via the solvent evaporation induced co-assembly approach. Reprinted with permission. (98) Copyright 2017, American Chemical Society. c) Left: Schematic showing the fabrication of individual spherical porous polymers from solid spherical nanoparticles templates (top), tubular porous polymers from tubular porous templates (middle), ordered macroporous polymers from colloidal crystal templates (bottom). Reprinted with permission from ref (87), Copyright 2012, American Chemical Society. Right: Schematic diagram for fabricating 3D ordered macroporous polyethylene by gaseous infiltration method. Reprinted from ref (107), Copyright 2008, with permission form Elsevier.

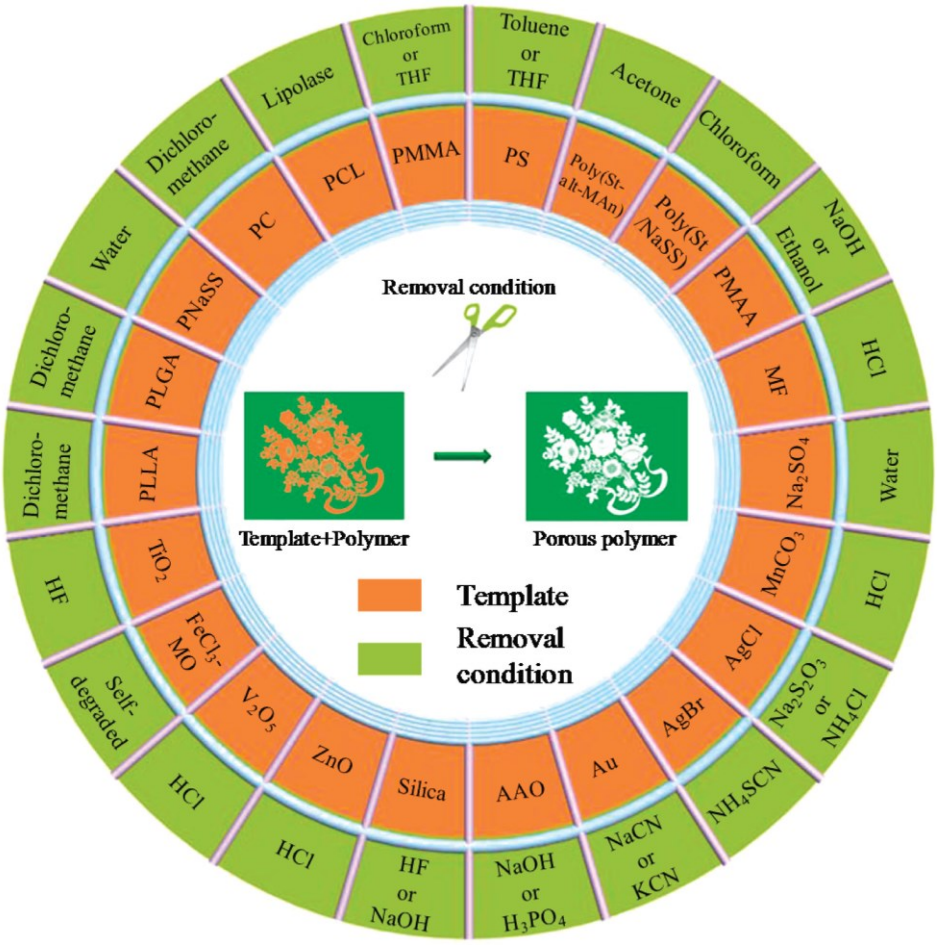

Figure 11. A summary of various templates and their removal conditions. The templates are shown in the inner ring and their corresponding removal conditions are indicated in the outer ring. Reprinted with permission. (87) Copyright 2012, American Chemical Society.

As already mentioned above, porous polymers are found to have many applications enabled by the pressure and organization of pores. A porous structure endows the materials with the unique feature of having an available three-dimensional space for incorporation of multiple functional compounds or particles or materials with different properties. As a matter of fact, porous polymers have been explored for actuator applications in artificial muscles, soft robotics, and energy generators. (8, 109, 110) Such actuating porous polymers can respond to environmental stimuli, such as change in humidity, temperature and pH. A representative example is shown in Figure 2a,b. A porous polyelectrolyte membrane

made with a polymer ionic liquid (PIL) and a pillararene complex (PILTf_2N/C-pillar[5]arene) can respond to the actuator acetone vapor and deform. On the one hand, the bending behavior is contributed by a gradient in the electrostatic complexation degree along the thickness of membrane, which is accompanied by heterogeneous swelling, leading to the membrane in contact with organic vapors. On the other hand, the presence of pore structure can speed up the diffusion kinetics of solvent gas to the site of action, improving their sensitivity. (111) In addition, based on a similar method, Yuan and co-workers reported a porous PCMVImTf_2N-PAA membrane actuator exhibiting exceptional sensitivity to low organic solvent concentrations (Figure 12c, d). This is accomplished by integrating porous architectures and electrostatic complexation gradients in the membrane that bears ionic liquid species for solvent sorption. The pore channels not only accelerate mass transport of solvents into the membrane but also weaken the overall bending rigidity. The pore structures circumvent the need for a high acetone concentration, thus leading to a higher sensitivity to solvent concentration (as low as 0.25 mol% acetone molecules in water). (112)

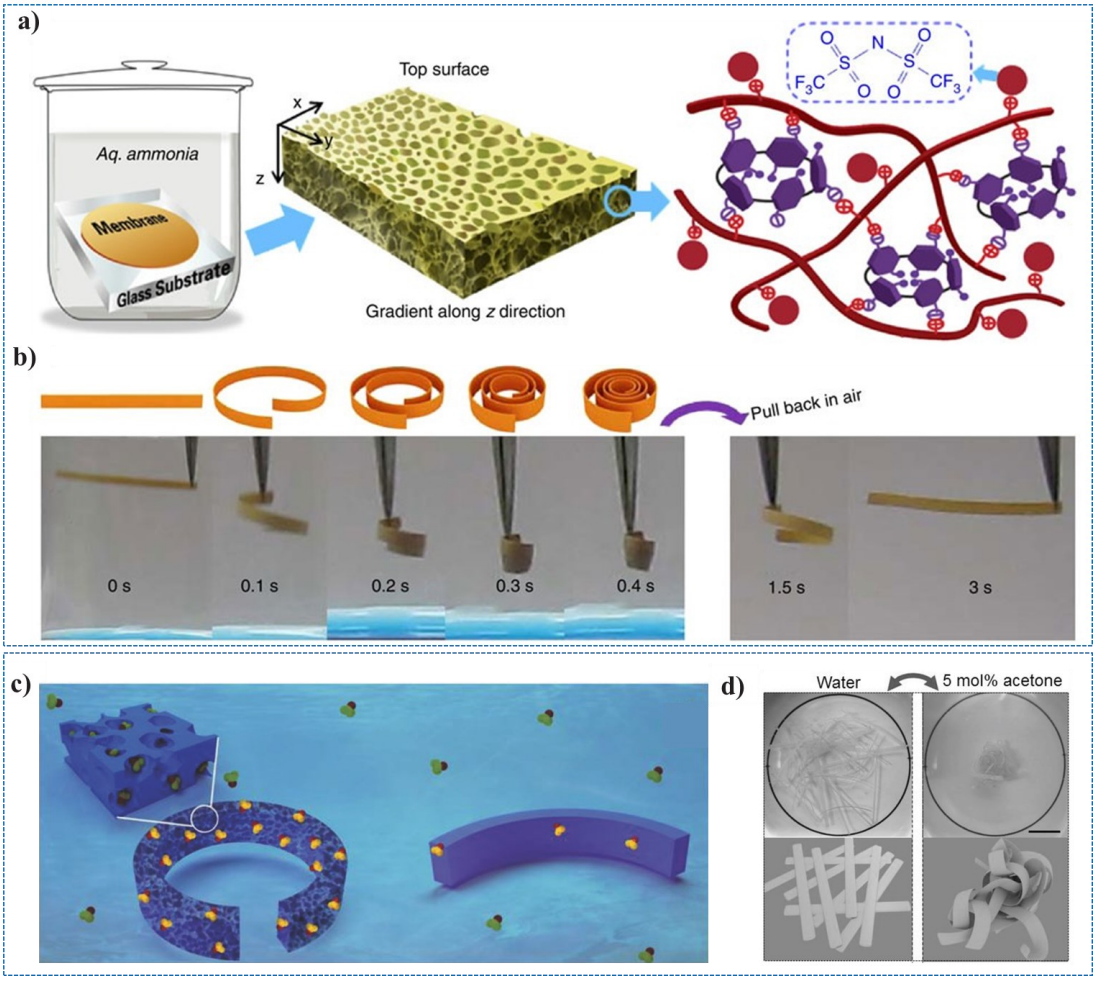

Figure 12. a) A scheme illustrating the preparation route (left), porous morphology (middle), and the chemical structure (right) of the PILTf$_2$N/C-pillar[5]arene membrane actuator. Right: The red line and purple ring represent PILTf$_2$N polymer chains and C-pillar[5]arene molecules, respectively; this cartoon schematizes the electrostatic complexation between the imidazolium cations on PILTf$_2$N and the carboxylate anions on C-pillar[5]arene molecules. b) Adaptive movement of a PILTf$_2$N/C-pillar[5]arene membrane (1 mm × 20 mm × 30 mm) placed in acetone vapor (24 kPa, 20 °C, left) and then back in air (right). Note: Acetone solvent is stained in blue. Reproduced with permission. (111) Copyright 2014, Nature Publishing Group. c) A schematic mechanism of the sensitive actuation of a porous membrane actuator (on the left) compared to dense one (right). d) Cooperative actuation of 30 PCMVImTf$_2$N-PAA membranes (1 mm × 25 mm × 30 μm) shuttled between water (left)

and a 5 mol% acetone–water mixture (right); pictures were taken at a top view; the schemes (bottom panel) illustrate the entangling–disentangling of membrane stripes. The scale bar is 1 cm. Reproduced with permission. (113) Copyright 2015, Wiley-VCH.

Few reports on porous liquid crystal polymers can be found in the literature. Most notable is a several of studies by Broer and collaborators, (114, 115) which are summarize in Figure 13. They prepared nanoporous (or microporous) LCPs using H-bonded benzoic acid dimers as side-group mesogens. As already mentioned in section 1.4 (Figure 7), an alkaline treatment can break the mesogenic dimers and leads to the formation of LCP salt. Based on this mechanism, after obtaining an ordered smectic phase of reactive dimers by means of rubbed surface, photopolymerization is carried out to fix the smectic order in the resulting LCP network. Afterwards, an alkaline treatment with nanopores (nanochannels) confined between smectic layers. This nanoporous membrane can absorb aqueous solutions, allowing reagents, chemicals, or ions to flow into the membrane. Using this property, several applications have been demonstrated, including in-situ formation of silver nanoparticles and their 2D patterning imposed by the confinement, efficient and selective absorbent for cationic dyes, and dynamic polarity switching. (115, 116)

As for porous LCPs or LCEs prepared using the direct template method, reported studies are even rarer. The notable work is about the use of a salt-leaching method to prepare porous, crosslinked lactone- and lactide-based star block copolymers with cholesterol liquid crystal pendants. (117) In this case, the material was designed to promote cell growth through an LC alignment effect. Interestingly, other techniques were utilized recently to make porous LCEs designed for specific properties. In one case, 3D printing was employed to fabricate LCE foam that can efficiently enhance the impact-absorbing capability due to the soft-elasticity of LCE. (118, 119) In another case, LCE-based aerogel was obtained using a facile thermally-induced thiolene click chemistry for polymerization and crosslinking, followed by supercritical CO_2 extraction. (120) This LCE aerogel not only shows

excellent compressibility but also reversible shape deformation. For both LCE foam and aerogel, the volume fraction of pores (porosity) is large.

Despite the existing reports (very few) on porous LCPs or LCEs as discussed above, the least we can say is that this topic remains largely unexplored until now, especially about porous LCE actuators. Can the presence of pores or the porous structure endow LCE actuator with new functions or properties? Can such pore-enabled new functions or properties be exploited for potential applications? The present thesis aims to address these questions.

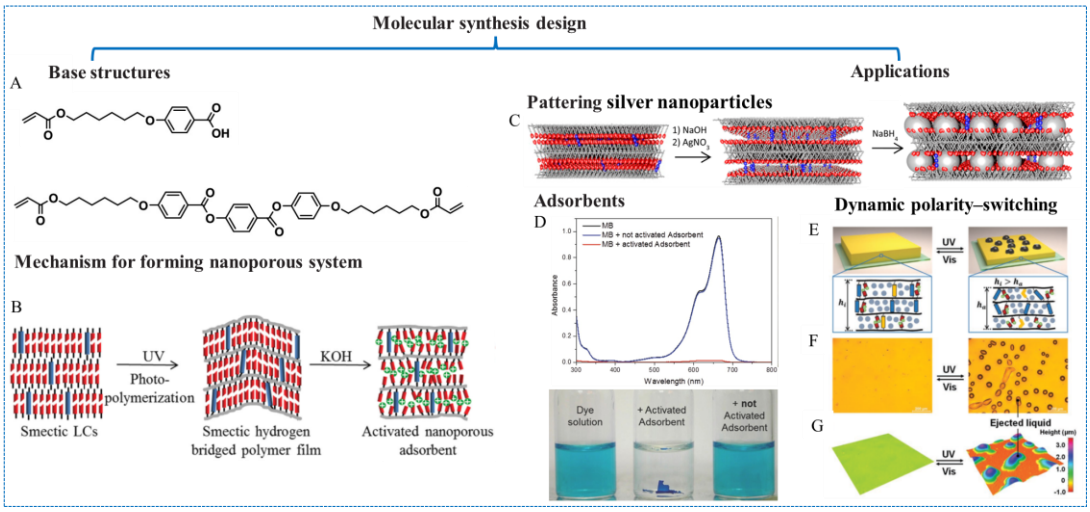

Figure 13. Preparation and applications of nanoporous LCP network using benzoic dimers as side-group mesogens. A) Chemical structures of the used monomer. B) Schematic representation of the formation mechanism of the nanoporous membrane based on smectic liquid crystals. Reproduced with permission from ref (115), Copyright 2014, Wiley-VCH. C) Schematic showing the patterning of silver nanoparticles through in-situ formation between smectic layers. Reprinted with permission from ref (116), Copyright 2013, American Chemical Society. D) Selective absorbent for cationic methylene blue (MB) dye. Top: UV-vis spectra of the dye solutions before and after being added to the activated or non-activated adsorbent. Bottom: vials with the initial dye solution (left side), the dye solution with the activated nanoporous adsorbent (middle), and with the non-activated adsorbent (right). Reproduced with permission from ref (115), Copyright 2014, Wiley-VCH. E-G) Dynamic

polarity-switching for filling of the glass-supported membrane with ethylene glycol and the subsequent secretion: E) secretion and uptake of ethylene glycol monitored by F) optical microscope and G) digital holographic microscope. Reprinted with permission from ref (121), Copyright 2023, Wiley-VCH.

1.6 Objective of the Thesis

The objective of this thesis is to study porous LCE actuator, discover possible new properties and explore the use of pores to endow the actuator with new functions. We hope to be able to demonstrate that making pores is a simple yet powerful approach in developing multifunctional actuators with application potential without synthesizing LCEs of new molecular structures or engineering complex actuator geometry.

Motivated by this objective, we have conducted several studies using the same LCE, which are the first of the kind in the field as reported in the following chapters. In Chapter 2, we used $CaCO_3$ nanoparticles as the template and prepared microporous LCE actuator. By discovering the hydrogel-like water absorption of the porous actuator made with an initially hydrophobic LCE, we showed the reversible deformation based on two different actuation mechanisms. More importantly, we used the swelling in aqueous solution to demonstrate the concept of "function reconfigurability" for a same actuator by loading-unloading-reloading different active fillers through the pore channels. In Chapter 3, we focused our effort on porous LCE actuator filled with an ionic liquid. We demonstrated its use either as deformable sensor through change in electrical resistance in response to various-mode mechanical deformation or as stimuli-triggered actuator. These two functions can be activated either separately (as from two types of materials) or collectively (the actuator component in a device can switch its role from sensor to actuator when needed). In Chapter 4, we proposed the concept of “active porogen” by using MOF nanoparticles as the template in making porous LCE actuator. Before MOF removal, the actuator is microporous due to the molecular cavities in MOF, while after MOF removal, the actuator becomes macroporous.

We made a number of interesting and unexpected findings with this type of porous LCE actuator, including peculiar deformation in water for actuator comprising a layer with MOF and a layer with MOF removed, and the magnetic property of the macroporous LCE actuator after acid etching, which is attributed to the in-situ formation of Fe_3O_4 nanoparticles. The thesis is concluded with a general discussion and conclusion.

BIBLIOGRAPHY

1. Aguilar, M. R., Román, J. S. Smart Polymers and their Applications. Burlington: Elsevier Science; **2014**.

2. Ionov, L. Polymeric actuators. *Langmuir*, **2015**, *31* (18): 5015-24.

3. Zhang, Q. M., Serpe, M. J. Stimuli-Responsive Polymers for Actuation. *Chemphyschem*, **2017**, *18* (11): 1451-65.

4. Pilz da Cunha, M., Debije, M. G., Schenning, A. Bioinspired light-driven soft robots based on liquid crystal polymers. *Chem. Soc. Rev.*, **2020**, *49* (18): 6568-78.

5. Xiao, Y. Y., Jiang, Z. C, Zhao, Y. Liquid Crystal Polymer-Based Soft Robots. *Adv. Intell. Syst.*, **2020**, *2* (12): 2000148.

6. Zhu, C., Lu, Y., Jiang, L., Yu, Y. Liquid Crystal Soft Actuators and Robots toward Mixed Reality. *Adv. Funct. Mater.*, **2021**, *31* (39): 2009835.

7. Wang, Y., He, Q., Wang, Z., Zhang, S., Li, C., Wang, Z., Cai, S. Liquid Crystal Elastomer Based Dexterous Artificial Motor Unit. *Adv. Mater.*, **2023**, *35* (17): e2211283.

8. Wu, J., Xu, F., Li, S., Ma, P., Zhang, X., Liu, Q., Wu, D. Porous Polymers as Multifunctional Material Platforms toward Task-Specific Applications. *Adv. Mater.*, **2019**, *31* (4): e1802922.

9. Silverstein, M. S., Cameron, N. R., Hillmyer, M. A. Porous polymers. John Wiley & Sons; **2011**.

10. Janocha, H. Introduction. In: Janocha H, editor. Actuators: Basics and Applications. Berlin, Heidelberg: Springer Berlin Heidelberg; **2004**. p. 1-17.

11. O'Halloran, A., O'Malley, F., McHugh, P. A review on dielectric elastomer actuators, technology, applications, and challenges. *J. Appl. Phys.* **2008**. *104* (7): 071101.

12. Osmani, B., Aeby, E. A., Müller, B. Stress measurements of planar dielectric elastomer actuators. *Rev. Sci. Instrum.* **2016**, *87* (5): 053901.

13. Kornbluh, R., Heydt, R., Pelrine, R. Dielectric elastomer actuators: fundamentals. biomedical applications of electroactive polymer actuators. **2009**, p: 385-93.

14. Romasanta, L. J., Lopez-Manchado, M. A., Verdejo, R. Increasing the performance of dielectric elastomer actuators: A review from the materials perspective. *Prog. Poly. Sci.* **2015**, 51: 188-211.

15. White, B. T., Long, T. Advances in polymeric materials for electromechanical devices. *Macromol. Rapid Comm.* **2019**, *40* (1):1800521.

16. Gu, G. Y., Zhu, J., Zhu, L. M., Zhu, X. A survey on dielectric elastomer actuators for soft robots. *Bioinspir. Biomim.* **2017**, *12* (1): 011003.

17. Ula, S. W., Traugutt, N. A., Volpe, R. H., Patel, R. R., Yu, K., Yakacki, C. M. Liquid crystal elastomers: an introduction and review of emerging technologies. *Liq. Cryst. Rev.*, **2018**, *6* (1): 78-107.

18. Bisoyi, H. K., Kumar, S. Liquid-crystal nanoscience: an emerging avenue of soft self-assembly. *Chem. Soc. Rev.*, **2011**, *40* (1): 306-19.

19. Bisoyi, H. K., Li, Q. Liquid Crystals: Versatile Self-Organized Smart Soft Materials. *Chem. Rev.*, **2022**, *122* (5): 4887-926.

20. Warner, M., Terentjev, E. M. Liquid Crystal Elastomers. Oxford OUP Oxford; **2003**.

21. Collings, P. J, Goodby, J. W. G. Introduction to Liquid Crystals: Chemistry and Physics. Second edition. ed. Boca Raton: CRC Press, Taylor & Francis Group; **2020**.

22. Tran, A., Boott, C. E., MacLachlan, M. Understanding the Self-Assembly of Cellulose Nanocrystals—Toward Chiral Photonic Materials. *Adv. Mater.*, **2020**, *32* (41):1905876.

23. Ohm, C., Brehmer, M., Zentel, R. Liquid Crystalline Elastomers as Actuators and Sensors. *Adv. Mater.*, **2010**, *22* (31): 3366-87.

24. Cotton, J., Hardouin, F. H. Chain Conformation of Liquid Crystalline Polymers Studied by Small-angle Neutron Scattering. *Prog Polym Sci.*, **1997**, *22* (4): 795-828.

25. Chen, X. F., Shen, Z., Wan, X. H., Fan, X. H., Chen, E. Q., Ma, Y., Zhou, Q. F. Mesogen-jacketed Liquid Crystalline Polymers. *Chem. Soc. Rev.*, **2010**, *39* (8): 3072-101.

26. Brömmel, F. K. D, Finkelmann, H. liquid Crystal Elastomers: Materials and Applications. New York (NY): Springer; **2012**., P1-48.

27. Herbert, K. M., Fowler, H. E., McCracken, J. M., Schlafmann, K. R., Koch, J. A., White, T. J. Synthesis and alignment of liquid crystalline elastomers. *Nat. Rev. Mater.*, **2022**. *7* (1): 23-38.

28. Usman, A., Uwada, T., Masuhara, H. Optical Reorientation and Trapping of Nematic Liquid Crystals Leading to the Formation of Micrometer-Sized Domain. *J. Phys. Chem. C.*, **2011**, *115* (24): 11906-13.

29. Kundler, I., Finkelmann, H. Director Reorientation via Stripe-domains in Nematic Elastomers: Influence of Cross-link Density, Anisotropy of the Network and Smectic Clusters. *Macromol. Chem. Phys.*, **1998**, *199* (4): 677-86.

30. Küpfer, J., Finkelmann, H. Nematic Liquid Single Crystal Elastomers. *Makromol. Chem.*, **1991**, *12* (12): 717-26.

31. Kundler, I., Finkelmann, H. Strain-induced Director Reorientation in Nematic Liquid Single Crystal Elastomers. *Macromol. Rapid Commun.*, **1995**, *16* (9): 679-86.

32. Ware, T. H., McConney, M. E., Wie, J. J., Tondiglia, V. P., White, T. Voxelated Liquid Crystal Elastomers. *Science*, **2015**, *347* (6225): 982-4.

33. Yakacki, C., Saed, M., Nair, D., Gong, T., Reed, S., Bowman, C. Tailorable and Programmable Liquid-crystalline Elastomers Using a Two-stage Thiol–acrylate Reaction. *RSC Adv.*, **2015**, *5* (25): 18997-9001.

34. Broer, D. J., Finkelmann, H., Kondo, K. In-situ Photopolymerization of an Oriented Liquid-crystalline Acrylate. *Macromol. Chem. Phys.*, **1988**, *189* (1): 185-94.

35. Davidson, Z. S., Shahsavan, H., Aghakhani, A., Guo, Y., Hines, L., Xia, Y., Yang, S., Sitti, M. Monolithic shape-programmable dielectric liquid crystal elastomer actuators. *Sci. Adv.*, **2019**, *5* (11): eaay0855.

36. Yang, R., Zhao, Y. Non-Uniform Optical Inscription of Actuation Domains in a Liquid Crystal Polymer of Uniaxial Orientation: An Approach to Complex and Programmable Shape Changes. *Angew. Chem. Int. Ed.*, **2017**, *56* (45): 14202-6.

37. Bisoyi, H. K., Li, Q. Light-driven Liquid Crystalline Materials: from Photo-induced Phase Transitions and Property Modulations to Applications. *Chem. Rev.*, **2016**, *116* (24): 15089-166.

38. Pang, X., Lv, J. A., Zhu, C., Qin, L., Yu, Y. Photodeformable Azobenzene-Containing Liquid Crystal Polymers and Soft Actuators. *Adv. Mater.*, **2019**, *31* (52): e1904224.

39. Chen M, Yao B, Kappl M, Liu S, Yuan J, Berger R, et al. Entangled Azobenzene-Containing Polymers with Photoinduced Reversible Solid-to-Liquid Transitions for Healable and Reprocessable Photoactuators. *Adv. Funct. Mater.*, **2019**, *30* (4): 1906752.

40. Pilz da Cunha, M., van Thoor, E. A. J., Debije, M. G., Broer, D. J. Schenning, A. P. Unravelling the Photothermal and Photomechanical Contributions to Actuation of Azobenzene-doped Liquid Crystal Polymers in Air and Water. *J. Mater. Chem. C.*, **2019**, *7* (43): 13502-9.

41. Yang, H., Liu, J. J., Wang, Z. F., Guo, L. X., Keller, P., Lin, B. P., Zhang, Q. X. Near-infrared-responsive Gold Nanorod/Liquid Crystalline Elastomer Composites Prepared by Sequential Thiol-click Chemistry. *Chem. Commun.*, **2015**, *51* (60): 12126-9.

42. Hauser, A. W., Liu, D., Bryson, K. C., Hayward, R. C., Broer, D. J. Reconfiguring Nanocomposite Liquid Crystal Polymer Films with Visible Light. *Macromolecules*, **2016**, *49* (5): 1575-81.

43. Wang, M., Sayed, S. M., Guo, L. X., Lin, B. P., Zhang, X. Q., Sun, Y., Hong, Y. Multi-Stimuli Responsive Carbon Nanotube Incorporated Polysiloxane Azobenzene Liquid Crystalline Elastomer Composites. *Macromolecules*, **2016**, *49* (2): 663-71.

44. Jiang, Z. C., Xiao, Y. Y., Cheng, R. D., Hou, J. B., Zhao, Y. Dynamic Liquid Crystalline Networks for Twisted Fiber and Spring Actuators Capable of Fast Light-Driven Movement with Enhanced Environment Adaptability. *Chem. Mater.*, **2021**, *33* (16): 6541-52.

45. Guo, L. X., Liu, M. H., Sayed, S. M., Lin, B. P., Keller, P., Zhang, X. Q., Yang, H. A Calamitic Mesogenic Near-infrared Absorbing Croconaine Dye/Liquid Crystalline Elastomer Composite. *Chem. Sci.*, **2016**, *7* (7): 4400-6.

46. Zeng, H., Lahikainen, M., Liu, L., Ahmed, Z., Wani, O. M., Wang, M., Priimagi, A. Light-fuelled Freestyle Self-oscillators. *Nat. Commun.*, **2019**, *10* (1): 1-9.

47. Lu, X., Zhang, H., Fei, G., Yu, B., Tong, X., Xia, H., Zhao, Y. Liquid-Crystalline Dynamic Networks Doped with Gold Nanorods Showing Enhanced Photocontrol of Actuation. *Adv. Mater.*, **2018**, *30* (14): 1706597.

48. Wani, O. M., Verpaalen, R., Zeng, H., Priimagi, A., Schenning, A. An Artificial Nocturnal Flower via Humidity-Gated Photoactuation in Liquid Crystal Networks. *Adv. Mater.*, **2019**, *31* (2): e1805985.

49. Lan, R., Sun, J., Shen, C., Huang, R., Zhang, L., Yang, H. Reversibly and Irreversibly Humidity-Responsive Motion of Liquid Crystalline Network Gated by SO_2 Gas. *Adv. Funct. Mater.*, **2019**, *29* (23): 1900013.

50. Liu, Y., Xu, B., Sun, S., Wei, J., Wu, L., Yu, Y. Humidity- and Photo-Induced Mechanical Actuation of Cross-Linked Liquid Crystal Polymers. *Adv. Mater.*, **2017**, *29* (9): 1604792.

51. Xiao, Y. Y., Jiang, Z. C., Hou, J. B., Chen, X. S., Zhao, Y. Electrically Driven Liquid Crystal Network Actuators. *Soft Matter.*, **2022**, *18* (26): 4850-67.

52. Xiao, Y. Y., Jiang, Z. C., Tong, X., Zhao, Y. Biomimetic Locomotion of Electrically Powered "Janus" Soft Robots Using a Liquid Crystal Polymer. *Adv. Mater.*, **2019**, *31* (36): e1903452.

53. He, Q. Q., Wang, Z. J., Wang, Y., Minori, A., Tolley, M. T., Cai, S. Q. Electrically Controlled Liquid Crystal Elastomer–based Soft Tubular Actuator with Multimodal Actuation. *Sci. Adv.*, **2019**, *5* (10): eaax5746

54. Kotikian, A., Morales, J. M., Lu, A., Mueller, J., Davidson, Z. S., Boley, J. W.,Lewis, J. A. Innervated, Self-Sensing Liquid Crystal Elastomer Actuators with Closed Loop Control. *Adv. Mater.*, **2021**, *33* (27): e2101814.

55. Ford, M. J., Ambulo, C. P., Kent, T. A., Markvicka, E. J., Pan, C., Malen, J., Majidi, C. A Multifunctional Shape-morphing Elastomer with Liquid Metal Inclusions. *PNAS*, **2019**, *116* (43): 21438-44.

56. Ambulo, C. P., Ford, M. J., Searles, K., Majidi, C., Ware, T. H. 4D-Printable Liquid Metal-Liquid Crystal Elastomer Composites. *ACS Appl. Mater. Interfaces*, **2021**, *13* (11): 12805-13.

57. Xu, L., Wagner, R. J., Liu, S., He, Q., Li, T., Pan, W., Feng, H., Meng, Q., Zou, X., Fu, Y. Locomotion of an untethered, worm-inspired soft robot driven by a shape-memory alloy skeleton. *Sci. Rep.*, **2022**, *12* (1): 12392.

58. Chen, S., Cao, Y., Sarparast, M., Yuan, H., Dong, L., Tan, X., Cao, C. Soft Crawling Robots: Design, Actuation, and Locomotion. *Adv. Mater. Technol.*, **2020**, *5* (2): 1900837.

59. Wang, W., Lee, J. Y., Rodrigue, H., Song, S. H., Chu, W. S., Ahn, S. H. Locomotion of inchworm-inspired robot made of smart soft composite (SSC). *Bioinspir. Biomim.*, **2014**, *9* (4): 046006.

60. Umedachi, T., Vikas, V., Trimmer, B. A. Softworms: the design and control of non-pneumatic, 3D-printed, deformable robots. *Bioinspir. Biomim.*, **2016**, *11* (2): 025001.

61. Broitman, E. The nature of the frictional force at the macro-, micro-, and nano-scales. *Friction*, **2014**, 2: 40-6.

62. Yamada, M., Kondo, M., Miyasato, R., Naka, Y., Mamiya, J. I., Kinoshita, M., Ikeda, T. Photomobile polymer materials—various three-dimensional movements. *J. Mater. Chem.*, **2009**, *19* (1):60-2.

63. de Haan, L. T., Verjans, J. M., Broer, D. J., Bastiaansen, C. W., Schenning, A. P. Humidity-responsive liquid crystalline polymer actuators with an asymmetry in the molecular trigger that bend, fold, and curl. *J. Am. Chem. Soc.*, **2014**, *136* (30): 10585-8.

64. Zheng, X., Guan, S., Zhang, C., Qu, T., Wen, W., Zhao, Y., Aihua, Chen. A Cut-and-Weld Process to 3D Architectures from Multiresponsive Crosslinked Liquid Crystalline Polymers. *Small.*, **2019**, *15* (16): e1900110.

65. Lan, R., Gao, Y., Shen, C., Huang, R., Bao, J., Zhang, Z.,Wang, Q., Zhang, L., Yang, H. Humidity-Responsive Liquid Crystalline Network Actuator Showing Synergistic Fluorescence Color Change Enabled by Aggregation Induced Emission Luminogen. *Adv. Functi. Mater.*, **2021**, *31* (17): 2010578.

66. Dai, M., Picot, O. T., Verjans, J. M., de Haan, L. T., Schenning, A. P., Peijs, T., Bastiaansen, C. W. Humidity-Responsive Bilayer Actuators Based on a Liquid-Crystalline Polymer Network. *ACS Appl. Mater. Inter.*, **2013**, *5* (11):4945-50.

67. Lan, R., Shen, W., Yao, W., Chen, J., Chen, X., Yang, H. Bioinspired humidity-responsive liquid crystalline materials: from adaptive soft actuators to visualized sensors and detectors. *Mater. Horiz*., **2023**, *122* (5): 4946-75.

68. Lugger, S. J., Houben, S. J., Foelen, Y., Debije, M. G., Schenning, A. P., Mulder, D. J. Hydrogen-Bonded Supramolecular Liquid Crystal Polymers: Smart Materials with Stimuli-Responsive, Self-Healing, and Recyclable Properties. *Chem. Rev.*, **2021**, *122* (5): 4946-75.

69. Shibaev, P. V., Sanford, R. L., Chiappetta, D., Rivera, P. Novel Color Changing pH Sensors Based on Cholesteric Polymers. *Mol. Cryst. Liq. Cryst.*, **2007**, *479* (1):161-7.

70. Shibaev, P. V., Chiappetta, D., Sanford, R. L., Palffy-Muhoray, P., Moreira, M., Cao, W.,Green, M. M. Color Changing Cholesteric Polymer Films Sensitive to Amino Acids. *Macromolecules*. **2006**, *39* (12): 3986-92.

71. Chen, F. J., Guo, J. B., Jin, O. Y., Wei, J. A temperature and pH double sensitive cholesteric polymer film from a photopolymerizable chiral hydrogen-bonded assembly. *Chin. J. Polym. Sci.* **2013**, *31* (4): 630-40.

72. Herzer, N., Guneysu, H., Davies, D. J., Yildirim, D., Vaccaro, A. R., Broer, D. J. ,Bastiaansen, C. W., Schenning, A. P. Printable Optical Sensors Based on H-Bonded Supramolecular Cholesteric Liquid Crystal Networks. *J. Am. Chem. Soc.*, **2012**, *134* (18): 7608-11.

73. Stumpel, J. E., Broer, D. J., Schenning, A. P. Water-responsive dual-coloured photonic polymer coatings based on cholesteric liquid crystals. *RSC Adv*., **2015**, *5* (115): 94650-3.

74. Ma, J., Yang, Y., Valenzuela, C., Zhang, X., Wang, L., Feng, W. Mechanochromic, Shape-Programmable and Self-Healable Cholesteric Liquid Crystal Elastomers Enabled by Dynamic Covalent Boronic Ester Bonds. *Angew. Chem. Int. Ed.*, **2021**, *61* (9): e202116219.

75. Liu, Z., Bisoyi, H. K., Huang, Y., Wang, M., Yang, H., Li, Q. Thermo- and Mechanochromic Camouflage and Self-Healing in Biomimetic Soft Actuators Based on Liquid Crystal Elastomers. *Angew. Chem. Int. Ed.*, **2022**, *61* (8): e202115755.

76. Huang, Y., Bisoyi, H., Huang, S., Wang, M., Chen, X. M., Liu, Z. Yang, H., Li, Quan. Bioinspired Synergistic Photochromic Luminescence and Programmable Liquid Crystal Actuators. *Angew. Chem. Int. Ed.*, **2021**, *60* (20): 11247-51.

77. Jiang, Z. C., Xiao, Y. Y., Hou, J. B., Chen, X. S., Yang, N., Zeng, H., Yue, Zhao. Dynamic AIE crosslinks in liquid crystal networks: visualizing for actuation-guiding, re-bonding for actuation-altering. *Angew. Chem. Int. Ed.*, **2022**, *61* (44): e202211959.

78. Voort, P., Leus, K., De Canck, E. Introduction to Porous Materials. Hoboken, NJ: Wiley; **2019**.

79. Su, B. L., Sanchez, C., Yang, X. Y. Hierarchically structured porous materials : from nanoscience to catalysis, separation, optics, energy, and life science. *Adv. Funct. Mater.*, **2012**, *22* (22): 4634-67.

80. Tan, L., Tan, B. Hypercrosslinked Porous Polymer Materials: Design, Synthesis, and Applications. *Chem. Soc. Rev.*, **2017**, *46* (11): 3322-56.

81. Li, J., Zhang, Y. Porous Polymer Films with Size-Tunable Surface Pores. *Chem. Mater.*, **2007**, *19* (10): 2581-4.

82. Sing, K. S. W., Everett, D., Haul, R., Moscou, L., Pierotti, R., Rouquerol, J., Siemieniewska, T. Reporting Physisorption Data for Gas/solid Systems with Special Reference to the Determination of Surface area and Porosity. *Pure Appl. Chem.*, **1985**, *57* (4): 603-19.

83. Hillmyer, M. A. Nanoporous Materials from Block Copolymer Precursors. *Block Compolymers II*, **2005**, *190*: 137-81.

84. Olson, D. A., Chen, L., Hillmyer, M. Templating Nanoporous Polymers with Ordered Block Copolymers. *Chem. Mater.*, **2008**, *20* (3): 869-90.

85. Wan, Y., Shi, Y., Zhao, D. Ordered Mesoporous Polymers and Carbon Molecular Sieves. *Chem. Mater.*, **2008**, *20*: 932-45.

86. Wang, Y., Li, F. An Emerging Pore-Making Strategy: Confined Swelling-Induced Pore Generation in Block Copolymer Materials. *Adv. Mater.*, **2011**, *23* (19): 2134-48.

87. Wu, D., Xu, F., Sun, B., Fu, R., He, H., Matyjaszewski, K. Design and Preparation of Porous Polymers. *Chem. Rev.*, **2012**, *112* (7): 3959-4015.

88. Rzayev, J., Hillmyer, M. A. Nanoporous Polystyrene Containing Hydrophilic Pores from an ABC Triblock Copolymer Precursor. *Macromolecules*, **2005**, *38* (1): 3-5.

89. Jiang, J. X., Cooper, A. I. Microporous Organic Polymers: Design, Synthesis, and Function. *Funct. Metal-organic Frameworks: Gas Storage, Separation, Catalysis*, **2010**, *293*: 1-33.

90. Mastalerz, M. The Next Generation of Shape-Persistant Zeolite Analogues: Covalent Organic Frameworks. *Angew. Chem. Int. Ed.*, **2008**, *47* (3): 445-7.

91. Tsyurupa, M., Davankov, V. A. Porous Structure of Hypercrosslinked Polystyrene: State-of-the-art mini-review. *React. Funct. Polym.*, **2006**, *66* (7): 768-79.

92. Cooper, A. I. Conjugated Microporous Polymers. *Adv. Mater.*, **2009**, *21* (12): 1291-5.

93. Weder, C. Hole Control in Microporous Polymers. *Angew. Chem. Int. Ed.*, **2008**, *47* (3): 448-50.

94. McKeown, N. B., Budd, P. M. Exploitation of Intrinsic Microporosity in Polymer-based Materials. *Macromolecules*, **2010**, *43* (12): 5163-76.

95. Holst, J. R., Cooper, A. I. Ultrahigh Surface Area in Porous Solids. Wiley Online Library; **2010**.

96. Al-Muhtaseb, S. A., Ritter, J. Preparation and Properties of Resorcinol–formaldehyde Organic and Carbon Gels. *Adv. Mater.*, **2003**, *15* (2): 101-14.

97. Kanamori, K., Nakanishi, K., Hanada, T. Rigid Macroporous Poly (divinylbenzene) Monoliths with a Well-defined Bicontinuous Morphology Prepared by Living Radical Polymerization. *Adv. Mater.*, **2006**, *18* (18): 2407-11.

98. Zhu, Y., Zhao, Y., Ma, J., Cheng, X., Xie, J., Xu, P., Zhao, D. Mesoporous Tungsten Oxides with Crystalline Framework for Highly Sensitive and Selective Detection of Foodborne Pathogens. *J. Am. Chem. Soc.*, **2017**, *139* (30): 10365-73.

99. Thomas, A., Goettmann, F., Antonietti, M. Hard Templates for Soft Materials: Creating Nanostructured Organic Materials. *Chem. Mater.*, **2008**, *20* (3): 738-55.

100. Lu, A. H., Schüth, F. Nanocasting: a Versatile Strategy for Creating Nanostructured Porous Materials. *Adv. Mater.*, **2006**, *18* (14): 1793-805.

101. Yang, H., Zhao, D. Synthesis of Replica Mesostructures by the Nanocasting Strategy. *J. Mater. Chem.*, **2005**, *15* (12): 1217-31.

102. Stein, A., Li, F., Denny, N. Morphological Control in Colloidal Crystal Templating of Inverse Opals, Hierarchical Structures, and Shaped Particles. *Chem. Mater.*, **2008**, *20* (3): 649-66.

103. Li, Q., Retsch, M., Wang, J., Knoll, W., Jonas, U. Porous Networks through Colloidal Templates. *Templates in Chemistry III*, **2009**, *287*: 135-80.

104. Bai, F., Huang, B., Yang, X., Huang, W. Synthesis of Monodisperse Porous Poly (divinylbenzene) Microspheres by Distillation–precipitation Polymerization. *Polymer*, **2007**, *48* (13): 3641-9.

105. Suslick, B. A., Hemmer, J., Groce, B. R., Stawiasz, K. J., Geubelle, P. H., Malucelli, G., Sottos, N. R. Frontal Polymerizations: from Chemical Perspectives to Macroscopic Properties and Applications. *Chem. Rev.*, **2023**, *123* (6): 3237-98.

106. Merlet, S., Marestin, C., Schiets, F., Romeyer, O., Mercier, R. Preparation and Characterization of Nanocellular Poly (phenylquinoxaline) Foams. A New Approach to Nanoporous High-performance Polymers. *Macromolecules*, **2007**, *40* (6): 2070-8.

107. Zhang, X., Yan, W., Yang, H., Liu, B., Li, H. Gaseous Infiltration Method for Preparation of Three-dimensionally Ordered Macroporous Polyethylene. *Polymer.*, **2008**, *49* (25): 5446-51.

108. Li, C., Li, Q., Kaneti, Y. V., Hou, D., Yamauchi, Y., Mai, Y. Self-assembly of Block Copolymers towards Mesoporous Materials for Energy Storage and Conversion Systems. *Chem. Soc. Rev.*, **2020**, *49* (14): 4681-736.

109. Zhang, W., Zhao, Q., Yuan, J. Porous Polyelectrolytes: The Interplay of Charge and Pores for New Functionalities. *Angew. Chem. Int. Ed.*, **2018**, *57* (23): 6754-73.

110. Hearon, K., Singhal, P., Horn, J., Small, W., Olsovsky, C., Maitland, K. C.,Maitland, D. J. Porous Shape Memory Polymers. *Polymer Rev.*, **2013**, *53* (1): 41-75.

111. Zhao, Q., Dunlop, J. W., Qiu, X., Huang, F., Zhang, Z., Heyda, J., Yuan, J. An Instant Multi-responsive Porous Polymer Actuator Driven by Solvent Molecule Sorption. *Nat. Commun.*, **2014**, *5* (1): 4293.

112. Zhao, Q., Heyda, J., Dzubiella, J., Täuber, K., Dunlop, J. W. C., Yuan, J. Sensing Solvents with Ultrasensitive Porous Poly(ionic liquid) Actuators. *Adv. Mater.*, **2015**, *27* (18): 2913-7.

113. Zhao, Q., Heyda, J., Dzubiella, J., Täuber, K., Dunlop, J. W. C., Yuan, J. Sensing Solvents with Ultrasensitive Porous Poly(ionic liquid) Actuators. *Adv. Mater.*, **2015**, *27* (18): 2913-7.

114. Gonzalez, C. L., Bastiaansen, C. W. M., Lub, J., Loos, J., Lu, K., Wondergem, H. J., Broer, D. J. Nanoporous Membranes of Hydrogen-bridged Smectic Networks with Nanometer Transverse Pore Dimensions. *Adv. Mater.*, **2008**, *20* (7): 1246-52.

115. van Kuringen, H. P. C., Eikelboom, G. M., Shishmanova, I. K., Broer, D. J., Schenning, A. P. Responsive Nanoporous Smectic Liquid Crystal Polymer Networks as Efficient and Selective Adsorbents. *Adv. Funct. Mater.*, **2014**, *24* (32): 5045-51.

116. Dasgupta, D., Shishmanova, I. K., Ruiz-Carretero, A., Lu, K., Verhoeven, M., van Kuringen, H. P., Schenning, A. P. Patterned Silver Nanoparticles Embedded in a Nanoporous Smectic Liquid Crystalline Polymer Network. *J. Am. Chem. Soc.*, **2013**, *135* (30): 10922-5.

117. Prevot, M. E., Andro, H., Alexander, S. L. M., Ustunel, S., Zhu, C., Nikolov, Z., Hegmann, E. Liquid Crystal Elastomer Foams with Elastic Properties Specifically Engineered as Biodegradable Brain Tissue Scaffolds. *Soft Matter.*, **2018**, *14* (3): 354-60.

118. Luo, C., Chung, C., Traugutt, N. A., Yakacki, C. M., Long, K. N., Yu, K. 3D Printing of Liquid Crystal Elastomer Foams for Enhanced Energy Dissipation Under Mechanical Insult. *ACS Appl. Mater. Interfaces*, **2021**, *13* (11): 12698-708.

119. Mistry, D., Traugutt, N. A., Sanborn, B., Volpe, R. H., Chatham, L. S., Zhou, R., Yakacki, C. M. Soft Elasticity Optimises Dissipation in 3D-printed Liquid Crystal Elastomers. *Nat. Commun.*, **2021**, *12* (1): 6677.

120. Wang, M., Song, Y., Bisoyi, H. K., Yang, J. F., Liu, L., Yang, H., Li, Q. A Liquid Crystal Elastomer-Based Unprecedented Two-Way Shape-Memory Aerogel. *Adv. Sci.*, **2021**, *8* (22): e2102674.

121. Zhan, Y., Broer, D. J., Liu, D. Perspiring Soft Robotics Skin Constituted by Dynamic Polarity-Switching Porous Liquid Crystal Membrane. *Adv. Mater.*, **2023**, *35* (12): e2211143.

CHAPTER 2. POROUS LIQUID CRYSTALLINE NETWORKS WITH HYDROGEL-LIKE ACTUATION AND RECONFIGULE FUNCTION

2.1 About this Project

This is the first work accomplished in the thesis. A main-chain liquid crystal polymer previously reported by our group was used to prepare porous LCE actuator through the templating method. An important finding about the preparation conditions has been made during this work. In order to maintain the reversible deformation of porous LCE actuator, it is imperative to complete first the actuator preparation with inorganic nanoparticles in place and then proceed with their removal through chemical etching. In other words, $CaCO_3$-loaded LCE film needs to be mechanically stretched to induce the alignment of mesogens and subjected to full photo-crosslinking using UV light, and only afterwards, etching can be carried out. Etching before crosslinking will lead to the loss of reversible deformation. The porous LCE actuator thus obtained was found to exhibit hydrogel-like swelling in water, meaning that the presence of pores makes the initially hydrophobic LCE behave like conventional hydrogel. The residual ions after etching and the paths via pore channels were identified as the cause for the improved affinity between the LCE actuator and water molecules. Thanks to the actuation through either water absorption-desorption or order-disorder phase transition of the mesogens, 3D shape transformations were demonstrated. Moreover, we demonstrated the concept of LCE actuator with reconfigurable functions. By making use of the large swelling capability in aqueous solution of porous actuator, different functional additives can be introduced into the voids or pore channels at different time in the same LCE actuator through a loading-removal-reloading process.

2.2 Contributions

This work was published in *Angewandte Chemie,* 2022, 61, e202116689 (DOI: 10.1002/anie.202116689) by Jie Jiang, Li Han, Feijie Ge, Yaoyu Xiao, Ruidong Cheng, Xia Tong, and Yue Zhao. The research was conducted in Université de Sherbrooke under the supervision of Prof. Yue Zhao. Prof. Zhao and I designed the experiments. I prepared porous LCE films and actuators. I carried out the experiments, collected and analyzed most data, demonstrated novel swelling behavior, and designed all reconfigurable functions. Li Han and Fejie Ge helped me with the synthesis of the liquid crystal monomers and polymers. Yaoyu Xiao helped me with the editing of the videos reported in this project. Ruidong Cheng helped me draw some of the figures in the publication. Xia Tong assisted me in operating laser sources and gave me many useful suggestions on characterization. I wrote the first draft of the manuscript and Prof. Zhao revised and finalized this paper. Please note that the term of liquid crystallin networks (LCN) used in this publication is the same as LCE used elsewhere in the thesis.

2.3 Paper Published in *Angewandte Chemie,* 2022, 61, e202116689.

Porous Liquid Crystalline Networks with Hydrogel-Like Actuation and Reconfigurable Function

Jie Jiang, Li Han, Feijie Ge, Yaoyu Xiao, Ruidong Cheng, Xia Tong, and Yue Zhao*

Département de Chimie, Université de Sherbrooke, Sherbrooke, Québec, J1K 2R1, Canada.

*E-mail: yue.zhao@usherbrooke.ca

2.3.1 Abstract

A porous liquid crystalline network (LCN), prepared using a template method, was found to exhibit peculiar actuation functions. The creation of porosity makes the initially hydrophobic LCN behave like a hydrogel, capable of absorbing a large volume of water (up to ten times the sample size of LCN). When the amount of absorbed water is relatively small (about 100% swelling ratio), the porous LCN displays anisotropic swelling in water and, in the same time, the retained uniaxial alignment of mesogens ensures thermally induced shape change associated with LC-isotropic phase transition. Combining the characteristic actuation mechanisms of LCN (order-disorder transition of mesogens) and hydrogel (water absorption), such porous LCN can be explored for versatile stimuli-triggered shape transformations. Moreover, the porosity enables loading/removal/reloading of functional fillers such as ionic liquid, photothermal dye and fluorophore, which imparts a same porous LCN actuator with reconfigurable functions such as ionic conductivity, light-driven locomotion, and emissive color.

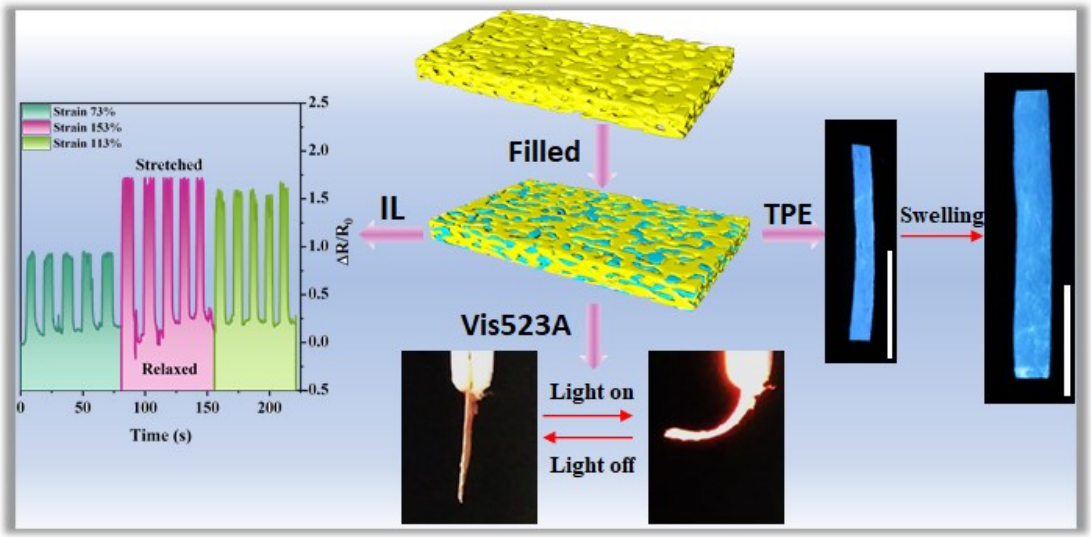

2.3.2 Introduction

Nature provides vivid examples of stimuli-triggered shape changes and motions both in plants (like flytrap and pinecone) and in the animal world (like octopus body). These natural systems have inspired researchers to develop soft responsive materials for applications in many fields such as soft robotics[1], artificial muscle[2], sensors[3], oscillators[4] and energy generators[5]. Stimuli-responsive polymeric materials are promising candidates for mimicking these dynamic shape change and motion functions. In particular, liquid crystalline polymers (LCPs)[6], hydrogels[7] and shape-memory polymers[8] have been much studied in recent years, which have different actuation mechanisms. While hydrogels change shape and size based on the amount of absorbed water, and shape-memory polymers deform as a result of activated chain relaxation and strain energy release, the reversible shape change of LCPs is generally dictated by an order-disorder phase transition of mesogens. By crosslinking an LCP in a macroscopically oriented state of mesogens or LC director field, liquid crystalline network (LCN) actuators can be prepared, which are capable of displaying large shape changes, producing mechanical forces and executing a variety of movements like walking[2b, 6a, 9], rolling[10], swimming[11], jumping[12] under the stimulation of light[4c, 8b, 13], electric field[6a, 14], heat[15], humidity[16], and magnetic field.[17] In terms of materials research, most effort has been dedicated to designing new molecular structures of LCNs for sought-after properties or functions. Examples include interpenetrating LCNs for superior actuation forces[18] and Diels-Alder dynamic LCNs for self-locking of oriented mesogens in actuator processing[19], to name only a few. For a given LCN, diverse approaches have also been exploited for actuator applications, such as using it in a bilayer structured actuator, and loading or coating it with a kind of photothermal agents to enable light-triggered actuation. Despite the numerous progresses, novel strategies for developing LCN materials are needed. Herein, we show that making porous LCNs is an interesting means to generate unusual properties and new functions.

Porous polymers may possess high porosity, large surface area and low density. By combining the advantages of porous media and polymeric materials, they have applications in such fields as separation membrane, battery separator and sensor support. Reliable methods for preparation of porous polymers include direct templating[20], "Breath Figure"[21], non-solvent induced phase separation[20a, 22] and so on. However, porous LCPs have been largely unexplored thus far. There are several studies with an interest on biomedical applications. One example is the use of porous LCPs as a three-dimensional brain tissue scaffold for cell culture, showing that cell alignment could be promoted by LC order.[23] Notably, several attempts have been made to take advantage of both porous structure and actuation behavior of LCPs to realize shape memory in stimuli-controlled surface topography[24] as well as switchable pore shape and size in porous films[25]. It is thus of interest to know if porous LCPs can be made a materials platform for soft actuators.

2.3.3 Results and Discussion

In the present study, a simple template method was utilized to prepare a porous LCN. Figure 1 shows the preparation procedure and some characterization results of the porous LCN. The used LCP bears biphenyl moieties as mesogens and cinnamyl units for photocrosslinking (Figure 1a), whose synthesis was reported previously[15a]. As depicted schematically in Figure 1b, the preparation of a porous LCN film consists in three steps, in the order: 1) making an LCP film (through solution casting followed by compression-molding) with dispersed $CaCO_3$ particles (0.8 μm unless otherwise stated), 2) mechanically stretching the film to induce uniaxial orientation of mesogens and then photocrosslinking the polymer under strain, leading to LCN, and 3) immersing the LCN film in hydrochloric acid (HCl, 12M) for chemical etching that removes $CaCO_3$ particles and generates pores in the LCN. It is noted that no hydrolysis of ester bonds in the LCP or LCN was found (Figure S1). While details of the preparation procedure are given and discussed in Supporting Information, we mention here that in order to form the pores, it is necessary to crosslink the

composite film first and carry out the etching afterwards. If the sequence is reversed, i.e., etching first followed by crosslinking, apparently no significant porosity in the LCN film can be obtained (Figure S2a). Besides, the porous LCN after etching retains similar mechanical properties except a reduced yield stress (Figure S3). To investigate the effect of porosity, different $CaCO_3$ contents (10, 20 and 40 wt% of the polymer) were used, resulting in porous LCN films denoted as LCN-10, LCN-20 and LCN-40 (the number corresponds to the used wt% of $CaCO_3$). For the sake of comparison, non-porous LCN, LCN-0, was also prepared under the same conditions (subjected to etching). Unless otherwise stated, porous LCN films were prepared using 330% uniaxial stretching (at 51 ºC) and photocrosslinked by UV light exposure to both sides (325 nm, 90 $mW.cm^{-2}$) through photodimerization of cinnamyl moieties (Figure S4), resulting in a typical thickness of about 80 μm. Figure 1c shows the XRD 2D-patterns and diffractograms of an LCN-40 film before and after chemical etching, which confirms complete removal of solid $CaCO_3$ as the diffraction ring and peak at $2\theta=23.4^{o}$ from $CaCO_3$ crystal[27] are disappeared after etching. By contrast, the diffraction arcs and peak around $2\theta=20.8^{o}$ appear intact, indicating that the stretching-induced alignment of mesogens are retained in the porous LCN. The porosity from the voids after $CaCO_3$ removal was estimated using a method based on *n*-butanol uptake (details in Supporting Information) and the results are shown in Figure 1d. The porosity increases with increasing the amount of $CaCO_3$ in the LCN and reaches nearly 30% for LCN-40. The SEM cross-section image of LCN-40 in the inset shows pores channels in the film, with an average pore size of 350 nm (Figure S5). Comparing the DSC heating and cooling curves of LCN-40 with LCN-0 (non-porous) in Figure 1e, even with a large porosity, the glass transition temperature (T_g) and nematic-isotropic (order-disorder) phase transition temperature of the LCN are not much affected, appearing at ~ 25 ºC and ~ 58 ºC, respectively. However, the nematic-isotropic phase transition enthalpy (ΔH_{NI}) does decrease with increasing the porosity (Figure S6 and Table S1). As shown in Figure 1f, the presence of

pores also causes visually noticeable change to the LCN film. While LCN-0 appears translucent, LCN-40 is highly opaque due to light scattering by the voids in the film.

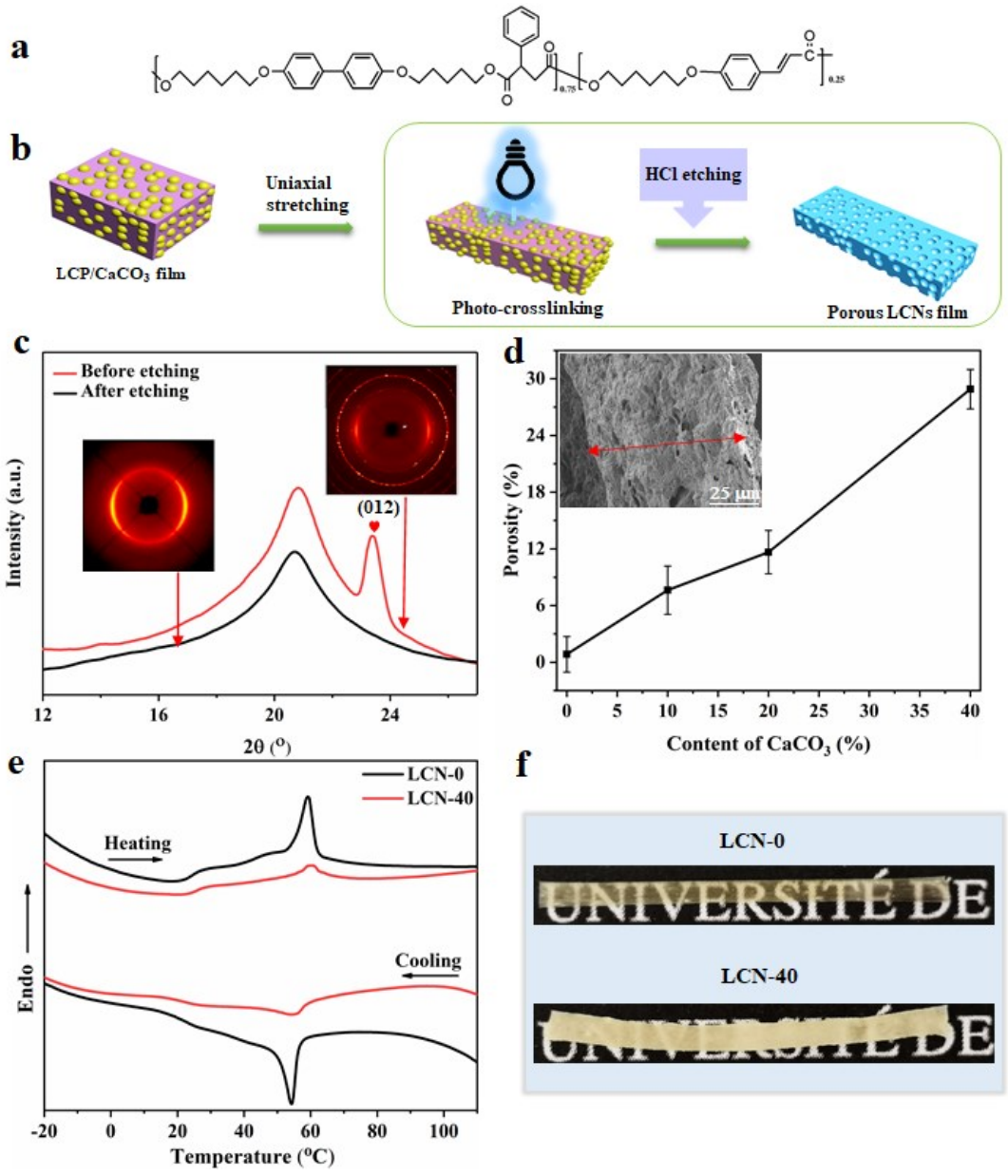

Figure 1 (a) Chemical structure of the used liquid crystalline polymer. (b) Schematic illustration of the preparation of porous LCN film through a templating method. (c) 1D-XRD diffractograms and 2D-XRD patterns (inset photos) of LCN-40 before and after etching.

(d) Porosity of LCN-based films with different contents of $CaCO_3$ (inset is SEM cross-section image of LCN-40, the red arrow indicates the film thickness). (e) DSC traces of cooling (first scan) and heating (second scan) of LCN-0 and LCN-40. (f) Photos of LCN-0 and LCN-40 films.

Despite a significant porosity in the porous LCN, it exhibits the same reversible shape change upon order-disorder phase transition as the non-porous LCN counterpart: a monolithic strip contracts on heating to isotropic state and extends on cooling to LC phase (Figure S7a), or its bilayer actuator with a passive polymer bends and unbends on heating/cooling cycles (Figure S8). Although the overall actuation behaviors are not much affected by the presence of pores, the magnitude of actuation, as usually measured by the reversible actuation degree (length in LC phase over length in isotropic state, or achievable bending angle), is reduced to some extent for porous LCN (Figure S7b). This is no surprise because the voids in the LCN, which cannot contribute to the actuation force, could affect the order state of the mesogens and contribute to stress relaxation during thermal actuation. A reduced order parameter in porous LCN films, especially for LCN-40, was indeed revealed by polarized infrared spectroscopic and XRD measurements (Figure S9). While it is interesting to confirm that porous LCN can retain the basic actuation behavior of the non-porous counterpart, it would be more useful if the porosity generates new properties and functions which the non-porous LCN does not possess. What is reported below is such an unexpected finding for porous LCN. Although the LCN is hydrophobic, the porous LCN can swell in water like a hydrogel, enabling actuation through both order-disorder transition of mesogens and absorption of water. It should be emphasized that many water-absorbing LCNs were obtained in previous studies through introduction of hydrophilic species either in the LCN structure or in the material formulation[28-33,16c]. The most notable approaches include using benzoic acid dimer as the mesogen in LCN to afford pH-dependent water absorption[28-29], incorporating mesogens in the backbone of a hydrogel network[31], and making

an LCN-hydrogel interpenetrating network (IPN)[32]. However, water absorption through creation of pores in hydrophobic LCN has not been reported. Perhaps more interestingly is the feature that the pores in LCN actuator can be used to load a functinal filler to endow the actuator with a specific function, while the filler can be washed out later on and the actuator is refilled with another active filler to enable a different function. We demonstrate such function reconfigurability or multiple refunctionalizations for a same LCN actuator.

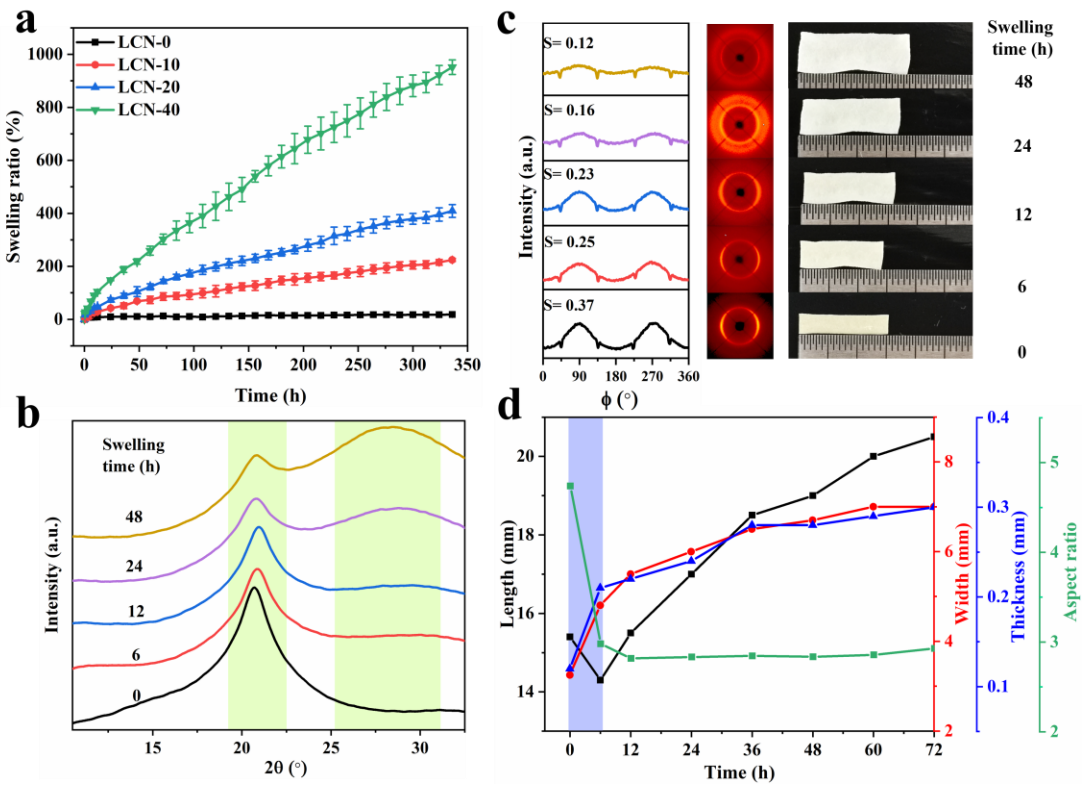

Figure 2 (a) Swelling ratio vs. time for non-porous and porous LCN films immersed in water at room temperature. (b) XRD diffractograms of an LCN-40 film immersed in water for various swelling times. (c) 2D XRD patterns, azimuthal diffraction profiles (2θ=17.6°-20.9° for nematic order), order parameters and photos for an LCN-40 film swollen in water after different times. (d) Change of an LCN-40 strip in length, width, thickness, and aspect ratio (length/width) as a function of immersion time.

Figure 2a shows the plots of swelling ratio versus immersion time for the porous and non-porous LCN at room temperature. While the latter displays no swelling, the porous LCN samples swell slowly but continuously over time, and at a given immersing time the swelling is more prominent for LCN having a larger porosity. As can be seen from the XRD diffractograms in Figure 2b, within the first 48h of immersion, a broad peak at $2\theta = 28.7^{o}$ belonging to the amorphous water[34], becomes increasingly prominent over time. For the same samples, Figure 2c shows their 2D XRD pattern, azimuthal diffraction profile at the wide-angle reflection of nematic order, calculated order parameter S, as well as their photos. Although the macroscopic orientation of mesogens decreases upon swelling from water absorption, the LC order is not completely lost even after 48 h of water absorption reaching a swelling ratio of about 200%. Figure 2d shows the plots of changes in the length, width, thickness and aspect ratio (length/width) of an LCN-40 strip over the swelling time in water, revealing a peculiar swelling behavior of porous LCN. While both the width and thickness of the strip, i.e., in the directions perpendicular to the mesogen and chain backbone orientation direction in the actuator, expand from the beginning of swelling and become gradually wider and thicker over time, the length of the strip first decreases in the first 6 h and then increases continuously. In term of the length to width aspect ratio, it drops in the first 6 h and, beyond this time, remains essentially constant over the 72 h monitoring period. Normally, when heated into the isotropic state, non-porous LCN strip contracts in length and extends in width, as a result of order-disorder phase transition. The shape change of LCN-40 upon water absorption within the first few hours apparently resembles the thermally induced shape change of LCN-0. However, unlike non-porous LCN strip in isotropic phase whose LC order is lost, the porous LCN strip retains much of LC order after 6 h water absorption (Figure 2c). This result indicates that the early stage of the hydrogel-like swelling of the porous LCN strip is an anisotropic swelling process that features a predominant enlargement of the strip in the transversal directions, for which the insertion of water molecules needs mainly to overcome the intermolecular interactions between oriented

mesogens and polymer chains; while in the length direction of the strip, the swelling by water results in a relaxation of aligned mesogens and chain backbone. At the end of the anisotropic swelling, even though some LC order remains, the structurally rearranged porous LCN swells essentially like an isotropic hydrogel, increasing its size the same way in all directions, as revealed by a constant length to width aspect ratio.

Since the porous LCN retains a significant degree of orientation of mesogens after absorption of a large amount of water (about 200% water in LCN-40), we investigated how the presence of water could affect the actuation. The results show that porous LCN strips with different amounts of water change their shapes based on the interplay of volume variation due to water absorption like hydrogel and shape changing arising from order-disorder phase transition of mesogens like LCN (see Figure S10 and related discussion). Sophisticated 3D shape transformations can be obtained using the actuation of hydrogel-like LCN. Figure 3a shows an example making use of monolithic film with asymmetrical crosslinking of the two sides. A "fishing net" was assembled with eight LCN-40 strips whose two sides were photocrosslinked under UV light exposure for 40 min (top side) and 80 min (bottom side), respectively. It was found that LCN-40 photocrosslinked for 80 min swollen in water more importantly than the sample photocrosslinked for 40 min (Figure S11). This behavior contrasts with normal hydrogels, for which higher crosslinking means less swelling. We postulate that porous LCNs need pores in a hydrophobic matrix to promote water absorption, while higher crosslinking prior to $CaCO_3$ particle removal can better stabilize the pore structure and thus favors the swelling in water. When the "fishing net" was immersed in water at room temperature, with more water absorbed by the bottom side than the top side, the initially flat net curled over time to form a closing bowl shape and the net mesh shrunk from 4 mm^2 to 1 mm^2. After water removal, the size and shape of the net could return to the original state. Figure 3b shows the shape transformation of a bilayer actuator. The top layer is a non-porous LCN strip with mesogens oriented along the long axis, while the bottom layer is the porous LCN-40 film. Such a bilayer actuator can exhibit separate shape

changes through hydrogel- and LCN-based actuation mechanisms. As shown, upon immersion in water at room temperature, the top layer (LCN) cannot absorb water and is passive, but the bottom layer (LCN-40) absorbs water and swells over time. As the interface-restricted asymmetrical expansion of the bilayer goes on, although some longitudinal deformation occurs, bending in the width direction dominates, which rolls the flat strip into a tube with the non-absorbent LCN as the inner layer. Subsequently, when the tube is heated in an oven to 65 °C, the order-disorder transition of mesogens induces contraction, which is more important for the inner LCN layer than the outer swollen LCN-40 layer, squeezes and winds the tube into a twisted structure (Movie S1). This example demonstrates the effect of combining the two shape change mechanisms of hydrogel-like porous LCN actuators.

More interestingly, the presence of voids and the capability of water absorption can be explored to impart the porous LCN actuator with functionalities which neither non-porous LCN nor hydrogel alone can possess. In what follows, we show that the pores in porous LCN actuator can be used to load an active filler and, later on, reload another active filler after washing out the previous one, demonstrating reconfigurable function with a same porous actuator. First, a porous LCN-40 strip was immersed and swollen in an ionic liquid (IL)/water (1:1) mixture for 48 h, IL being 1-butyl-3-methylimidazolium tetrafluoroborate ($BMIMBF_4$). By doing so, IL was carried through water into the porous LCN matrix to endow the actuator, denoted as LCN-40-IL, with electrical response. Indeed, the sample became electrically responsive due to ionic conductivity (setup in Figure S12a). The relative resistance (resistance variation normalized by initial resistance) measured with dry sample (water removed by heating at 60 °C) at room temperature and 70 °C for three consecutive heating/cooling cycles is shown in Figure 4a (left part), with higher conductivity at elevated temperature. By contrast, porous LCN-40 swollen in pure water without IL is not conductive (electrical resistance is too high to measure with the multimeter with a

resistance limit of 120 MΩ). The wet sample of LCN-40-IL is also conductive (Figure S12b). What's more, as can be seen from the inset photos, the electrically responsive porous LCN actuator can still exhibit thermally induced reversible shape change (on heating to 70 ^{o}C, the LCN-40-IL strip shrinks by about 27%). This experiment demonstrates that the hydrogel-like absorption of water of the porous LCN actuator can be used to introduce IL, which confers the LCN actuator with the electrical response capability (impedance measurements in Figure S13). Similar to LCN containing liquid metals (LMs), such electrical response can be used for sensing applications in deformable electronics[35,36]. Figure 4a (right part) shows the relative resistance of a dry LCN-40-IL strip subjected to cyclic stretching and relaxation at 70 ^{o}C, which is specific to the magnitude of strain. Afterward, IL in the porous actuator was removed completely through washing using water at room temperature. This can be seen from Figure 4b (left part) comparing the infrared spectra of IL, LCN-40-IL and the latter after washing. The characteristic absorption bands of IL (highlighted) disappeared after washing. The reset porous actuator was then refilled with a photothermal dye (Vis523A) dissolved in ethanol through swelling followed by drying. The presence of the dye in the actuator can be seen from the absorption spectrum after filling (Figure 4b, on the right). This refilling treatment has thus reconfigured the LCN actuator to possess a new targeted function, switching from electrically active (with IL) to photoactive (with dye). As shown in Figure 4c, when glued to a passive polyimide layer, the bilayer actuator bends toward the porous LCN under visible light irradiation due to photothermal effect inducing order-disorder phase transition (Figure S14). Under light on-off cycles, the bilayer on a paper, with the porous LCN as the bottom side, undergoes arching-up (light on) and flattening-down (light off) deformation and moves like caterpillar due to friction bias[16b] (with a moving speed of about 18 mm/min) (Movie S2). This filling/washing/refilling process was carried out one more time to replace the photothermal dye by tetraphenylethylene (TPE) in the porous actuator. Since TPE is a dye with aggregation-induced emission (AIE), the characteristic emission of blue light from the refilled actuator under

UV light excitation (350 nm), as shown in Figure 4d (left part), implies that the dye was not dissolved in the LCN matrix, rather it was likely present in the pores. The actuator strip can emit blue fluorescence before and after swelling in water (200% swelling ratio) (Figure 4d, right part).

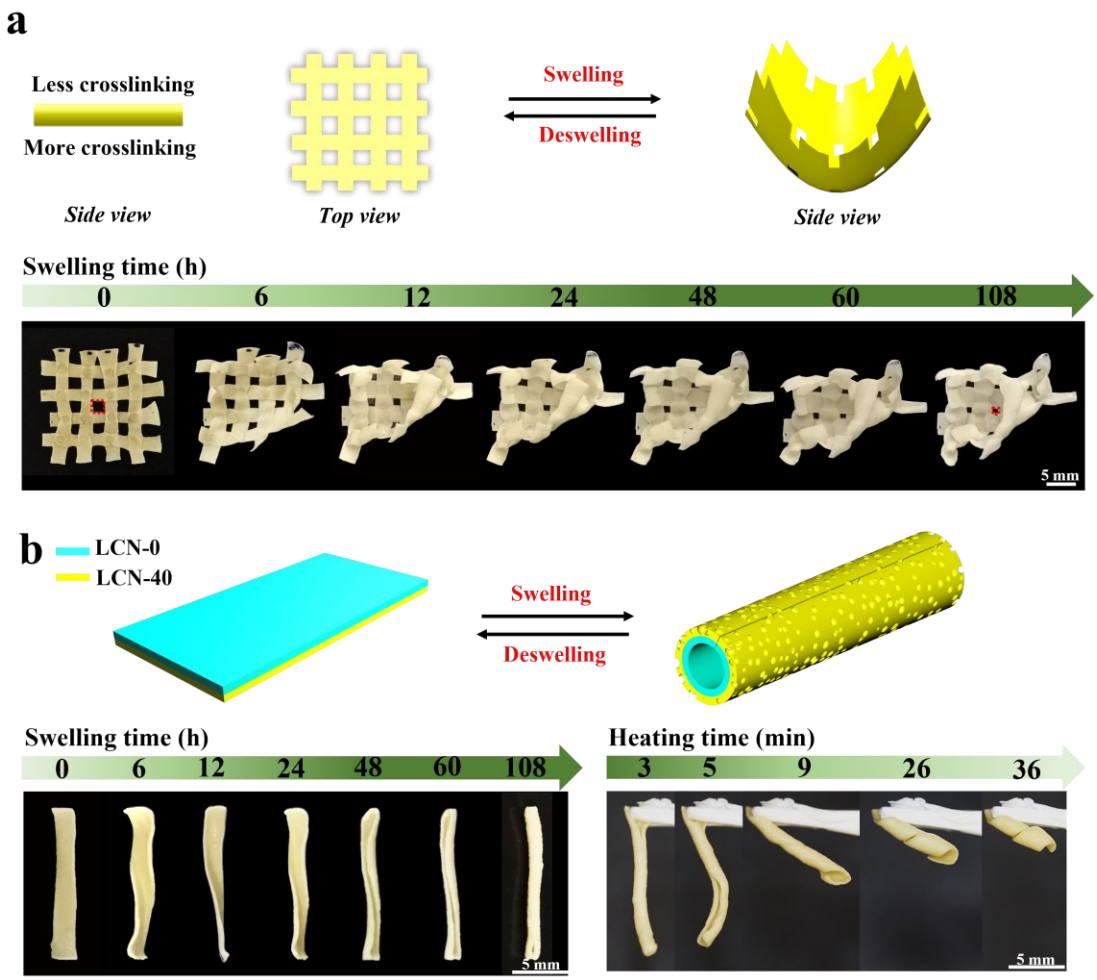

Figure 3 (a) Schematics and photos showing the asymmetrical water-absorption-induced transformation of a "fishing net" assembled with eight monolithic, porous LCN-40 actuator strips having different crosslinking densities on the bottom and top sides (strip size: 20 mm x 2 mm x110 μm). (b) Schematics and photos showing the two-step water-absorption and order-disorder phase transition-induced shape transformation of a bilayer actuator made of non-porous LCN as top layer and porous LCN-40 as bottom layer (both layers have the same strip size:1.3 cm x 2 mm x 80 μm).

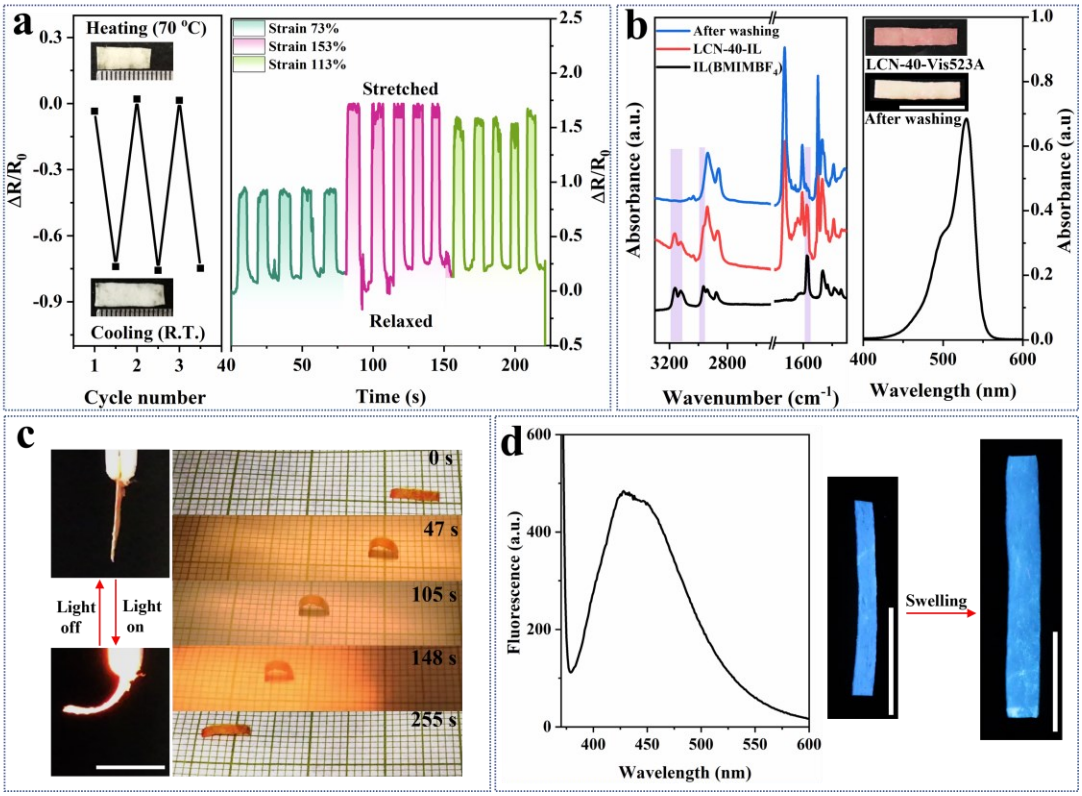

Figure 4 (a) Left: relative resistance at room temperature and 70 °C upon three consecutive heating/cooling cycles for dry LCN-40-IL. The inset photos show thermally induced reversible shape change of the LCN-40-IL actuator strip. Right: resistance changes of LCN-40-IL in response to mechanical stretching and relaxation. (b) Left: infrared spectra of IL ($BMMBF_4$), LCN-40-IL and LCN-40-IL after washing. Right: absorption spectrum of the reset LCN-40 after refilling with a photothermal dye (Vis523A). The inset photos show the actuator before and after dye refilling (scale bar: 0.5 cm). Note: since the absorption spectrum could not be recorded from the solid opaque film, it was taken from an ethanol solution with dye-filled film immersed for extraction. (c) Left: photos showing visible light on/off-induced bending/unbending of a bilayer actuator comprising LCN-40 (80 μm thickness) loaded with Vis523A and a passive polyimide Layer (bending toward the LCN-40 side regardless of the light beam direction). Right: Photos showing locomotion of a bilayer actuator (LCN-40 side down) under visible light on/off cycles through arching-up and

flattening-down (actuator size: 6.0 mm x 1.5 mm x 110 μm, light intensity: 0.6 W/cm^2). (d) Left: fluorescence emission spectrum of reset LCN-40 after refilling with tetraphenylethylene (TPE) (λex= 350 nm). Right: photographs under illumination of UV light (365 nm) of LCN-40-TPE before and after swelling in water (scale bar: 0.5 cm).

Before concluding, the question should be discussed of why the formation of pores in the hydrophobic LCN makes it absorb a large amount of water like hydrogel. As pointed out above, porous LCN swells more in water with higher polymer chain crosslinking prior to removal of $CaCO_3$ particles by HCl etching. This observation indicates the importance of a stable pore structure in the LCN for water absorption. With the polymer immersed in water, should the pore surface has an affinity with water molecules, absorption of water by capillary effect could develop through pore channels[37]. As the LCN is a soft elastomer, it can expand to enlarge the pores and accommodate water molecules filling inside. We conducted contact angle measurements and found greater affinity with water for LCN with higher porosity (66º and 86º water contact angle for LCN-40 and LCN-0, respectively (Figure S15). On the other hand, although no residual solid $CaCO_3$ was found after etching (Figure 1c), it is possible to have ions remained in the porous LCN. To gain a better understanding, we conducted energy-dispersive X-ray (EDX) measurements on LCN-40 samples washed for different times following HCl etching (10 min, 12 h and 48 h) and, for comparison, on LCN-40 samples prepared with etching before crosslinking and washed for 10 min and 48 h. Their swelling behaviors were also monitored and compared. Two main findings are as follows. First, residual ions (Ca^{2+} and Cl^{-1}) were present in porous LCN-40, and their amounts decreased with longer washing time after etching. The Ca^{2+} residual was just below a third of the initial amount before etching (wt% or atomic%) with 10 min washing and a quarter after 12 h washing, while extended washing time of 48 h resulted in little further decrease (Figure S16). The swelling ratios for the samples washed for 12 h and 48 h were lower than that washed for 10 min but remained substantial (Figure S17). Secondly,

for LCN-40 samples subjected to etching before photocrosslinking, significant residual ions were also found after 10 min washing and reduced after 48 h washing, while the two samples swollen little in water. SEM cross-section and surface images of the sample with etching before crosslinking showed absence of pores and firm surface, in contrast to the sample with crosslinking before etching (Figure S18). These results indicate the importance of having stable pores in LCN for hydrogel-like water absorption and shed light on the mechanism. Essentially, the absorption of water requires the existence of interconnected pore channels with large interfaces and an affinity (favorable intermolecular interactions) between pore surfaces and water molecules, while the presence of residual ions help increasing the affinity and thus enhancing the ability of porous LCN to absorb water[38]. This mechanism also accounts for the slow absorption of water. Interestingly, the mechanism suggests the possibility of purposely using ions to promote the hydrogel-like behavior of porous LCN actuator. Finally, we mention that energy-dispersive spectroscopy (SEM-EDS) was used to examine the dispersion of $CaCO_3$ particles in LCN-40 before etching, showing good dispersion (Figure S19); and the effect of the size of $CaCO_3$ particles on actuation and water absorption of porous LCN was also investigated (Figure S20).

2.3.4 Conclusions

In conclusion, we have employed a template method to prepare porous LCN actuators. Although the LCN is hydrophobic, the presence of pores results in absorption of water and makes the LCN actuator swell in water like hydrogel. A substantial degree of alignment of mesogens was found to remain in the porous actuator upon water absorption (up to 200% swelling ratio). The coexistence of alignment of mesogens and porosity imparts the porous LCN actuator with the capability of changing reversibly its shape through either order-disorder phase transition like its non-porous LCN counterpart or water absorption like hydrogel (see schematic recapitulation in Figure S21). Combining the two actuation mechanisms can be explored for sophisticated 3D shape transformations. More interestingly, the

pores facilitate the loading, removal and reloading of active fillers in a same LCN actuator, which enables reconfiguration of the sought-after function. This interesting feature has been exemplified by filling a porous LCN with IL, rendering the actuator electrically responsive. The resulting LCN actuator has potential for deformable electronics application by having both sensing and actuation capabilities. After removal of IL and refilling with a photothermal dye, the LCN actuator was made into a light-driven microwalker, which is useful for soft robotics application. Finally, a fluorescent actuator was obtained by replacing the photothermal dye with an AIE dye in the porous LCN through another removal/refilling procedure.

2.4 Supporting Information

Supporting Information is available from the Wiley Online Library or from the author.

2.5 Acknowledgements

Y. Zhao acknowledges the financial support from the Natural Sciences and Engineering Research Council of Canada (NSERC), le Fonds de recherche du Québec: Nature et technologies (FRQNT), and The Centre québécois sur les matériaux fonctionnels. J. Jiang is grateful to China Scholarship Council (CSC) for providing her with a scholarship to study and live in Canada. L. Han, Y. Xiao, and R. Cheng thanks CSC for a scholarship. F. Ge thanks FRQNT and CSC for a scholarship. Dr. D. Fortin is acknowledged for assisting the XRD measurements. We also thank the anonymous referee who suggested the functionalization experiment through washing/refilling.

2.6 Conflict of Interest

The authors declare no conflict of interest.

2.7 Keywords

porous liquid crystalline network •reversible shape change • hydrogel-like swelling • soft actuator • reconfigurable function.

2.8 References

[1] a) T. Ube, K. Kawasaki, T. Ikeda, *Adv. Mater.* **2016**, *28*, 8212-8217; b) T. J. White, D. J. Broer, *Nat. Mater.* **2015**, *14*, 1087-1098; c) F. Ge, Y. Zhao, *Adv. Funct. Mater.* **2019**, *30*, 1901890; d) Y. Zhang, Z. Wang, Y. Yang, Q. Chen, X. Qian, Y. Wu, H. Liang, Y. Xu, Y. Wei, Y. Ji, *Sci. Adv.* **2020**, *6*, eaay8606; e) S. Li, H. Bai, R. F. Shepherd, H. Zhao, *Angew. Chem. Int. Ed.* **2019**, *58*, 11182-11204; f) H. Kim, J. A. Lee, C. P. Ambulo, H. B. Lee, S. H. Kim, V. V. Naik, C. S. Haines, A. E. Aliev, R. Ovalle-Robles, R. H. Baughman, T. H. Ware, *Adv. Funct. Mater.* **2019**, *29*; g) S. J. Asshoff, F. Lancia, S. Iamsaard, B. Matt, T. Kudernac, S. P. Fletcher, N. Katsonis, *Angew. Chem.* **2017**, *56*, 3261-3265.

[2] a) L. Liu, M. H. Liu, L. L. Deng, B. P. Lin, H. Yang, *J. Am. Chem. Soc.* **2017**, *139*, 11333-11336; b) X. Lu, H. Zhang, G. Fei, B. Yu, X. Tong, H. Xia, Y. Zhao, *Adv. Mater.* **2018**, *30,* 1706597.

[3] a) C. Larson, B. Peele, S. Li, S. Robinson, M. Totaro, L. Beccai, R. Shepherd, *Science* **2016**, *351*, 1071-1074; b) C. Ohm, M. Brehmer, R. Zentel, *Adv. Mater.* **2010**, *22*, 3366-3387.

[4] a) H. Zeng, M. Lahikainen, L. Liu, Z. Ahmed, O. M. Wani, M. Wang, H. Yang, A. Priimagi, *Nat. Commun.* **2019**, *10*, 1-9; b) R. Lan, J. Sun, C. Shen, R. Huang, Z. Zhang, L. Zhang, L. Wang, H. Yang, *Adv. Mater.* **2020**, e1906319; c) A. H. Gelebart, G. Vantomme, E. W. Meijer, D. J. Broer, *Adv. Mater.* **2017**, *29,* 1606712; d) K. Kumar, C. Knie, D. Bleger, M. A. Peletier, H. Friedrich, S. Hecht, D. J. Broer, M. G. Debije, A. P. Schenning, *Nat. Commun.***2016**, *7*, 11975.

[5] a) Y. Xiong, L. Zhang, P. Weis, P. Naumov, S. Wu, *J. Mater. Chem. A* **2018**, *6*, 3361-3366; b) G. L. Ma M, Anderson DG, Langer R., *Science* **2013**, *339*, 186-189; c) L. Zhang, P. Naumov, *Angew. Chem.* **2015**, *54*, 8642-8647. d) X. Pang, J. A. Lv, C. Zhu, L. Qin, Y. Yu, *Adv. Mater.* **2019**, *31*, e1904224.

[6] a) Y. Y. Xiao, Z. C. Jiang, X. Tong, Y. Zhao, *Adv. Mater.* **2019**, *31*, e1903452; b) T. Ikeda, J. Mamiya, Y. Yu, *Angew. Chem.* **2007**, *46*, 506-528; c) Z. C. Jiang, Y. Y. Xiao, Y. Zhao, *Adv. Opt. Mater.* **2019**, *7*, 1900262; d) R. C. Verpaalen, M. Pilz da Cunha, T. A. Engels, M. G. Debije, A. P. Schenning, *Angew. Chem. Int. Ed.* **2020**, *59*, 4532-4536;e) J. A. Lv, Y. Liu, J. Wei, E. Chen, L. Qin, Y. Yu, *Nature* **2016**, *537*, 179-184; f) H. Yu, T. Ikeda, *Adv. Mater.* **2011**, *23*, 2149-2180.

[7] a) X. Le, W. Lu, J. Zhang, T. Chen, *Adv. Sci. News* **2019**, *6*, 1801584; b) X. P. Hao, Z. Xu, C. Y. Li, W. Hong, Q. Zheng, Z. L. Wu, *Adv. Mater.* **2020**, e2000781.

[8] a) G. Li, S. Wang, Z. Liu, Z. Liu, H. Xia, C. Zhang, X. Lu, J. Jiang, Y. Zhao, *ACS Appl. Mater.Interfaces* **2018**, *10*, 40189-40197; b) A. Rose, Z. Zhu, C. F. Madigan, T. M. Swager, V. Bulović, *Nature* **2005**, *434*, 876-879.

[9] a) H. Zeng, P. Wasylczyk, C. Parmeggiani, D. Martella, M. Burresi, D. S. Wiersma, *Adv. Mater.* **2015**, *27*, 3883-3887; b) Z. Wang, K. Li, Q. He, S. Cai, *Adv. Mater.* **2019**, *31*, e1806849.

[10] a) M. Yamada, M. Kondo, J. Mamiya, Y. Yu, M. Kinoshita, C. J. Barrett, T. Ikeda, *Angew. Chem. Int. Ed.* **2008**, *47*, 4986-4988; b) J. J. Wie, M. R. Shankar, T. J. White, *Nat. Commun.* **2016**, *7*, 1-8; c) X. Lu, S. Guo, X. Tong, H. Xia, Y. Zhao, *Adv. Mater.* **2017**, *29*, 1606467; d) C. Ahn, K. Li, S. Cai, *ACS Appl. Mater. Interfaces* **2018**, *10*, 25689-25696.

[11] a) S. Palagi, A. G. Mark, S. Y. Reigh, K. Melde, T. Qiu, H. Zeng, C. Parmeggiani, D. Martella, A. Sanchez-Castillo, N. Kapernaum, F. Giesselmann, D. S. Wiersma, E. Lauga, P. Fischer, *Nat. Mater.* **2016**, *15*, 647-653; b) M. Camacho-Lopez, H.

Finkelmann, P. Palffy-Muhoray, M. Shelley, *Nat. Mater.* **2004**, *3*, 307-310; c) S. Ma, X. Li, S. Huang, J. Hu, H. Yu, *Angew. Chem. Int. Ed.* **2019**, *131*, 2655-2659.

[12] a) H. Shahsavan, A. Aghakhani, H. Zeng, Y. Guo, Z. S. Davidson, A. Priimagi, M. Sitti, *Proc. Natl. Acad. Sci. U.S.A.* **2020**, *117*, 5125-5133; b) H. Arazoe, D. Miyajima, K. Akaike, F. Araoka, E. Sato, T. Hikima, M. Kawamoto, T. Aida, *Nat. Mater.* **2016**, *15*, 1084-1089.

[13] a) J. Chen, F. K.-C. Leung, M. C. A. Stuart, T. Kajitani, T. Fukushima, E. van der Giessen, B. L. Feringa, *Nat. Chem.* **2018**, *10*, 132-138; b) Z. C. Jiang, Y. Y. Xiao, X. Tong, Y. Zhao, *Angew. Chem. Int. Ed.* **2019**, *58*, 5332-5337; c) X. Lu, C. P. Ambulo, S. Wang, L. K. Rivera-Tarazona, H. Kim, K. Searles, T. H. Ware, *Angew. Chem.* **2021**, *60*, 5536-5543.

[14] a) C. Lu, Y. Yang, J. Wang, R. Fu, X. Zhao, L. Zhao, Y. Ming, Y. Hu, H. Lin, X. Tao, Y. Li, W. Chen, *Nat. Commun.* **2018**, *9*, 1-11;b) S. Taccola, F. Greco, E. Sinibaldi, A. Mondini, B. Mazzolai, V. Mattoli, *Adv. Mater. Interfaces* **2015**, *27*, 4.

[15] a) R. Yang, Y. Zhao, *Angew. Chem. Int. Ed.* **2017**, *56*, 14202-14206; b) V. Magdanz, G. Stoychev, L. Ionov, S. Sanchez, O. G. Schmidt, *Angew. Chem. Int. Ed.* **2014**, *53*, 2673-2677.

[16] a) W. Hu, J. Sun, Q. Wang, L. Zhang, X. Yuan, F. Chen, K. Li, Z. Miao, D. Yang, H. Yu, H. Yang, *Adv. Funct. Mater.* **2020**, *30*, 2004610; b) Y. Liu, B. Xu, S. Sun, J. Wei, L. Wu, Y. Yu, *Adv. Mater.* **2017**, *29*, 1604792; c) R. Lan, J. Sun, C. Shen, R. Huang, L. Zhang, H. Yang, *Adv. Funct. Mater.* **2019**, *29*, 1900013.

[17] H. W. Huang, M. S. Sakar, A. J. Petruska, S. Pané, B. J. Nelson, *Nat. Commun.* **2016**, *7*, 1-10.

[18] H. F. Lu, M. Wang, X. M. Chen, B. P. Lin, H. Yang, *J. Am. Chem. Soc.* **2019**, *141*, 14364-14369.

[19] Z. C. Jiang, Y. Y. Xiao, L. Yin, L. Han, Y. Zhao, *Angew. Chem.* **2020**, 132, 4955-4961.

[20] a) D. Wu, F. Xu, B. Sun, R. Fu, H. He, K. Matyjaszewski, *Chem. Rev.* **2012**, *112*, 3959-4015; b) J. Wu, F. Xu, S. Li, P. Ma, X. Zhang, Q. Liu, R. Fu, D. Wu, *Adv. Mater.* **2019**, *31*, e1802922; c) W. Zhang, Q. Zhao, J. Yuan, *Angew. Chem. Int. Ed.* **2018**, *57*, 6754-6773.

[21] a) W. Wang, C. Du, X. Wang, X. He, J. Lin, L. Li, S. Lin, *Angew. Chem. Int. Ed.* **2014**, *53*, 12116-12119; b) A. Zhang, H. Bai, L. Li, *Chem.Rev.* **2015**, *115*, 9801-9868; c) M. Hernández-Guerrero, M. H. Stenzel, *Polym. Chem.* **2012**, *3*, 563-577; d) H. Bai, C. Du, A. Zhang, L. Li, *Angew. Chem.* **2013**, *52*, 12240-12255.

[22] G. R. Guillen, Y. Pan, M. Li, E. M. V. Hoek, *Ind. Eng. Chem.Res.* **2011**, *50*, 3798-3817.

[23] M. E. Prevot, H. Andro, S. L. M. Alexander, S. Ustunel, C. Zhu, Z. Nikolov, S. T. Rafferty, M. T. Brannum, B. Kinsel, L. T. J. Korley, E. J. Freeman, J. A. McDonough, R. J. Clements, E. Hegmann, *Soft Matter* **2018**, *14*, 354-360.

[24] C. H. Wu, C. S. Lu, W. L. Chen, S. H. Tung, R. J. Jeng, *Macromol. Mater. Eng.* **2018**, *303*, 1700433.

[25] W. Wang, D. Shen, X. Li, Y. Yao, J. Lin, A. Wang, J. Yu, Z. L. Wang, S. W. Hong, Z. Lin, S. Lin, *Angew. Chem. Int. Ed.* **2018**, *130*, 2139-2143.

[26] F. Ge, R. Yang, X. Tong, F. Camerel, Y. Zhao, *Angew. Chem. Int. Ed.* **2018**, *57*, 11758-11763.

[27] R. Ranjan, S. D. Narnaware, N. V. Patil, *Nati. Acad. Sci. Lett.* **2018**, *41*, 403-406.

[28] I. K. Shishmanova, C. W. Bastiaansen, A. P. Schenning, D. J. Broer, *Chem. Commun.* **2012**, *48*, 4555-4557.

[29] L. T. de Haan, J. M. Verjans, D. J. Broer, C. W. Bastiaansen, A. P. Schenning, *J. Am. Chem. Soc.* **2014**, *136,* 10585-10588.

[30] Y. Wang, A. H. McKinstry, K. A. Burke, *Biomacromolecules*, **2020**, *21*, 2365-2375.

[31] R. S. Kularatne, H. Kim, M. Ammanamanchi, H. N. Hayenga, T. H. Ware, *Chem. Mater.* **2016**, *28*, 8489-8492.

[32] J. E. Stumpel, E. R. Gil, A. B. Spoelstra, C. W. Bastiaansen, D. J. Broer, A. P. Schenning, *Adv. Funct. Mater.* **2015**, *25*, 3314-3320.

[33] Y. Chen, L. Yin, F. Ge, X. Tong, H. Zhang, Y. Zhao, *Macromol. Rapid Commun.* **2021**, 100495.

[34] T. L. Malkin, B. J. Murray, A. V. Brukhno, J. Anwar, C. G. Salzmann, *Proc. Natl. Acad. Sci. U.S.A.* **2012**, *109*, 1041-1045.

[35] M. J. Ford, C. P. Ambulo, T. A. Kent, E. J. Markvicka, C. Pan, J. Malen, C. Majidi, *Proc. Natl. Acad. Sci.* **2019,** *116*, 21438-21444.

[36] A. Kotikian, J. M. Morales, A. Lu, J. Mueller, Z. S. Davidson, J. W. Boley, J. A. Lewis, *Adv. Mater.* **2021**, *33*, 2101814.

[37] R. A. Gemeinhart, Park, H., Park, K., *Polym. Adv. Technol.* **2000**, *11*, 617-625.

[38] A. K. Tiwari, J. P. Goss, P. R. Briddon, N. G. Wright, A. B. Horsfall, R. Jones, H. Pinto, M. J. Rayson, *Phys. Rev. B* **2011**, *84*, 245305.

CHAPTER 3. LIQUID CRYSTALLINE ELASTOMER FOR SEPARATE OR COLLECTIVE SENSING AND ACTUATION FUNCTIONS

3.1 About the project

The development of flexible, deformable sensors for soft electronics has attracted a great deal of interest due to their promising applications in displays, electronic skins, implantable medical devices, and energy generators. A requirement for these sensors is to exhibit change of an electrical property (conductivity, resistance, capacity) upon deformation and can sustain at large deformations without breakage. For this reason, elastomers have been a natural choice of materials in the field of deformable electronics. In the previous chapter, we found that a porous LCE actuator filled with an ionic liquid (PLCE-IL) displays change in electrical resistance in response to deformation. Therefore, we carried out a follow-up study focused on PLCE-IL, aiming to reveal its potential to fulfill the functions that are normally obtained from two classes of materials: sensing using electrically responsive, deformable materials and stimuli-triggered actuation using soft active materials. Interesting findings are reported in this chapter. On one hand, upon the order–disorder phase transition of aligned mesogens, PLCE-IL behaves like a typical actuator capable of stimuli-triggered reversible shape change and movement. On the other hand, at temperatures below the phase transition, PLCE-IL is an elastomer that can sustain and sense large deformations of various modes as well as environmental condition changes (temperature, humidity) by reporting the corresponding electrical resistance variation. Moreover, the collective use of two distinguished functions has been demonstrated in one device, that is, PLCE-IL is a component that works as sensor but can switch its role to actuator when required.

3.2 Contributions

This work was published in *Small*, **2023**, 2301932 by Jie Jiang and Yue Zhao. The research work was conducted in Université de Sherbrooke under the supervision of Prof. Yue Zhao. I designed the experiments and was responsible for the entire process from preparing and characterizing PLCE-IL samples, assembling the PLCE-IL-based sensing devices, collecting data of the PLCE-IL devices about sensing and actuation functions, and analyzing the use of LCEs as a deformable device and as a soft robot. I processed all data and produced all the Figures and Schemes. I wrote the first draft of the manuscript and Prof. Yue Zhao modified, revised, and finalized the manuscript.

3.3 Paper Published in *Small*, 2023, 2301932.

Liquid crystalline elastomer for separate or collective sensing and actuation functions

Jie Jiang, Yue Zhao*

Département de Chimie, Université de Sherbrooke, Sherbrooke, Québec, J1K 2R1, Canada

*E-mail: yue.zhao@usherbrooke.ca

3.3.1 Abstract

A porous liquid crystalline elastomer actuator filled with an ionic liquid (PLCE-IL) is shown to fulfill the functions of two classes of materials: electrically responsive, deformable materials for sensing and soft active materials for stimuli-triggered actuation. On one hand, upon the order-disorder phase transition of aligned mesogens, PLCE-IL behaves like a typical actuator capable of reversible shape change and can be used to assemble light-fueled soft robot. On the other hand, at temperatures below the phase transition, PLCE-IL is an elastomer that can sustain and sense large deformations of various modes (stretching, twisting, bending, vibration) as well as environmental condition changes (temperature, humidity) by reporting the corresponding electrical resistance variation. The two distinguished functions can also be used collectively with PLCE-IL integrated in one device. This intelligent feature is demonstrated with an artificial weight-lifting arm. When the arm is manually powered to fold and unfold, the PLCE-IL strip serves as a deformation sensor; while when the manual power is not available, the role of the PLCE-IL strip is switched to an actuator that enables light-driven folding and unfolding of the arm. This study shows that electrically responsive LCEs are an exciting materials platform that offers possibilities for merging deformable electronic and actuation applications.

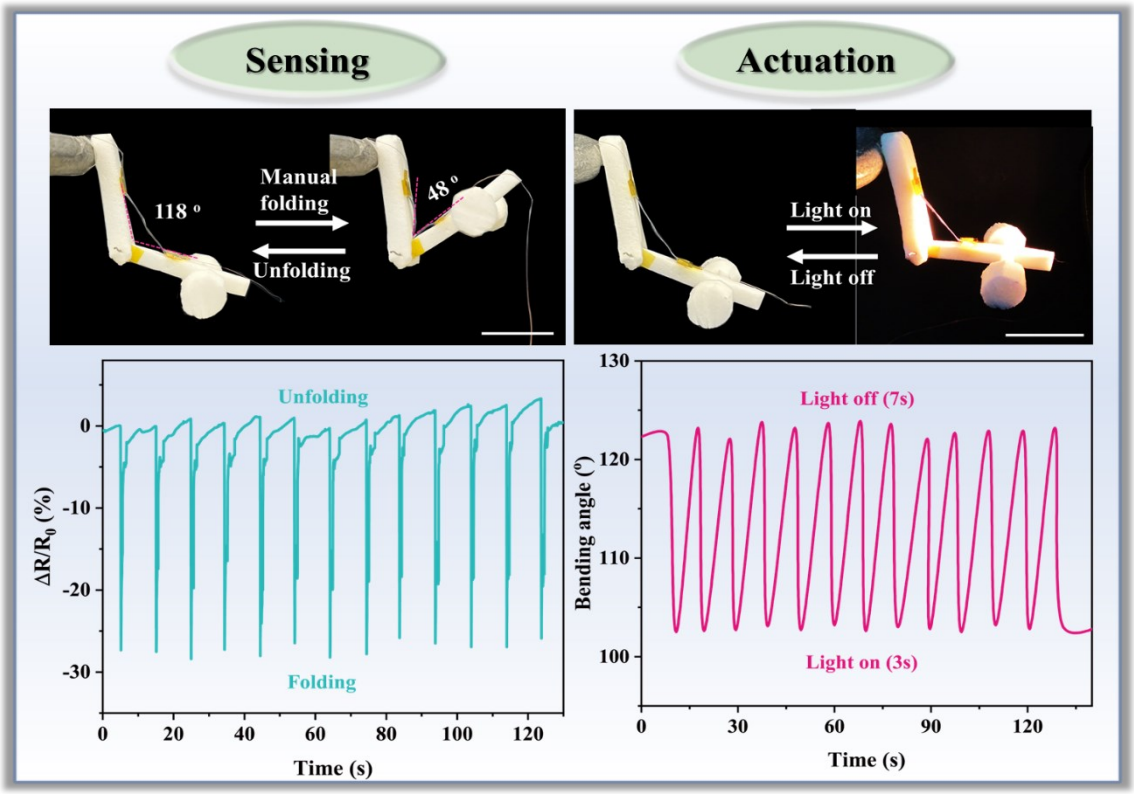
Sensing
Actuation
118 °
Manual folding
48 °
Unfolding
Light on
Light off
Unfolding
Folding
ΔR/R0 (%)
Time (s)
Light off (7s)
Light on (3s)
Bending angle (°)
Time (s)

3.3.2 Introduction

Currently there is great interest in developing advanced materials for deformable electronics given the wide range of applications in displays, electronic skins, implantable medical devices, and energy generators[1].The sought-after materials can be deformed (sometimes substantially) while retaining their desired electrical properties, such as electronic or ionic conductivity, and resistance or capacitance change. Understandably, the key issue and persistent challenge is to retain these electrical properties upon deformation, especially at large deformations. For conducting or electrically responsive materials capable of large deformations, elastomers are a natural choice and have been much studied.[2] On another front, liquid crystal elastomers (LCEs) have been increasingly explored as actuating materials for broad applications including biomimetic actuators, soft robots and artificial muscles.[3] When appropriately processed, LCE has the fascinating ability to undergo a large and reversible deformation (shape change or morphing) upon an order-disorder phase transition of mesogens in the polymer structure, which can be triggered by a variety of stimuli such as heat,[4] light,[5] electric field,[6] and humidity.[7] Therefore, it is of great interest to merge the characteristic properties and functions of both elastomers for deformable electronics and LCEs for actuation into one single material. To date, various electrically conductive LCE-based actuators have been developed by either embedding conductive wires[6a, 6b, 8] or introducing liquid metals[6c, 9] where electrical power is mainly used to trigger the order-disorder phase transition in the LCE actuators through the Joule heating effect. In the case of liquid metal-loaded LCEs, electrical conductivity change associated with the actuator's reversible deformation and motion has been demonstrated for sensing. However, studies from the perspective of endowing the actuating function with deformable electronic materials are rare. By mixing an ionic liquid in an LCE,[10] it was reported that stretching-induced alignment of mesogens can create ordered channels that facilitates the motion of ions, which results in large relative electrical resistance change upon deformation and thus

enhanced deformation sensing for wearable electronics,[11] but no actuation of the material was demonstrated.

Herein, we demonstrate an electrically responsive LCE that can fulfill separately two distinct functions. On one hand, it can sense mechanical motions/deformations as well as variations in environmental conditions through resistance changes. On the other hand, it is capable of order-disorder phase transition-based reversible shape change and stimuli-driven locomotion such as light-fueled movement. Before reporting our study, the interest of having the two separate functions as a trait of intelligence need to be emphasized with examples. Conceptually, the same material can function as sensor for human motions related to variable deformations (stretching, shearing, torsion, etc.) and, at due time or when desired, can be activated to work as an artificial muscle to do mechanical work. It is also conceivable that a soft robot senses the environment of an initial location, and then is driven by a stimulus (e.g. light) to move to a new place to sense a different environment.

3.3.3 Results and Discussion

3.3.3.1 Fabrication and Characterization of PLCE-IL

The approach and materials used in the present study are shown in Figure 1a. We first prepared a porous liquid crystalline elastomer (PLCE) with interconnected void channels and uniaxially aligned mesogens. In short, a molded film of the used main-chain LCE mixed with $CaCO_3$ nanoparticles (adjustable content and size) was stretched to 330% strain for alignment of mesogens, exposed to UV light for photocrosslinking, and subjected to etching in an acid solution for nanoparticles removal.[12] Then, the PLCE film was filled with an IL, 1-butyl-3-methylimidazolium tetrafluoroborate ($BMIMBF_4$), through soaking in an IL/water solution followed by drying. The resulting material, denoted as PLCE-IL, can fulfil the conditions required for the two separate functions: on the one hand, it is still elastic and can sustain large deformation, while electrical resistance variation enables sensing; on the other hand, it still can behave like an LCE actuator to exhibit reversible shape

change upon stimuli- triggered order-disorder phase transition of the mesogens. The effect of loaded IL on the alignment of mesogens and the mechanical property of the material was first investigated.

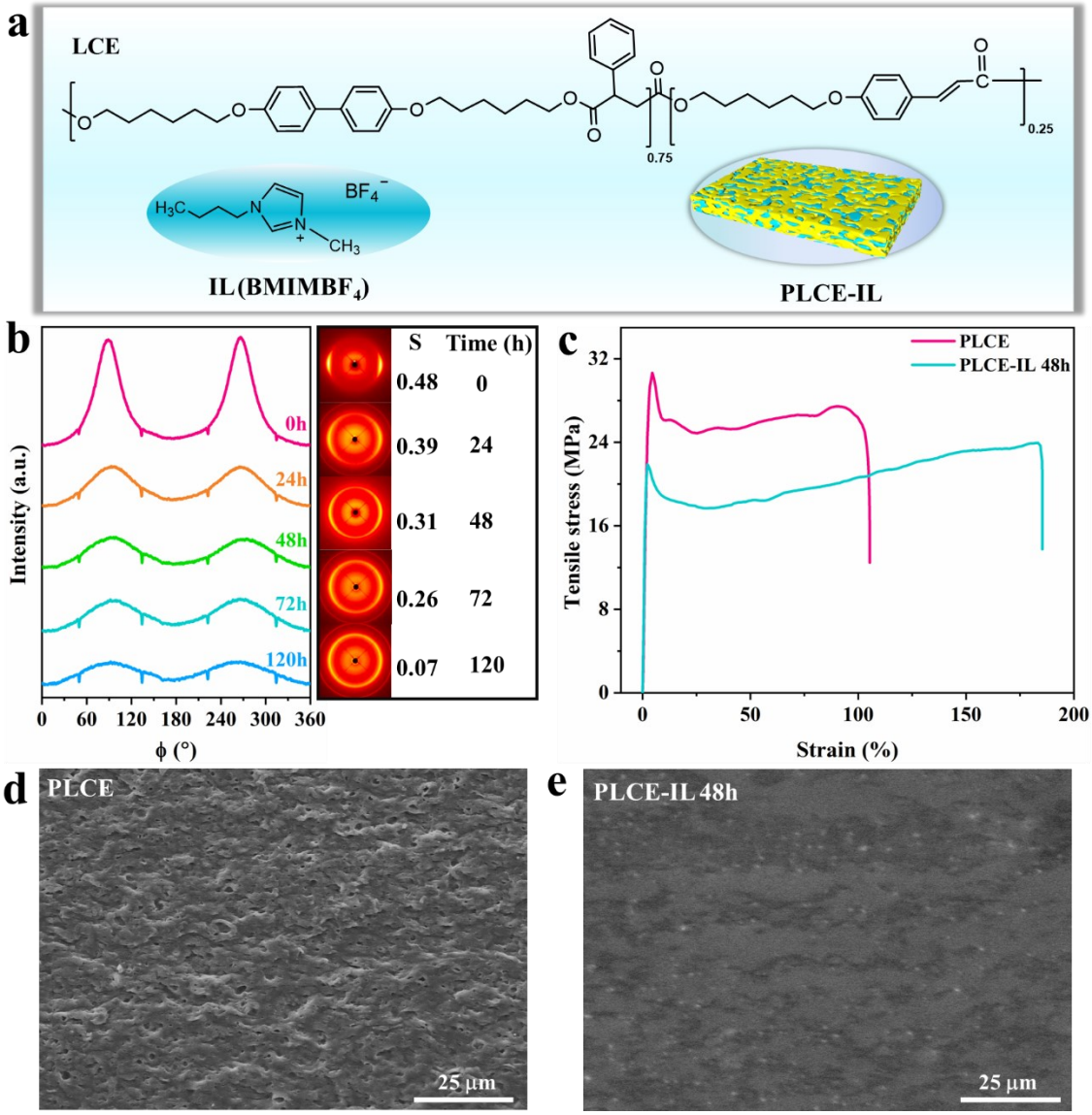

Figure 1. (a) Chemical structures of the liquid crystalline elastomer (LCE) and ionic liquid (IL, $BMIMBF_4$), and schematic illustration of porous LCE filled by ionic liquid (PLCE-IL). (b) 2D-WAXS patterns, azimuthal diffraction profiles (2θ=17.6˚-20.9˚ for nematic order), and order parameters for an PLCE film soaking in an IL/DI (3/1) mixture for different

times, followed by drying. (c) Tensile stress-strain curves at room temperature of PLCE and PLCE-IL (48h soaking). (d) SEM images of PLCE (on the left) and PLCE-IL (right).

Different soaking times in IL/DI (3/1, v/v) were used in preparing the PLCE-IL films. The swelling of PLCE increases over time, though slightly after 24 h, resulting in an increased loading of IL (Figure S1, Supporting Information). For the resulting PLCE-IL films, Figure 1b shows their 2D-WASX patterns, azimuthal diffraction profiles (at 2θ=17.6˚-20.9˚) and calculated order parameters (S) for the uniaxial alignment of mesogens. It is seen that the order parameter decreases with increasing the soaking time, meaning that the filled IL has a disrupting effect on the alignment of mesogens. Therefore, a good trade-off between filled IL and retained alignment of mesogens is necessary for achieving both sensitive electrical resistance change (for sensing) and large reversible shape change (for actuation). Unless otherwise stated, the soaking time of 48 h was used in preparing PLCE-IL. Under this condition, the content of filled IL is about 28 wt%, as estimated from the weight loss and degradation steps using TGA measurement (Figure S2, Supporting Information). The presence of IL also affects the mechanical properties of the material, as can be seen from the tensile tests at room temperature in Figure 1c. While the Young's modulus appears unchanged, the yield stress of PLCE-IL decreases by about 29% as compared to PLCE (22 MPa for the former and 31 MPa for the latter). However, the PLCE-IL film can be elongated to larger strain at the break (185%) than PLCE (105%), corresponding to an improved toughness. These results indicate that IL filled in PLCE has a softening effect on the material. Figure 1d compares the SEM images of PLCE and PLCE-IL. The pores in PLCE are no longer visible. More characterization results are reported in Figure S3. The average pore size of PLCE is about 400 nm, based on SEM images (Figure S3, Supporting Information). The presence of IL after the filling process is confirmed by both energy-dispersive spectroscopy (SEM-EDS) and attenuated total reflection-Fourier transform infrared (ATR-FTIR) (Figure S3, Supporting Information). Moreover, comparing the DSC heating and cooling curves of PLCE-IL with PLCE (Figure S3, Supporting Information), even with a

large amount of IL, the glass transition temperature (T_g) and the nematic-isotropic (order-disorder) phase transition temperature show almost no changes, appearing at ≈ 24 ºC and ≈ 58 ºC, respectively.

3.3.3.2 PLCE-IL as Deformable Sensing

The electrically responsive sensing capability of PLCE-IL was first investigated by measuring the relative resistance change defined as $\Delta R/R_0$, where R_0 is the initial resistance. Depicted in Figure 2a are an illustration and a photo of a PLCE film in contact with two copper electrodes sandwiched by two pieces of transparent tapes, as well as the schematics showing the different deformation modes imposed on the PLCE-IL film. Figure 2b shows the relative resistance variation of the film subjected to stepwise strain upon uniaxial stretching at room temperature. It is seen that $\Delta R/R_0$ increases with increasing the strain. At a given strain, the variation reaches a peak value before dropping to essentially a plateau with the film under strain. This phenomenon, more prominent at higher strains, reflects a dynamic process of the changing ionic conductivity of the PLCE-IL. It is likely that the film stretching deforms the porous channels and disrupts the paths of ions, which results in the early resistance rise; whereas with the film under strain, possible structural relaxation occurs with concomitant rearrangement of ions, which recovers part of lost conductivity. The inset of Figure 2b plots the maximum $\Delta R/R_0$ (peak value) as a function of strain. Two regions are visible with strain below and above 60% respectively. The slope of the fitted straight line in each region, defined as the gauge factor (GF), is a measure of the sensing sensitivity for stretching deformation of PLCE-IL. As can be noted, the sensitivity is much greater in the higher strain range (about 60-150%). Plotting the value of $\Delta R/R_0$ (after peak) against strain also shows two regions with smaller GF values (Figure S4, Supporting Information). Moreover, since PLCE-IL is elastic material at $T<T_{ni}$, instead of the stepwise stretching, the film can also be stretched to a given strain and relaxed immediately upon removal of the external force. The PLCE-IL film was subjected to cyclic strain/relaxation

experiments at 45 ^{o}C, the relative resistance of the film rises and drops, and the peak value of $\Delta R/R_0$ changes linearly with strain (Figure S4, Supporting Information). The response times were measured at 30% strain. The duration of $\Delta R/R_0$ increase and decrease depends on how quickly the film responds to the loading strain and unloading, which is about 0.6 s (response) and 0.5 s (relaxation), indicating faster recovery upon release (Figure S4, Supporting Information). These results show that PLCE-IL has high strain sensitivity.

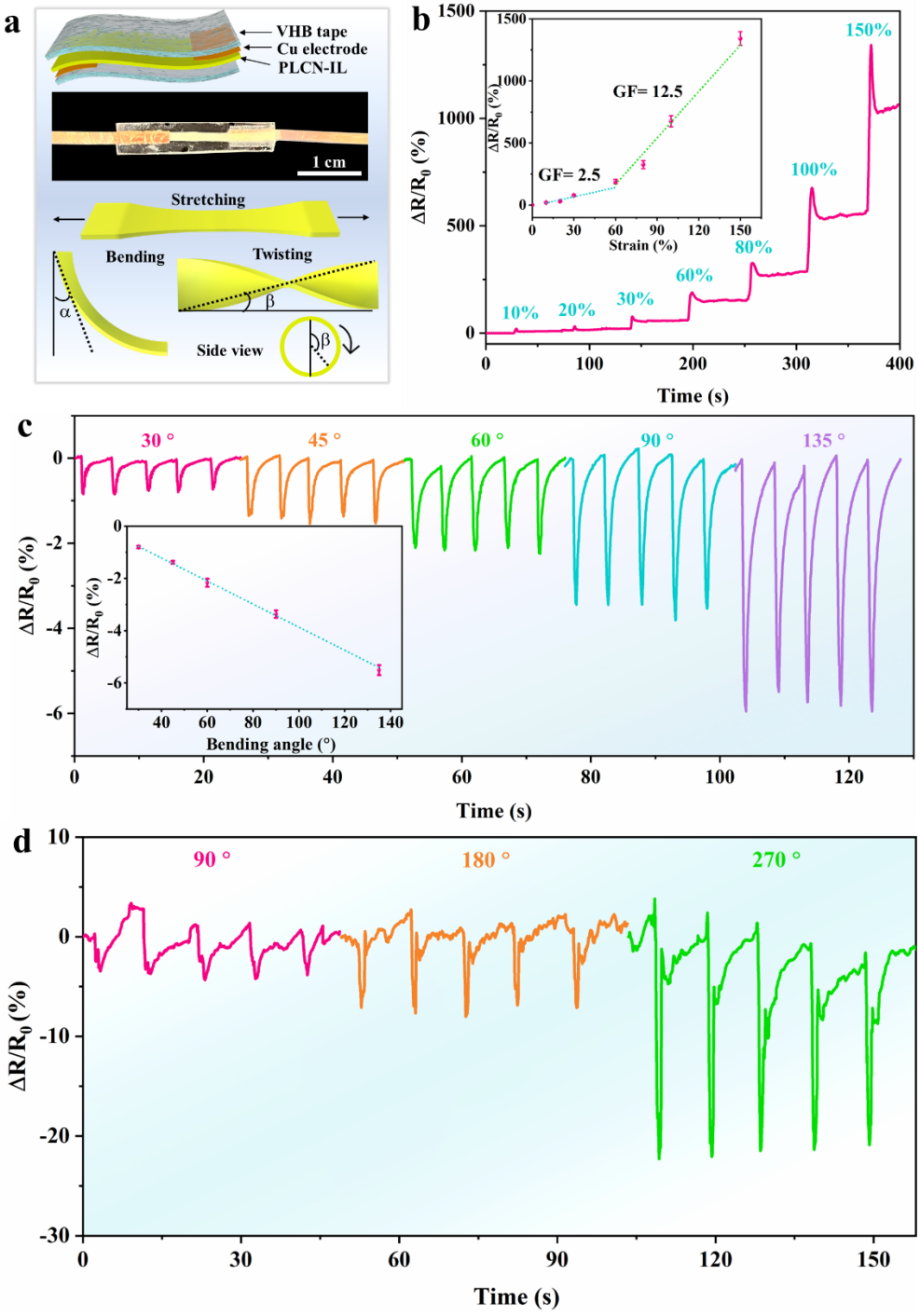

Figure 2. (a) Top: schematic and photo showing the sandwich structure of an electrically responsive, deformable sensing device assembled with VHB tap as sealing material, Cu as electrode, and PLCE-IL as conductive layer (size of PLCE-IL: 1.5 cm × 2 mm × 80 μm).

Bottom: schematics showing the deformation modes and how to define the bending angle (α) and the twisting angle (β) (the twisting angle is determined clockwise along the circle. (b) The relative resistance variation of PLCE-IL sensor in response to stepwise uniaxial strain ranging from 10 to 150% at room temperature. The inset is the plot of peak value of relative resistance change vs. strain, with the linear fitting used to measure the gauge factor (GF)). (c) Relative resistance changes of PLCE-IL sensor for bending from 30° to 135° (inset fitted curve showing relative resistance change vs. bending angle). (d) Relative resistance change vs. twisting angle (90°, 180°, 270°) of PLCE-IL deformable sensor.

In addition to stretching, deformable devices require sensors to sustain other large mechanical deformations, such as bending, twisting, and vibration. Figure 2c shows the cyclic relative resistance changes of a PLEC-IL film subjected to bending for bending angles of 30-135°. For these tests, one end of the film was fixed and the other one was free to fold. As can be seen, the relative resistance decreases upon bending, and the effect is more prominent with increasing the bending angle. The good linear relationship between $\Delta R/R_0$ and bending angle (inset of Figure 2c) shows that the PLCE-IL based device can be used to detect and recognize different bending angles. Furthermore, by replacing the simple PLCE-IL film with a PLCE-IL/LCE bilayer in the assembly shown in Figure 2a, the bending direction can also be revealed from the relative resistance change. Indeed, when the active bilayer is bent towards the non-conductive LCE side with a bending angle 90°, the relative resistance increases, and conversely, when it is bent towards the conductive PLCE-IL side, the relative resistance decreases **(**Figure S5, Supporting Information). This behavior can be explained as follows. Upon bending towards to the LCE side, the length of the conductive PLCE-IL film is elongated, which leads to a significant increase in the resistance as a result of longer conductive pathway and lower local ion concentration due to deformation. The opposite effect acts upon bending towards the PLCE-IL side, as the conductive side is squeezed to generate shorter conductive pathway and higher local ion concentration, giving rise to a decrease in relative resistance[13]. Serving as another example, twisting

deformation was imposed on the device containing a single PLCE-IL layer, under different twisting angles (90°, 180°, 270°). As shown in Figure 2d, the relative resistance decreases with increasing the twisting angle. Finally, the PLCE-IL based device can also be used to detect damped vibration, a special motion mode **(**Figure S6, Supporting Information). The whole of the above results shows that the elastic, ionic conductive PLCE-IL actuator can fulfil the functions of deformable materials for sensing diverse mechanical deformations, making them potentially useful for deformable smart devices to monitor various real-time motions.

3.3.3.3 PLCE-IL as Stimulus-Driven Actuator

As pointed out above, the purpose of this work is to demonstrate the use of electrically conductive LCEs as a platform for materials that can serve separately or collectively for sensing and actuation. Indeed, PLCE-IL remains an actuator that exhibits reversible shape change or stimuli-controlled movement through order-disorder phase transition**.** Figure 3 shows a PLCE-IL based soft robot designed to realize light-fueled locomotion. It was fabricated with a top transparent bridge on BOPP (commercial transparent scotch-tape, thickness: 45 μm), an ink-painted PLCE-IL strip (the same one as used in the sensing device), and two legs made of card stock. The robot could crawl on the surface of a paper under intermittent light exposure, as a result of the cyclic contraction/extension of the PLCE-IL strip at light on and off state, respectively, and a friction bias of the two legs (Figure 3a). Under a light intensity of 3 W cm^{-2}, the photothermally induced nematic-isotropic phase transition is fast (Figure S7, Supporting Information). As shown by the photos in Figure 3b and Movie S1 (Supporting Information), when the robot crawling under light on/off cycles (light on for 2 seconds and light off for 9 seconds) is realized at room temperature (21 °C), it moves at an overall speed of 7.0 mm min^{-1}. By carrying out the tests at 38 °C, the robot in the hotter environment moves at a reduced speed of 5.6 mm min^{-1}. Figure 3c shows the corresponding electrical signaling from the robot crawling at the two different

environmental temperatures. In both cases, the relative resistance drops when light is on, and it goes up when light is off. Although the change in length and the order/disorder state of mesogens in PLCE-IL may contribute to change in resistance, the drop in $\Delta R/R_0$ is mainly caused by the light-induced heating of the material, which results in higher conductivity of ions with increased temperature. As light is turned off, the PLCE-IL strip is cooled and the resistance increases. The effect is similar to direct heating and cooling of PCLE-IL across the nematic-isotropic phase transition (Figure S8, Supporting Information). A couple of interesting observations can be made from Figure 3. First, with respect to the resistance at 21 ºC, $\Delta R/R_0$ of the robot in the stationary state (prior to light exposure) already decreases at 38 ºC, showing that the PLCE-IL based robot can sense the temperature change in the environment. Second, the oscillation amplitude of $\Delta R/R_0$ between light-on and light-off state is smaller at 38 ºC than at 21 ºC. At both environment temperatures, when light on/off cycles are applied, the recorded resistance variation mainly reflects the difference between the temperature at light-on (2 s duration) and the temperature at light-off (after 9 s cooling) of the PLCE-IL component in the robot. Since the temperature reached at light-on is similar, the cooling of the sample in a cooler environment (21 ºC) is faster, which results in a larger temperature difference and, consequently, a greater resistance variation. In both cases, however, the cooling time of 9 s is not sufficiently long to bring the sampler back to the environment temperature, which explains the partial recovery of the resistance at light-off with respect to the initial resistance at given environment temperature, which explains the partial recovery of the resistance at light-off with respect to the initial resistance at a given environment temperature. More interestingly, since the temperature difference between light-on and light-off determines the magnitude of the reversible shape change that, in turn, dictates the locomotion behavior, the lower moving speed of the robot at 38 ºC is understandable. In other words, not only the PLCE-IL senses the environmental temperature change, its feedback on relative resistance change during the light-driven movement of the robot can also provide information about the magnitude of the reversible

shape change that is directly related to the speed of locomotion. Therefore, this example demonstrates the correlation between the actuation and sensing functions, which enables PLCE-IL based soft robot to perceive and interact with changing environments, and report its operation conditions through feedback signals. In addition to temperature, PLCE-IL can also sense the humidity change in the range of 43-98% at room temperature with a decrease of relative resistance when humidity increases (Figure S9, Supporting Information). This result is no surprise, because absorbed water molecules could decrease the viscosity of the IL and thus increase the ionic conductivity.[14].

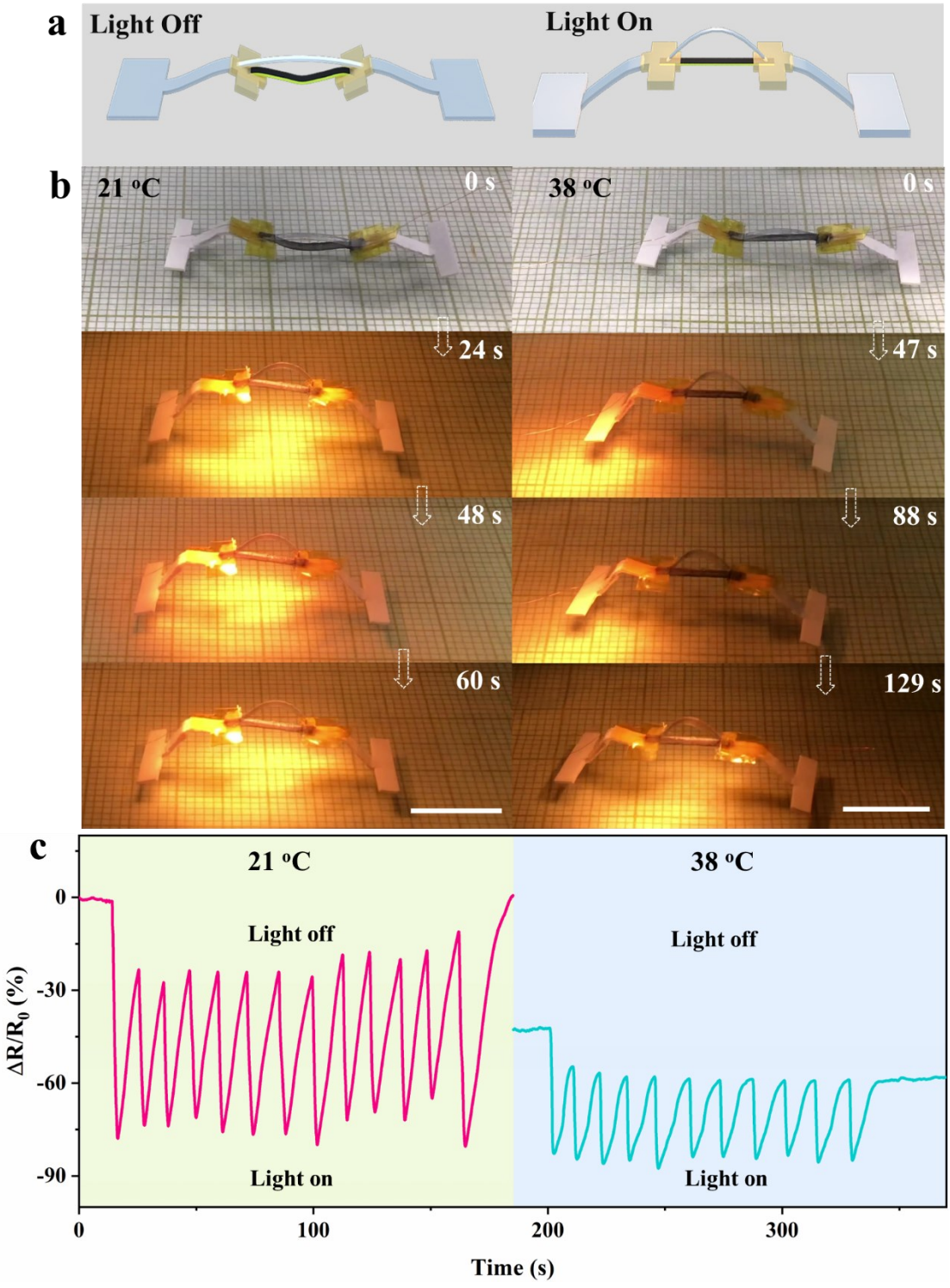

Figure 3. (a) Schematics illustration of a PLCE-IL based walker crawling on the surface through cyclic contraction and outward bending under light on/off cycles. (b) Photos

showing the light-fueled crawling of the walker at two different environmental temperatures: 21 (left) and 38 ºC (right). (Size: 1 cm × 2 mm × 80 μm, light intensity: 3 W/cm^2, light on 2s/ light off 9s, scale: 1 cm). (c) The corresponding relative resistance changes of the walker crawling under light on/off cycles.

3.3.3.4 PLCE-IL for Collective Sensing and Actuation

After demonstrating separately the sensing and actuation capabilities of PLCE-IL, it would be more challenging to envision applications where the same material functions as both sensor and actuator depending on the necessity. To this end, Figure 4 shows a PLCE-IL based weight-lifting artificial arm designed to mimic a bicep muscle, in which an ink-paint PLCE-IL strip was tethered to the foam board arm serving as the skeleton to realize elbow movements. On the one hand, when the artificial arm moves, the PLCE-IL strip acts as a sensor. For example, when the arm was manually made to repeatedly bend to a 48º angle and then unbend to the initial posture at room temperature (Figure 4a), cyclic variation of the relative resistance due to the bending deformation could be recorded (Figure 4b). In this action, the PLCE-IL strip acts just as a sensor for monitoring the movement of the artificial arm. On the other hand, since the PLCE-IL strip is also an actuator, when the situation requires, it enables light-controlled bending and unbending of the artificial arm. When the PLCE-IL strip was irradiated with light, it contracted, causing the arm to bend and lift a weight of 26 mg (about 11 times heavier than its own weight); whereas, when light was turned off, the PLCE-IL strip extended, unbending the arm (Figure 4c, Movie S2, Supporting Information). The light-controlled muscle-mimicking movement can be repeated for many cycles with the corresponding relative resistance changes measured (Figure 4d). In addition, the amplitude of relative resistance changes between light-on and light-off state is different upon different light-on/off time, and longer light-off intervals cause a larger amplitude in relative resistance change of PLCE-IL strip (Figure S10, Supporting Information). This is because a longer cooling time will give the PLCE-IL strip enough

time to extend to the original state, and further improve its reversible actuation degree. Regarding the actuation, furthermore, PLCE-IL strip actuator can be used to realize reversible light-controlled lifting and lowering of an object that is 1250 times heavier, with the height of lift corresponding to a reversible actuation degree of about 62 % (Figure S11, Supporting Information).

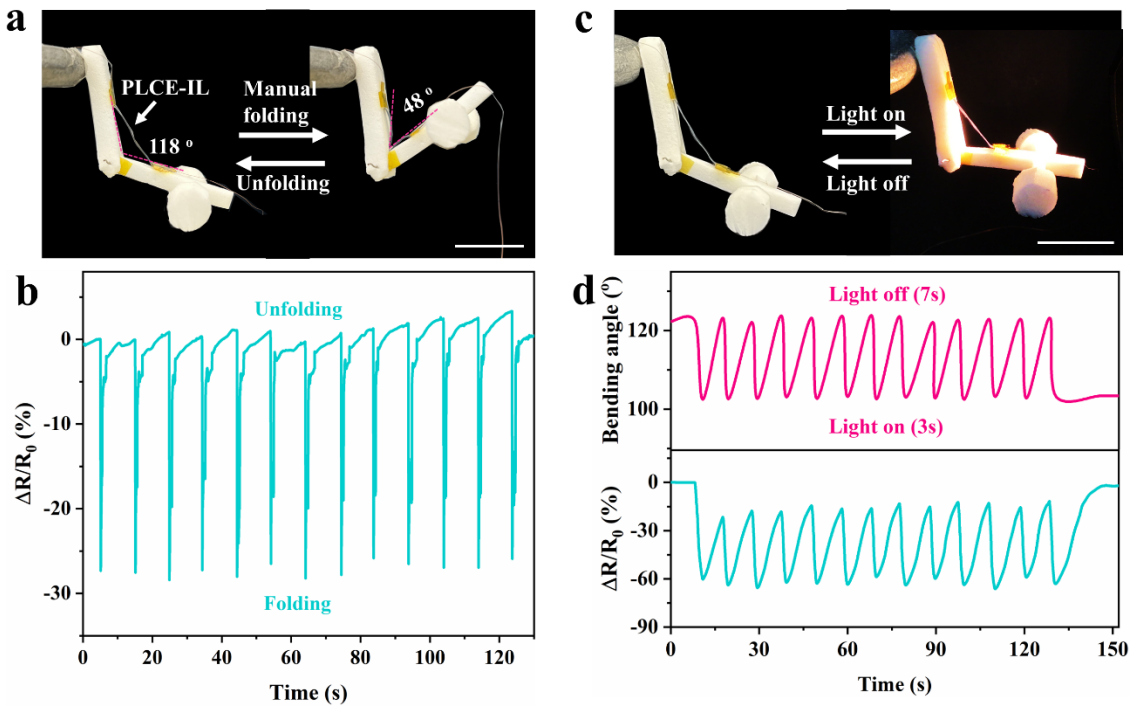

Figure 4. An artificial arm comprising a PLCE-IL strip that can function either as sensor or actuator (weight of the PLCE-IL strip: 2.3 mg, and weight of the dumbbell load: 25.6 mg,). (a) Photos showing manual elbow bending and unbending of the arm (scale bar: 1.5 cm), and (b) corresponding relative resistance changes. (c) Photos showing light-driven elbow movement of the arm activated by the PLCE-IL strip exposed to cycles of light-on (3 s) and light-off (7 s) (scale bar: 1.5 cm), and (d) corresponding elbow bending angle switch and relative resistance changes (light intensity: 3 W/cm^2).

Before concluding, a comment related to the actuation performance of PLCE-IL is worth being made. Any time when a non-actuating additive or element is added in a LCE actuator,

which are the pores and ionic liquid in PLCE-IL, with the purpose to endow the actuator with a new function or property, the actuation performance is most often, if not always, reduced to a certain degree. What is important is to achieve a good trade-off between the sought-after new function and the actuation performance depending on the targeted application. To this regard, it certainly is of great interest to find ways that allow LCE actuator to display new functions with little or without sacrificing the actuation performance.

3.3.4 Conclusion

We have demonstrated the use of LCEs as a deformable material platform for both sensing and actuation functions. This was achieved by preparing PLCE-IL, a porous LCE actuator with uniaxially aligned mesogens filled with an IL for electrical conductivity. On the one hand, at temperatures below T_{NI}, PLCE-IL is an elastomer that can sustain large deformations and sense the various deformation modes (stretching, bending, twisting and vibration) as well as changing environmental conditions (temperature, humidity) through change in its electrical resistance. On the other hand, by heating above and cooling below T_{NI}, PLCE-IL behaves like a typical LCE actuator, displaying reversible shape change as a result of the order-disorder phase transition of the mesogens. As an example of actuating properties, light-fueled crawling movement of a soft robot at two different surrounding temperatures was realized using PLCE-IL. Moreover, the two separate or distinguished functions of sensing and actuation can also be used collectively in one device. To demonstrate this feature, a PLCE-IL integrated artificial arm was fabricated. When the arm is manually powered to fold and unfold repeatedly, the PLCE-IL strip in the device senses the cyclic deformation by reporting the associated relative resistance change. In case the manual power is not available, and the arm still needs to function (e.g., for weight lifting), the role of the PLCE-IL strip can be switched to acting as an actuator, allowing the arm to fold and unfold under light on/off cycles. The principle of merging the sensing and

actuation functions into a single LCE has the potential to offer a new route to combining deformable electronics applications and active materials.

3.3.5 Experimental Section

Materials

4,4'-Dichloromethane (99%) was purchased from Fisher Scientific; p-coumaric acid (99%), 6-chlorohexanol (96%), phenylsuccinic acid (98%), $CaCO_3$ particles (size: ≈ 0.8 mm), and 1-butyl-3-methylimidazolium tetrafluoroborate **(**$BMIMBF_4$, ≥98%**)** was purchased from Sigma Aldrich. Scotch 4910 VHB tape (thickness: 1.02 mm) and BOPP tape (thickness: 45 mm) were purchased from 3-M Company. Copper magnet wire (diameter: 50 mm) with polyurethane as the insulation coating was purchased from Remington Industries. They were used directly without further purification.

Preparation of Porous LCE Actuator

The preparation of porous LCE actuator with uniaxially mesogens contains three steps. First, a compressed composite film (LCE/$CaCO_3$ (30 wt.%); thickness: 180 μm) was cut into 10 mm × 2 mm in length and width, respectively, and then was stretched with tweezers at 55 ºC in water to 40 mm × 1 mm × 80 μm, and with final strain at 330±10%. Secondly, the film was crosslinked by using UV Spot System via a filter with wavelength in the range of 320-480 nm for 2 h in each side. Finally, the crosslinked film was soaking in HCl (12M) for 48 h, and washing for 10 min by DI, and then drying in vacuum oven at 45 ºC for 6 h. The detailed fabrication was reported in previous literature.[12]

IL Filling Process

PLCE strip was immersed and swollen in an IL/DI water (3/1, v/v) solution for different times (0, 24, 48, 72, 120 h) at room temperature (denoted as PLCE, PLCE-IL 24 h, PLCE-IL 48 h, PLCE-IL 72 h, and PLCE-IL 120 h). Second, the PLCE-IL strips, after wiping out the extra IL on surface, were dried in vacuum oven at 45 ºC for 4 h.

Sensing Devices Assembling

For deformation-sensing, the PLCE-IL based electronic device was fabricated by sandwiching the PLCE-IL strip (1.5 cm × 2 mm × 80 μm) between two thick transparent VHB tape with the Cu wire electrodes on each side.

Measurement of Deformable Sensor

To conduct the stretching test, one end of device was fixed while the other end of device was clipped by tweezers as free end. The free end was stretched to a certain given stretching ratio and then the force was maintained. In the bending test, one end of device was vertically attached to a lab. iron stand and the other end was free. Then, the free end of device was manually bent to varying angles with a paper marked by angle as the background, and then released it. To perform the twisting test, the two ends of device were clamped by tweezers, and then the device was manually twisted.

Characterization

The surface and cross-sectional morphology as well as the measurements of EDX and EDS for PLCE and PLCE-IL subjected to different treatments were examined or recorded using a Hitachi S-4700 field-emission-gun SEM operating at 1-10 kV. 2D-XRD patterns were performed on a Bruker AXS Nanostar system with a microfocus copper anode, montal optics and a Vantec 2000 2D detector at 55 mm from the samples. The X-ray wavelength was 0.154 nm, and the azimuthal scans of 360º were measured at 2θ= 17-28º (for nematic order), and 2θ= 1-3º (for smectic layers). TGA (Setsys 24) was performed to measure the weight fraction of IL on a thermogravimetric analyzer from 25 ºC to 800 ºC at 10 ºC min^{-1} under N_2 atmosphere flow of 50 ml min^{-1}. Phase transition temperatures were determined by using a DSC (TA Q200) in the range of -20 to 120 ºC at a rate of 10 ºC min^{-1}, under protection of nitrogen flowing at 50 ml min^{-1}. The ATR-FTIR spectra were recorded on a Nicolet-IS10 (Thermo Electron Co.) spectrometer with resolution 4 cm^{-1}. The mechanical

properties and Young's modulus of samples were examined using an Instron5965 universal testing system at a strain rate of 5 mm min^{-1}. For light-triggered deformation, a lamp (Flash Torch) was used to irradiate the samples, and the light intensity was measured using a power meter (TURNER, gentec-co Company). For electric al resistance changes of samples were recorded using a Digit Multimeter DMM6500 6 1/2 (Tektronix, Inc.).

3.4 Supporting Information

Supporting Information is available from the Wiley Online Library or from the author.

3.5 Acknowledgements

Y. Z. acknowledges the financial support from the Natural Sciences and Engineering Research Council of Canada (NSERC), le Fonds de recherche du Québec: Nature et technologies (FRQNT), and the Centre québécois sur les matériaux fonctionnels. J. J. is grateful to China Scholarship Council (CSC) for providing her with a scholarship to study and live in Canada. Dr. Fortin is acknowledged for assisting the XRD measurements.

3.6 Conflict of Interests

The authors declare no conflict of interests.

3.7 Date Availability Statement

The data that support the findings of this study are available from the corresponding author upon reasonable request.

3.8 Keywords

deformable sensor, soft actuator, liquid crystalline elastomer, multifunctional devices

3.9 References

[1] a) J. Y. Oh, S. Kim, H. K. Baik, U. Jeong, *Adv. Mater.* **2016**, *28*, 4455-4461; b) M. Karolina Pierchala, F. B. Kadumudi, M. Mehrali, T. G. Zsurzsan, P. J. Kempen, M. P. Serdeczny, J. Spangenberg, T. L. Andresen, A. Dolatshahi-Pirouz, *ACS Nano* **2021**, *15*, 9531-9549; c) X. Q. Wang, K. H. Chan, Y. Cheng, T. Ding, T. Li, S. Achavananthadith, S. Ahmet, J. S. Ho, G. W. Ho, *Adv. Mater.* **2020**, *32*, e2000351; d) H. Tran, V. R. Feig, K. Liu, Y. Zheng, Z. Bao, *Macromolecules* **2019**, *52*, 3965-3974.

[2] J. S. Noh, *Polymers* **2016**, *8*, 123.

[3] a) T. J. White, D. J. Broer, *Nat. Mater.* **2015**, *14*, 1087-1098; b) M. Lahikainen, H. Zeng, A. Priimagi, *Nat. Commun.* **2018**, *9*, 4148; c) B. Zuo, M. Wang, B. P. Lin, H. Yang, *Nat. Commun.* **2019**, *10*, 4539; d) T. Ube, T. Ikeda, *Angew. Chem.* **2014**, *53*, 10290-10299.

[4] a) R. Yang, Y. Zhao, *Angew. Chem. Int. Ed.* **2017**, *56*, 14202-14206; b) G. Babakhanova, T. Turiv, Y. Guo, M. Hendrikx, Q. H. Wei, A. Schenning, D. J. Broer, O. D. Lavrentovich, *Nat. Commun.* **2018**, *9*, 456; c) V. Magdanz, G. Stoychev, L. Ionov, S. Sanchez, O. G. Schmidt, *Angew. Chem. Int. Ed.* **2014**, *53*, 2673-2677.

[5] a) S. Ma, X. Li, S. Huang, J. Hu, H. Yu, *Angew. Chem. Int. Ed.* **2019**, *131*, 2655-2659; b) Z. Wang, K. Li, Q. He, S. Cai, *Adv. Mater.* **2019**, *31*, e1806849; c) F. Ge, R. Yang, X. Tong, F. Camerel, Y. Zhao, *Angew. Chem. Int. Ed.* **2018**, *57*, 11758-11763; d) Z. Z. Nie, B. Zuo, M. Wang, S. Huang, X. M. Chen, Z. Y. Liu, H. Yang, *Nat. Commun.* **2021**, *12*, 2334; e) X. Yang, Y. Chen, X. Zhang, P. Xue, P. Lv, Y. Yang, L. Wang, W. Feng, *Nano Today* **2022**, *43,* 101419; f) Y. Yang, Z. Pei, Z. Li, Y. Wei, Y. Ji, *J. Am. Chem. Soc.* **2016**, *138*, 2118-212.

[6] a) Y. Y. Xiao, Z. C. Jiang, X. Tong, Y. Zhao, *Adv. Mater.* **2019**, *31*, e1903452; b) C. Wang, K. Sim, J. Chen, H. Kim, Z. Rao, Y. Li, W. Chen, J. Song, R. Verduzco, C. Yu,

Adv. Mater. **2018**, *30*, e1706695; c) A. Kotikian, J. M. Morales, A. Lu, J. Mueller, Z. S. Davidson, J. W. Boley, J. A. Lewis, *Adv. Mater.* **2021**, *33*, e2101814.

[7] a) Y. Liu, B. Xu, S. Sun, J. Wei, L. Wu, Y. Yu, *Adv. Mater.* **2017**, *29*, 1604792; b) R. Lan, Y. Gao, C. Shen, R. Huang, J. Bao, Z. Zhang, Q. Wang, L. Zhang, H. Yang, *Adv. Funct. Mater.* **2021**, *31*; c) O. M. Wani, R. Verpaalen, H. Zeng, A. Priimagi, A. Schenning, *Adv. Mater.* **2019**, *31*, e1805985.

[8] Q. Q. He, Z. J. Wang, Y. Wang, A. Minori, M. T. Tolley, S. Q. Cai, *Sci. Adv.* **2019**, *5*, eaax5746.

[9] a) P. Lv, X. Yang, H. K. Bisoyi, H. Zeng, X. Zhang, Y. Chen, P. Xue, S. Shi, A. Priimagi, L. Wang, W. Feng, Q. Li, *Mater. Horiz.* **2021**, *8*, 2475-2484; b) M. J. Ford, C. P. Ambulo, T. A. Kent, E. J. Markvicka, C. Pan, J. Malen, T. H. Ware, C. Majidi, *Proc. Nat. Acad. Sci.* **2019**, *116*, 21438-21444; c) W. Liao, Z. Yang, *Adv. Mater. Technol.* **2021**, *7*, 2101260.

[10] M. Yao, B. Wu, X. Feng, S. Sun, P. Wu, *Adv. Mater.* **2021**, *33*, 2103755.

[11] a) T. Li, Y. Wang, S. Li, X. Liu, J. Sun, *Adv. Mater.* **2020**, *32*, e2002706; b) S. Park, K. Parida, P. S. Lee, *Adv. Energy Mater.* **2017**, *7*, 1701369; c) H. Kim, K. R. Pyun, M. T. Lee, H. B. Lee, S. H. Ko, *Adv. Funct. Mater.* **2021**, *32*, 2110535; d) D. Chen, Q. Pei, *Chem. Rev.* **2017**, *117*, 11239-11268.

[12] J. Jiang, L. Han, F. Ge, Y. Xiao, R. Cheng, X. Tong, Y. Zhao, *Angew. Chem. Int. Ed.* **2021**, *61*, e202116689.

[13] X. Dong, X. Guo, Q. Liu, Y. Zhao, H. Qi, W. Zhai, *Adv. Funct. Mater.* **2022**, *32*, 2203610.9.

[14] a) A. Jarosik, S. R. Krajewski, A. Lewandowski, P. Radzimski, *J. Mol. Liq.* **2006**, *123*, 43-50; b) S. Xiang, X. He, F. Zheng, Q. Lu, *Chem. Eng. J.* **2022**, *439*, 135644.

CHAPTER 4. A POROUS MULTI-STIMULI RESPONSIVE LIQUID CRYSTAL ELASTOMER ACTUATOR ENABLED BY MOF LOADING: WATER UPTAKE, MAGNET-GUIDED NAVIGATION, AND LIGHT-DRIVEN LOCOMOTION

4.1 About the Project

In an effort to widen the scope of porous LCE actuator, we used nanocrystals of MIL-88A, an organic-metal framework (MOF), in the templating method. This material design allows us to investigate the concept of "active porogen", which means that the removable nanoparticles are not just for creation of pores, but have or enable other functions by their presence in LCE. Given that MOF is porous material in its own capacity, prior to removal by etching, LCE-MOF is nanoscale porous material. And the used MIL-88A is known to be deformable by absorption of water or ethanol, its addition in large quantity in a polymer may render the latter humidity sensitive. Our study, reported in this chapter, indeed revealed a number of interesting properties of LCE-MOF actuator. In particular, because the actuator with MOF (nanoporous) and after MOF removal (macroporous like in previous chapters) swell in water to different degrees and at different rates, spatially controlled etching in the thickness direction of the actuator leads to an unusual deformation behavior (bending reversal). We also made an unexpected finding. The actuator after MOF removal becomes magnetically responsive, being attributed to in-situ formation of magnetic Fe_3O_4 nanoparticles due to UV light irradiation and acid etching. As a result, the actuator can be driven and directed by a magnet to move on water surface. Concomitantly, the photothermal effect enhanced by light absorption and heat release of Fe_3O_4 can be exploited for efficient light-fueled locomotion.

4.2 Contributions

This manuscript is in preparation and will be submitted soon. The authors are Jie Jiang, Yaru Ma, Ruidong Cheng, and Yue Zhao. The research was conducted in Université de Sherbrooke under the supervision of Prof. Yue Zhao. In this work, my contributions include: designing and executing experiments, synthesizing MIL-88A nanoparticles, preparing LCE actuators, analyzing all experimental data and results. Some data of swelling in water were collected with the help of Yaru Ma. Ruidong Cheng helped me analyzing the XPS data. I wrote the first draft of the manuscript. Prof. Zhao revised and finalized the manuscript.

4.3 Manuscript in Preparation

A Porous Multi-stimuli Responsive Liquid Crystal Elastomer Actuator Enabled by MOF Loading: Water uptake, Magnet-Guided Navigation, and Light-Driven Locomotion

Jie Jiang, Yaru Ma, Ruidong Cheng, Yue Zhao*

Département de Chimie, Université de Sherbrooke, Sherbrooke, Québec, J1K 2R1, Canada.

*E-mail: yue.zhao@usherbrooke.ca

4.3.1 Abstract

A porous actuator is prepared using a liquid crystal elastomer (LCE) loaded with active metal-organic framework (MOF) nanoparticles (MIL-88A). While the swellable MOF additive endows the LCE actuator with nanoscale pores, after its removal by chemical etching, macroporous LCE actuator is obtained. This LCE-MOF actuator displays several interesting actuation features. 1) Selective etching allows the actuator to deform in usual manners in water owing to different water absorption of the nano- and macroporous layers. 2) The stretching-induced alignment of mesogens in the actuator is little affected by the presence of MOF and also substantially retained after water uptake, so that an actuation deformation can be generated either by water absorption or thermally induced order-disorder phase transition or combination of the two mechanisms. 3) Assisted by the UV irradiation used for polymer crosslinking in preparing the actuator, magnetic nanoparticles of Fe_3O_4 appear to be formed after chemical etching, which allows the actuator to gain the ability to move on water surface and track the multi-directional motions of a magnet. 4) The in-situ formation of magnetic nanoparticles in the macroporous actuator also provides an enhanced photothermal effect, making more effective light-driven locomotion of the actuator.

4.3.2 Introduction

Unless stated otherwise, in nature systems ranging from plants to human beings, many examples of stimuli-triggered shape change or deformation can be found with high complexity, efficiency and multifunctionality.[1] These natural systems have the ability to change their shape in response to various environmental stimuli, such as temperature, pH, light and electric filed.[2] To mimic such shape changing systems, the development of smart materials or stimuli responsive materials (SRMs) represents an exciting and rapidly growing area of materials science that has gained tremendous interest because of their potential applications for actuator, sensors, energy storage and biomedical engineering.[3] Particularly, the well-known anisotropic liquid crystal elastomers (LCEs), which combine the characteristics of ordered liquid crystal molecules and the entropy elasticity of polymer networks, stand out from others owing to advantageous actuation performance including reversible deformation, large amplitude, and rapid response.[4] LCEs-based actuators can exhibit complex macroscopic deformation, biomimetic locomotion, and intelligent functions under various stimuli.[5] To execute complex tasks, various rational designs on chemical compositions and assembling structures of LCEs have been investigated. For synthetic systems developed so far, new actuation functions and applications can be achieved by introducing dynamic bonds for crosslinking, especially with Diels-Alder dynamic network,[6] and introducing fluorophores for tunable photoluminescence,[7] or chromophores for reversible color-changing.[8] In addition, to amplify the actuation performance, diverse structures of actuator were designed, such as twisted fiber and spring actuator with ultrafast motion speed and multi-terrain locomotion,[9] springtail-inspired structure for jumping soft robot,[10] and Möbius strip as actuator with continuous rotation.[11] Therefore, it is easy to notice that most innovations in the field of LCE actuators reside in either designing new polymer structures or developing new actuator structures or both.

In recent years, a different approach has been emerging, which consists in introducing nano- or micropores into a LCE matrix without changing its chemical structure. The presence of pores offers new possibilities for the development in this filed. On one hand, nanopores can be obtained in LCEs through ingenious use of the mesogens in LCEs. The most notable example is the use of LCEs with a smectic phase, in which the mesogens are hydrogen-bonded benzoic acid dimers. Nanoporous materials can be prepared upon breaking of hydrogen bridges under heat or alkaline conditions.[12] Thanks to the nanoporous with 2D geometry, the resulting polymer membrane has potential for various applications such as patterning silver nanoparticles,[13] serving as absorbent materials,[12a] and as membrane with dynamic polarity-switching.[14] On the other hand, using directing template method is a simple and an efficient way to create pore structure in polymer matrix. Normally, the inorganic templates including SiO_2,[15] NaCl,[16] and $CaCO_3$[17] are easily removed by chemical etching and thus leaving pore cavity in the liquid crystal polymer (LCP) matrix. Using $CaCO_3$, we have demonstrated the use of the template method to prepare porous LCE actuators.[17] One example shows the porous liquid crystalline network can be enabled loading/removal/reloading of different functional fillers due to the hydrogel-like behavior, imparting its actuator with reconfigurable functions. In particular, a deformable and electrically responsive porous LCE filled with by an ionic liquid (PLCE-IL) is fabricated, exhibiting multiple functions via integration of sensing and actuating function.[18]

In order to further develop porous LCEs, we raised a new question in the present study: can we use some sort of removable particles that not only serves as template for creating pores, but also have other exploitable functions, i.e., an active porogen. Our reflection led to the choice of a MOF: MIL-88A (MIL=Materials from Institute Lavoisier) for the following reasons: 1) The introduction of MOF into LCE matrix allows for creating molecular-scale pores, since MOF is porous materials in itself.[19] 2) The MOF used, MIL-88A, is flexible and deformable upon absorption of water molecules into the cavity through the for

formation of hydrogen bonds between water molecules and the framework.[20] 3) MOF can also be easily removed like other passive inorganic particles. Here, we report the investigation of loading MIL-88A particles in LCE actuator. As shown below, new and interesting actuation features are discovered with this materials combination. These include: 1) partial removal of MOF particles along the thickness direction of LCE-MOF films leads to an unusual actuation behavior in water; 2) removal of MOF from the actuator through acid etching produces not only pores but also magnetic ion oxides, like Fe_3O_4, which enables magnet-driven and guided movement of porous LCE actuator on various substrate surfaces; and 3) the in situ formation of iron oxide enhances the photothermal effect upon light absorption, which allows for the preparation of light fueled soft microcrawler.

4.3.3 Results and Discussion

4.3.3.1 Effect of MOF on LCE Actuator

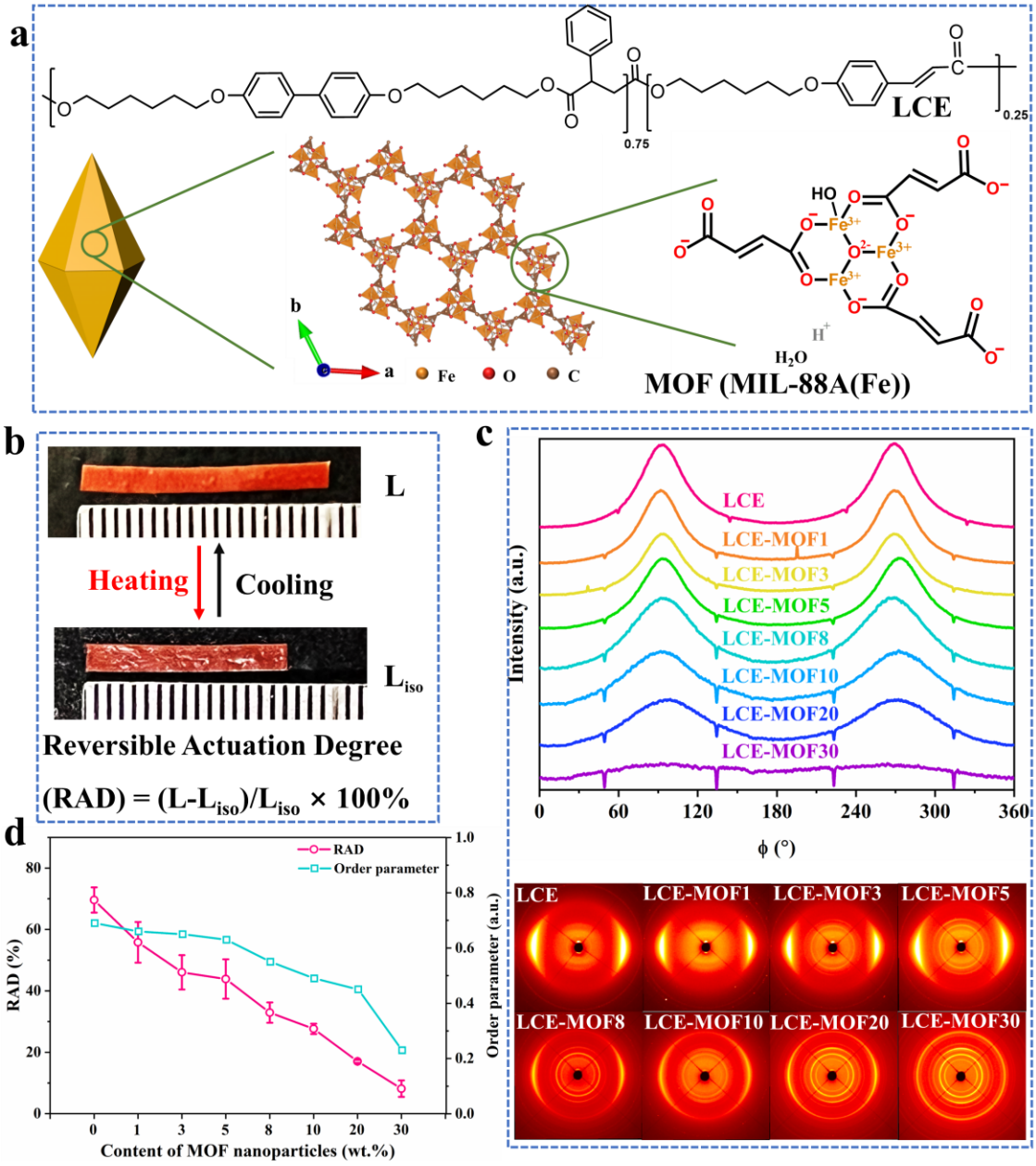

Figure 1. (a) Chemical structures of the used liquid crystal elastomer and MIL-88A, with the schematic illustration showing the porous structure of the MOF. (b) Photographs of an LCE- MOF20 (20 wt.% of MIL-88A) strip actuator displaying reversible elongation (at

room temperature, L=10 mm) and contraction (at 65 °C, in isotropic state, L_{iso}=8 mm), the reversible actuation degree. (Scale: 0.5 mm) (c) 2D-XRD patterns (top) and azimuthal diffraction profiles (bottom) (2θ =17° - 21° for nematic order) of LCE, LCE-MOF1, 3, 5, 8, 10, 20, 30. (d) Plots of RAD and order parameter of mesogens vs. MOF content for LCE-MOF actuators, showing the effect of increasing the MIL-88A content, the order parameter being calculated by the azimuthal diffraction profiles of each actuator.

Figure 1a shows the chemical structures of the materials used for the MOF-loaded LCE actuator main chain liquid crystal elastomer (LCE). The MIL-88A was synthesized using a surfactant-assisted method.[21] Elongated hexagonal bipyramidal MIL-88A nanocrystals were prepared by heating a mixture of $FeCl_3 \cdot 6H_2O$, fumaric acid and poly(vinylpyrrolidone) (PVP) as surfactant in N,N-dimethylformamide (DMF) at 85 °C for 2 h. The characterization results are shown in Figure S1. As analyzed from SEM images, the crystals have an average size of 680 ±100 nm in length and 540 ± 80 nm in width. As expected, XRD and infrared spectroscopic measurements show swelling of the crystals when immersed in water, corresponding to the characteristic transition from closed to the open form of MIL-88A.[22] Their porosity was measured through BET isothermal adsorption and desorption of nitrogen gas at 77 K, and the results indicate a distribution of pore sizes in the synthesized MIL-88A ranging from 9 nm to 83 nm and around 47 nm for the majority. As for the LCE bearing biphenyl mesogens and cinnamyl comonomer units for photo-crosslinking of polymer chains, it was synthesized by polycondensation using a previously reported method (Figure S2).[23]

The LCE-MOF actuators containing various amounts of MIL-88A (from 1 to 30wt%) were prepared. The typical preparation procedure consists in two steps. The first step is to obtain MOF-dispersed polydomain LCE film. To this end, a solution of MIL-88A crystals dispersed in THF and a solution of LCE dissolved in THF were mixed. The mixed solution was then poured into a Teflon mold and, after drying, the LCE/MOF mixture was subjected

to hot-compression to yield a film. DSC measurements found that the presence of MIL-88A particles has little effect on the thermal phase transition property of the LCE (Figure S3), as all mixture samples display a glass transition temperature (T_g) at around 25 °C and a nematic-isotropic phase transition (T_{ni}) in the range of 54 °C. In the second step leading to the actuators, the resulting LCE/MOF films were cut onto rectangular strips with a size of 10 mm × 2 mm × 180 μm in length, width and thickness, respectively. A given strip was mechanically stretched at 53 °C to 300% strain to induce uniaxial alignment of mesogens and then, under strain, exposed to UV light (320-480 nm filter, 90 mW cm^2, 2 h for each side) for photo-crosslinking the polymer. Afterward, the crosslinked LCE-MOF strip was heated into the isotropic state (65 °C) for relaxation and thermal equilibrium, thus completing the preparation of an actuator.

The reversible deformation or shape change of an LCE-MOF20 strip (the number in the acronym indicates the wt% of MIL-88A) can be seen from the photographs in Figure 1b, where the reversible actuation degree (RAD) is also defined. Given that RAD is related to the alignment of mesogens, the effect of MIL-88A particles on the stretching induced orientation of mesogens was investigated by means of XRD. Figure 1c compares the 2D-diffraction patterns and the azimuthal scans at 2q corresponding to the diffraction by mesogens for the actuators with different MOF contents. In all cases, as can be seen from the diffraction arcs on equator and the azimuthal diffraction profiles, mesogens remain aligned along the stretching direction. However, the orientation degree appears to decrease with increasing the MOF content. This is confirmed by Figure 1d showing the plot of the order parameter of mesogens vs. MOF content. This parameter is a measure of the average orientation of mesogens (1 for perfect orientation along the stretching direction and 0 for random alignment) and can be calculated from the azimuthal profiles. Also shown in Figure 1d is the plot of RAD vs. MOF content. It is clear that of the addition of MOF crystals in the LCE has an effect of reducing the orientation degree of mesogens and thus diminishing the reversible deformation. Indeed, RAD decreases continuously with increasing the

amount of MOF in the LCE and is down to only 8% for LCE-MOF30, meaning that MOF crystals hinder the retention of the orientation of mesogens in the LCE-MOF actuator.

It is not surprising that the MOF particles can affect the RAD, because their presence represents a portion of rigid and non-actuating mass in the soft LCE actuator. As for the effect on the orientation degree of mesogens, it is likely to be caused by the absorption of UV light by MIL-88A crystals (Figure S5a) that interferes with the absorption of cinnamyl groups for the photocrosslinking. In other words, under the same conditions for UV light photocrosslinking of stretched LCE/MOF strip, a higher content of MOF means more UV light absorption by the particles, which reduces the effective crosslinking of polymer chains through photodimerization of cinnamyl groups. This was confirmed by measuring the gel fraction in the LCE-MOF actuators (Figure S5b). The apparent gel fraction decreases with increasing the MOF content, as more uncrosslinked LCE chains (sol) was removed by immersing the actuator in THF 20 ml at 40 ºC for 3 hours. With this test, the actual gel fractions of the actuators may be higher than the apparent values, because it cannot be ruled out that some MOF particles could also diffuse out of the sample. But the effect of MOF particles to decrease the photocrosslinking degree is clear. Since uncrosslinked LCE chains in the actuators are relaxed in the isotropic phase and cannot contribute to the elongation of the strip on cooling to the LC phase, which accounts for the effect on RAD and the order parameter of mesogens. Nevertheless, even with 20% MIL-88A, the retained orientation of mesogens is still relatively prominent and the RAD remains substantial (close to 20%). Unless otherwise stated, the actuator of LCE-MOF20 was utilized in the diverse actuation experiments reported below.

4.3.3.2 Actuation Enabled by Water Absorption and Order-Disorder Phase Transition

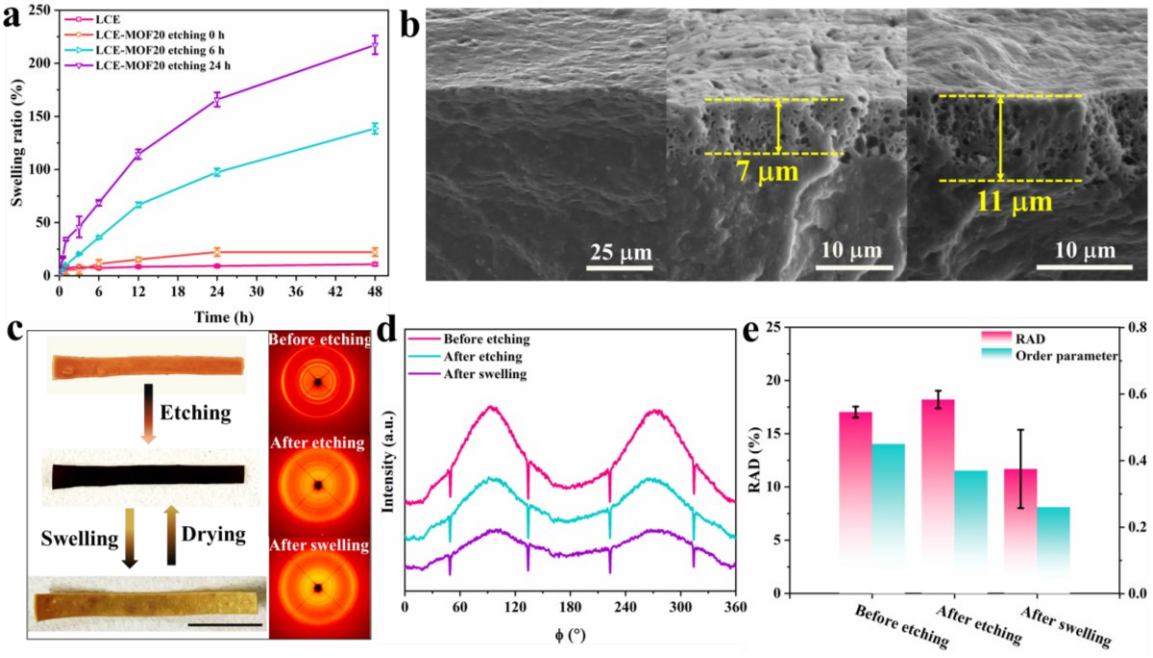

Figure 2. (a) Swelling ratio vs. immersion time in water for the actuator strips of neat LCE, and LCE-MOF20 before etching, and two LCE-MOF20 after 6 h and 24 h etching, respectively. (b) SEM cross-section images showing the propagation of etched region over time along the thickness direction of an LCE-MOF20 actuator at room temperature. Photos (scale bar: 5 mm) (c), 2D-XRD patterns azimuthal diffraction profiles (2θ =17° - 21°) (d), order parameter of mesogens and RAD values (e) (upon heating to 65 °C/cooling to room temperature) for an LCE-MOF20 actuator film before etching, after etching for 6 h, and with the etched film immersed in water for 12 h (swelling degree about 70%).

It is known that adding swellable MOFs in a polymer matrix, such as polyvinylidenedifluoride (PVDF), at a high content of 50 wt.%, or so can make the composite materials responsive to humidity changes, serving as a humidity sensor.[22a, 24] In the case of LCE-MOF actuator, we found that uncrosslinked LCE-MOF20 film can quickly respond to a high environmental humidity at 98% and deform due to swelling of LCE-MOF particles (Figure S6). However, the LCE-MOF20 actuator (crosslinked film) is not hygroscopic enough to

respond to the humidity changes, presumably due to the relative low MOF content (absence of continuous MOF phase) and the chain crosslinking that renders the hydrophobic polymer film denser. In order to preserve a reversible actuation governed by the LC-isotropic phase transition, the amount of MOF in the LCE actuator must be limited to 30 wt.% or below (Figure 1). Even with 30 wt.% of MIL-88A in the LCE-MOF actuator, the response to water vapor or high humidity was found to be still very slow. Nonetheless, as can be seen in Figure 2a, by immersing the LCE-MOF20 actuator in water, a higher swelling degree was observed as compared to the neat LCE actuator without MOF, implying that the presence of 20 wt.% MIL-88A improves the affinity of the material with water. Moreover, as mentioned above, MOF nanoparticles are also a template that can be removed by chemical etching to create macroporous LCE, which is expected to be able to uptake more water.[17] Indeed, the swelling degree of etched actuator is much greater than the unetched one and increases with increasing the etching time. The two etched LCE-MOF20 samples swell slowly but continuously over time, and at given immersing time the water absorption is more prominent for the sample with a longer etching time. As can be seen from the SEM cross-section images in Figure 2b, the etching depth of the LCE-MOF20 actuator increase from about 7 μm to 11 μm when the etching time prolongs from 6 h to 24 h. The formation of pores upon removal of MOF particles is also noticeable on the surface of LCE-MOF20 film after chemical etching for 6 h, with an average pore size of 540 nm, that are absent on the surface of the unetched film (Figure S7). For the two test samples of porous LCE-MOF, the LCE-MOF20 actuator was soaked in hydrochloric acid at room temperature for 6 h and 24 h, respectively, then washed thoroughly by water and ethanol, and finally dried in vacuum oven at 40 ^{o}C. The hydrogel-like water absorption of the porous actuator is explained by the large pore surface in the material and an enhanced affinity between the pore surface and water molecules due to residual ions after chemical etching.[17, 25]

The effect of etching and water absorption on the alignment of mesogens and the reversible actuation was then investigated, and the results are presented in Figure 2c,d,e. From the

photos, it is visible that the etching darkens the LCE-MOF20 actuator, while after absorption of water, the swollen actuator increases its size significantly. Form the XRD measurements (2D patterns and azimuthal profiles), after etching, the alignment of mesogens is largely retained, while the diffractions at smaller angles due to MIL-88A is less discernible, indicating removal of MOF particles. For the swollen actuator, due to the presence of a large amount of water and the resulting expansion of the strip, the alignment of mesogens is decreased but still significant. Comparing their RAD, the etching shows no detrimental effect, but the water-swollen actuator has a reduced yet appreciable reversible deformation.

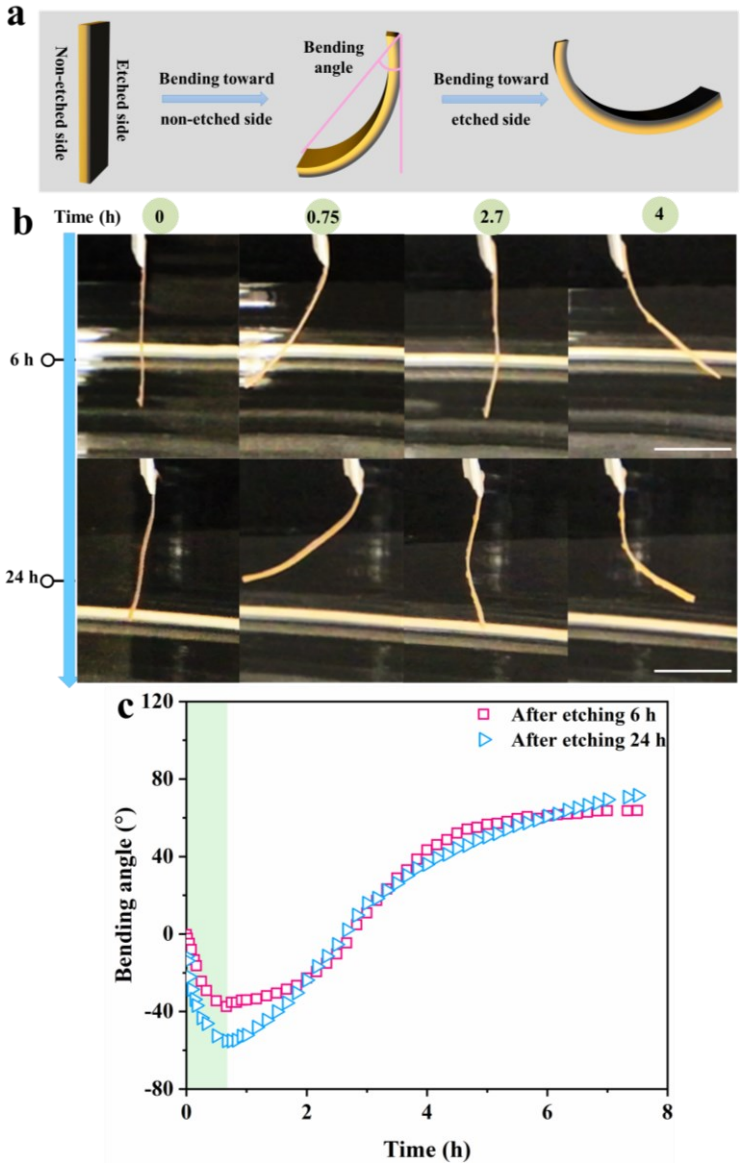

Figure 3. (a) Schematic illustration showing the asymmetric bending behavior of LCE-MOF20 strips and the definition of bending angle. (Black: etched side; Yellow: non-etched side) (b) Photographs displaying asymmetric bending of the LCE-MOF20 strips with different etching time 6 h and 24 h immersed in water for various times. (Scale bar: 5 mm) (c) Changes in bending angle of LCE-MOF20 strips with different etching times as an increase in immersion time in water.

The porous structure of the LCE-MOF actuator after removal of MIL-88A particles endows the material with hydrogel-like swelling in water while preserving the uniaxial alignment of mesogens. This observation can be exploited to generate new actuation features. To demonstrate an example, an asymmetric etching treatment was applied to LCE-MOF20 actuator by allowing etching to proceed only from one side of the film (see details in Experimental Section). Two actuator samples (thickness of about 70 μm) were subjected to the one-side etching for 6 and 24h, resulting in a porous layer of about 7 and 11 μm thick, respectively, on the etched side (Figure 2b). Therefore, the asymmetrical etching creates a bilayer structure in the monolithic actuator film (hereafter, the sake of discussion, the etched and unetched side are denoted as porous layer and MOF layer, respectively). Figure 3 show how these two films deform in water at room temperature, with a schematic illustration (a), photos (b), and plots of bending angle vs. time in water. For both samples, after immersion in water with one end of the flat strip fixed, in the first 50 min, the film bends toward the non-etched side, and the bending is more prominent for the film with a thicker porous layer (24 h etching). Beyond this time, the bending course is reversed, as the films start to unbend, recovering an essentially flat shape after about 2.7h, and go on to curl toward the etched side. After about 5h, the bending appears to reach equilibrium for the film with a thinner porous layer, but continues slowly for the film with a thicker porous layer. This peculiar deformation behavior of the LCE-MOF actuator is likely to stem from an asymmetrical water adsorption of the porous and MOF layer. At the beginning, the bending behavior is dictated by the porous layer that expands in volume due to relatively quick

water adsorption like hydrogel. This bending seems to reach equilibrium after about 45 min, probably counterbalanced by elastic force of the bended MOF layer, which is consistent with the higher mechanical modulus of the non-etched LCE-MOF20 film as compared to the etched sample. Then, the reversal of the bending course takes place at longer immersion time. At this point, a plausible explanation is the absorption of water by MOF particles in the MOF layer. Firstly, the MOF unit-cell volume exhibits reversible enlargement upon adsorption of water molecules owing to the formation of hydrogen bonds between guest molecules and the framework. This molecular-level swelling can be transferred to macroscopic deformation of the composite film. Seen from the SEM cross-section images, the thickness of the MOF layer is much thicker than that of the depth of the porous layer, which makes it possible for the MOF layer to absorb a large amount of water molecules as long as the soaking time is long enough. That is, although the swelling by the MOF layer is much slower than the porous layer, the influence of its volume expansion is larger. Secondly, although the interface between the two layers seems quit sharp based on the SEM images (Figure 2b), there should be an etching gradient. After the water absorption reaches equilibrium at the porous side, water molecules can find paths to diffuse through the interface. In other words, the porous layer may accelerate the swelling of the MOF layer. Thirdly, the mechanical properties of two layer are unbalanced, as the MOF layer is mechanically stronger than the porous layer. The effect of the depth of etched porous layer on the bending and reversed bending actuation in water can be seen from the plots of bending angle vs. immersion time for the two samples (Figure 3c).

4.3.3.2 Magnetically Responsive LCE-MOF Actuator with Enhanced Photothermal Effect

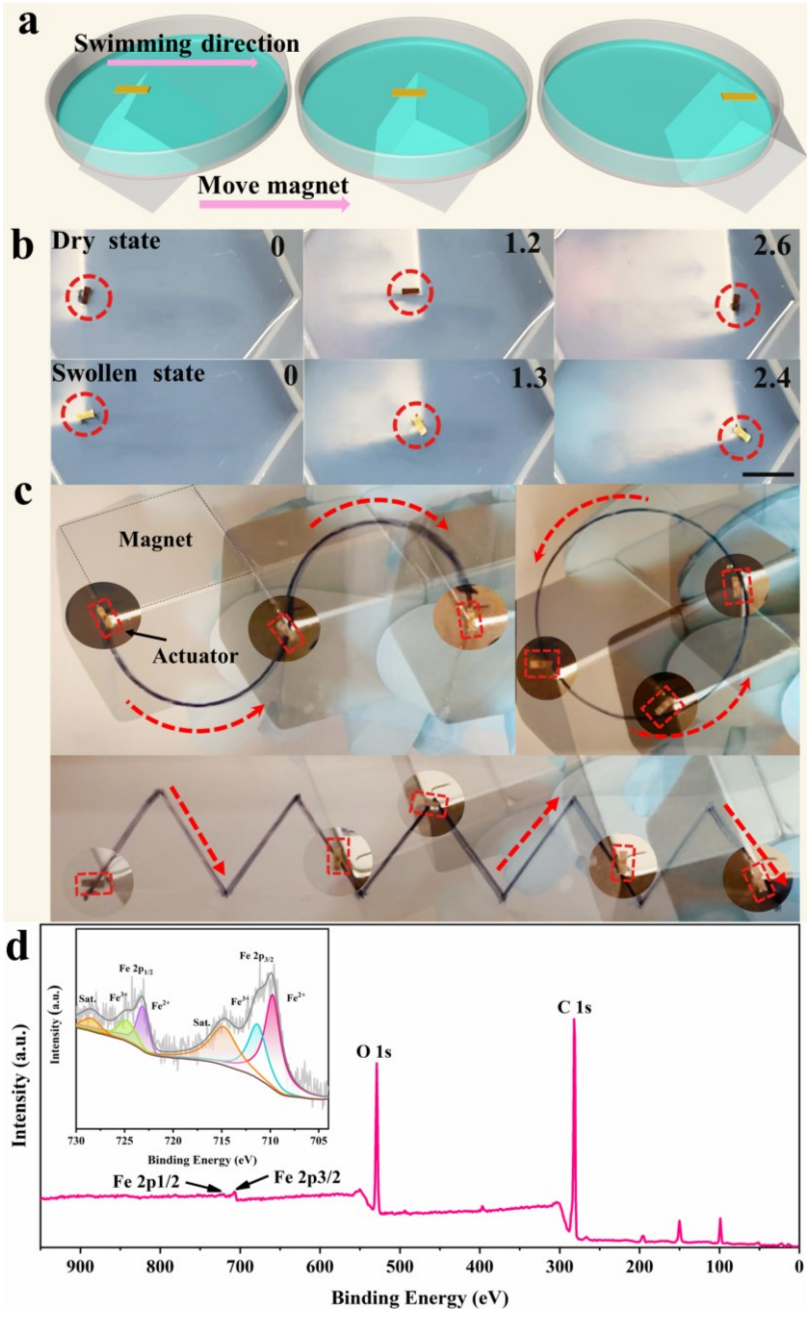

Figure 4. (a) Setup used to drive the movement of etched LCE-MOF actuator using a magnet. (b) Snapshots showing the motion of an LCE-MOF20 actuator at dry state (3 mm ×

1.3 mm × 70 μm) and swollen state (3.4 mm × 1.5 mm × 102 μm) movement directed by magnet (cubic magnet 2.4 cm × 2.4 cm × 2.4 cm). The distance between the actuator and magnet is 1.75 mm. Scale bar: 1 cm. (c) Snapshots showing the swimming of the dry actuator in multiple directions guided by magnet, tracing shapes of "S" (diameter: 28.6 mm), round (diameter: 34.9 mm) and "zigzag" (angle: 45°, each side of length: 21.2 mm). Maintaining the relative motion between the actuator and the magnet at 0. Scale bar: 1 cm. (d) XPS spectrum of etched LCN-MOF20 sample. The inset shows the corresponding high-resolution scans of Fe 2p.

The initially yellow LCE-MOF actuator film turns black after acid etching (Figure 2c). Interestingly, we found that the blackened porous LCE-MOF actuator is magnetic and can be moved by a magnet. Figure 4a is a schematic of the setup used to displace an actuator using a magnet. A piece of actuator is put on the surface of a water layer cast on a glass substrate, a magnet is positioned underneath and moves to bring the actuator to move with it. The recorded maximum "swimming" speed of the actuator corresponds to the fastest speed of the magnet at which the actuator is able to stay with it, i.e., the relative motion speed between the two is zero. As shown in Figure 4b, an LCE-MOF20 film (3 mm ×1.3 mm ×70 μm) can swim on water surface dragged by the motion of the magnet at a speed of 12 mm/s (Movie S1). Even after being swollen in water to have a swelling ratio of about 51%, the magnet-guided moving speed remains the same. In addition, the size of the actuator and its distance from the magnet can affect the swimming speed. As presented in Figure S8. at a constant distance of 1.75 mm between actuator and magnet (thickness of the substrate 0.25 mm + the thickness of the water layer 1.5 mm) the maximum swimming speed was observed to first increase from about 4 mm/s at body length of 2 mm to 12 mm/s at body length of 3 mm, and then decrease to 6 mm/s at body length of 10 mm. Strips of greater length exhibit greater resistance from water, and thus it is hard to move upon same magnetic force. However, at the length of 2 mm, the length is too short to move probably because the magnetic force exerted on the strip is weak. On the other hand, using the same

actuator of 3 mm in length, the swimming speed decreases sharply with the distance between actuator and magnet, dropped from 12 mm/s at distance of 1.75 mm to 4 mm/s at distance of 5.25 mm. As depicted in Figure 4c, by tracking the motion trajectory of the magnet, the actuator can be magnetically guided to execute multidirectional movements, drawing "S", round, and "zigzag" shape (Movie S2).

We carried out a number of experiments in an effort to understand how the etching make the LCE-MOF actuator responsive to magnetic field. Knowing the presence of Fe^{3+} in the structure of MIL-88A, it would be possible that during the acid etching for the removal of MOF particles, somehow magnetic iron oxides, such as Fe_3O_4, was formed inside the porous actuator. In a control test, an LCE-MOF20 film was subjected to the same conditions as for the actuator preparation, only without UV irradiation to photo-crosslinking. After the acid etching, the film didn't turn black, but became opaque due to light scattering from the porous structure (Figure S9), which is in agreement with a previous report, where no magnetic film was found after etching of MIL-88A@PVDF composite film.[26] The result of this control experiment implies that UV irradiation of the LCE-MOF film prior to chemical etching is a prerequisite for endowing the magnetic property to the actuator. Indeed, UV light is known to reduce Fe^{3+} to Fe^{2+} that is required for the formation of Fe_3O_4, the etching-induced formation of magnetic iron oxide. Therefore, plausible mechanism can be proposed as follows. Firstly, when the LCE-MOF20 film is subjected to UV light for photocrosslinking in air under ambient conditions, MIL-88A particles can absorb the incident UV light and undergo photo-transformation reactions leading to reduction of part of Fe^{3+} to Fe^{2+}, classified as "Fenton-like" reaction.[27] Subsequently, the LCE-MOF20 film containing mixture of Fe^{3+} and Fe^{2+} ions is successively etched in HCl (12 M), rinsed in DI, and finally dried in a vacuum oven at 40 ºC for 6 h. In the course of the whole treatment, Fe_3O_4 nanoparticles are formed,[28] making the film appear black after drying. X-ray electron spectroscopy (XPS) measurements were performed on the etched LCE-MOF20 film. The spectrum in Figure 4d shows the presence of carbon, oxygen, and iron, arising from

LCE and, presumably, Fe_3O_4. Normally, Fe_3O_4 is an intermediated phase which contains both Fe^{2+} and Fe^{3+} ions in an alternating manner,[29] the spin-orbit splitted Fe 2p peaks are broad due to a small chemical shift between Fe^{3+} and Fe^{2+} presented in Fe_3O_4.[30] From the high-solution scan of Fe 2p in the inset, the Fe $2p_{3/2}$ and Fe $2p_{1/2}$ peaks are well fitted with a major peak at 709.8 eV and 723.2 eV, and a minor one at 711.4 eV and 724.9 eV, which can be ascribed to Fe^{2+} and Fe^{3+}, respectively.[31] In addition, it is well recognized that the various oxides of iron can be distinguished from each other by their characteristic satellite features, which arise due to the charge transfer screening in the spectra.[30] For the etched LCE-MOF20 film, the presence of a shakeup satellite peak situated at 714.9 eV is contributed to Fe^{2+} in the FeO. On the basis of the above experiments and analysis, we attribute the magnetic property of the porous LCE-MOF actuator to the UV light-assisted, acid etching-induced formation of Fe_3O_4 nanoparticles.

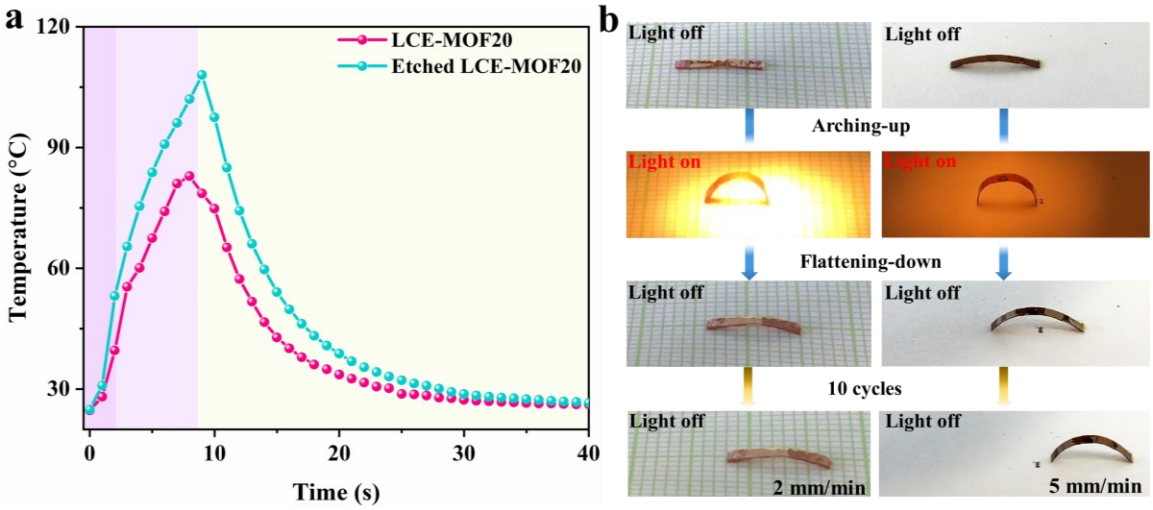

Figure 5. (a)Temperature variation of LCE-MOF20 film before and after etching upon exposure to NIR light (3.0 $W \cdot cm^{-2}$) and after light-off. (b) Photographs showing light-driven locomotion of two bilayer actuators composed of a passive Kapton top layer and an active bottom layer that is either LCE-MOF20 before etching (left) or after etching (right) (actuator size: 9 mm × 1.3 mm in length and width, respectively, and Kapton and LCE-

MOF20 films have a thickness of 30 μm and 100 μm, respectively). Light intensity: 3 $W \cdot cm^{-2}$, light on 2s /off 8s).

Moreover, the in situ formation of black iron oxide nanoparticles imparts the LCE-MOF actuator with enhanced photothermal effect. The reversible deformation of LCE actuator associated with the order-disorder phase transition can be translated into movement (locomotion). Using light to enable the locomotion via photothermal effect is a well-established approach, where light on/off cycles are applied to induce cyclic heating/cooling of the LCE actuator. Generally, this approach requires the loading in the LCE of a photothermal agent such dye, carbon nanotube, graphene.[9, 32] For LCE-MOF actuator, light-absorbing MOF can serve as a photothermal agent, but the photothermal effect is less efficient than the iron oxide nanoparticles. Figure 4a compares the temperature profiles of a non-etched and an etched LCE-MOF20 film upon exposure to a light source (3.0 W. cm^{-2}, mostly in NIR region). The temperature rises faster and higher for the etched film than the non-etched one, likely due to greater light absorption and release of heat with Fe_3O_4 nanoparticles.[33] This enhanced photothermal effect can be exploited for more efficient light-fueled locomotion, because a shorter light-on time is required for heating above the LC-isotropic phase transition, meaning that more deformation cycles can be realized within a period of time. Figure 5b shows a caterpillar-like microwalker consist of etched LCE-MOF20 (Figure 5b right) as active layer at bottom side and Kapton as passive layer at top side. Under irradiation of light on/off cycles, this microwalker undergoes arching-up (light on) and flattening-down (light off) shape change and walks due to friction bias (Movie S3, Supporting Information) due to photothermal effect inducing ordered to disordered phase transition. By repeating the arching/flattening for 10 cycles upon the irradiation of light on/off cycles, the actuator can walk from left to right, at an average speed of 5 mm/min. For comparison, we observe that the speed of microwalker fabricated by non-etched LCE-MOF20 (Figure 5a left) is slower that than of etched sample, which is 2 mm/min (Movie S3, Supporting Information). The result demonstrates that the formation of magnetic layer significantly enhanced the

photothermal effect, leading to a decrease of response time and improving the speed of actuation, which is of great importance in the application of soft robots.

4.3.4 Conclusions

We have developed a new feasible approach to fabricate a water-absorbing, magnetic-, and photo-responsive LCE actuator based on introducing swellable MOF crystals as active porogen. An interesting finding about the LCE-MOF20 actuator is the UV light-assisted etching-induced in-situ formation of Fe_3O_4 nanoparticles which endows the porous LCE-MOF actuator with magnetic property and enhanced photothermal effect. Magnet-directed movements of the actuator on water surface as well as light-fueled locomotion of LCE-MOF-based bilayer actuator were realized. Moreover, the actuator after MOF removal exhibits hydrogel-like swelling in water while retaining the alignment of mesogens, which allows the LCE-MOF actuator to display reversible deform either through water absorption/desorption or order-disorder phase transition, which offers actuation flexibility and versatility.

4.3.5 Experimental Section

Synthesis of Liquid Crystal Polymer

Unless stated otherwise, all reagents and chemicals were obtained from commercial sources. 4,4'-Dichloromethane (99%) was purchased from Fisher Scientific; p-coumaric acid (99%), 6-chlorohexanol (96%) and phenylsuccinic acid (98%) from Sigma Aldrich. They were used as received without further purification. The monomer 4,4'-bis(6 hydroxyhexyloxy)biphenyl (BHHBP) and the crosslinker 4-(6-Hydroxyhexyloxy) cinnamic acid (6HCA) were synthesized by using a literature method.[23] The main chain liquid crystal polymer (LCP) was synthesized by polycondensation. Fort the reaction, the monomer BHHBP (1.1596 g, 0.003 mol), PSA (0.5825 g, 0.003 mol), crosslinker 6HCA (0.2114 g, 0.001mol), catalysts $Zn(Ac)_2$ (0.0039 g, 0.2 wt.%) and Sb_2O_3 (0.0059 g, 0.3 wt.%) were loaded into a 100-mL three-necked flask, equipped with nitrogen inlet and outlet, a

mechanical stirrer, and a distillation trap connected to a vacuum line. Before the reaction, the oxygen in the flask was removed by vacuum pumping and nitrogen protection. The reaction was then proceeded through the following steps: 1) The flask was placed in a silicone oil bath pre-heated to 180 °C, held it for 1 h before heating stepwise from 180 °C to 200 °C for 1.5 h. 2) Under a low vacuum, the temperature was kept at 200 °C for 0.5 h. 3) The temperature was maintained at the 200 °C with a high vacuum of 30-50 Pa for 3 h. 4) After the polycondensation reaction was completed, and then LCP was purified by percipitating in methanol and dried under vacuum 40 °C and collected.

Synthesis of MIL-88A particles

$FeCl_3 \cdot 6H_2O$ and fumaric acid were purchased from Sigma Aldrich. The procedure of synthesis according to the literature[21] is as follows. $FeCl_3 \cdot 6H_2O$ (1.3518 g, 5 mmol), fumaric acid (0.5813 g, 5 mmol), and PVP (1.5011 g, 5 mmol) were added into the round-flask at temperature 85 °C for 2 h. Then, the obtained brown powder was centrifuged and washed by DMF, and ethanol, and dried at 100 °C under vacuum.

Preparation of LCN-MOF films

MOF nanoparticles (0.9, 2.8, 4.7, 7.8, 10, 22.5, 38.6 mg, respectively) were mixed with LCP (0.09 g) in THF (4 ml) and then sonicated for 5 min. The mixed solution was casted onto a PTFE mold, the solvent was evaporated in a vacuum oven at 40 °C for 6 h. The resulting LCE-MOF films with different contents of MOF nanoparticles (thickness of 180 mm) were compressed at 90 °C using a hydraulic press, followed by cooling to room temperature. The preparation of LCE-MOF actuator with uniaxially aligned mesogens consists in two steps. First, a film was cut into strips of 10 mm × 2 mm in length and width, respectively, which were stretched at 53 °C in water bath to 40 mm × 1.3 mm × 80 mm, with the final strain at 300 % after removal of extra stress. Second, the stretched film under strain was crosslinked under UV light (320-480 nm filter, 90 mW cm^2) for both side (2 h for each side) for full and uniform crosslinking.

Preparation of etched LCN-MOF films

The crosslinked films of LCE-MOF20 were soaked in HCl (12 M) for a period of time (6-24 h), and then rinsed by DI water for 10 min and ethanol for 35 min. To generate the asymmetric bending actuation behavior, the LCE-MOF20 films were tapped on a glass substrate, allowing only one side to be in contact HCl solution for 6-24 h, followed by washing using DI water for 10 min and ethanol for 35 min. The etched LCE-MOF films were dried in a vacuum oven at 40 °C for 6 h.

Characterization

2D-XRD patterns were recorded on a Bruker AXS Nanostar system with a microfocus copper anode, montal optics and a VANTEC 2000 2D detector at 55 mm from the samples, with 0.154 nm X-ray wavelength and the azimuthal scans of 360º were measured at 2θ = 17-28º (for mesogens). The attenuated total reflection-Fourier transform infrared (ATR-FTIR) spectra were recorded on a Nicolet-IS10 (Thermo Electron Co.) spectrometer with resolution of 4 cm^{-1}. The morphology of MOF nanoparticles and LCE-MOF films before and after etching were examined using a Hitachi S-4700 field-emission-gun scanning electron microscope (SEM) operating at 1-10 kV. An UV-Vis-NIR spectrometer (Varian) was used to measure the absorption spectra of the MIL-88A in water solution from 190 nm to 1100 nm. Phase transition temperatures were determined by using a differential scanning calorimeter (DSC, TA Q200) in the range of -20 to 120 ºC at a heating or cooling rate of 10 ºC min^{-1}, under protection of nitrogen flowing at 50 ml min^{-1}. X-ray electron spectroscopy analysis was performed using an XPS Axis UltraDLD from company Kratos at to quantify the elements. BET measurements (using ASAP 2020 analyzer) were conducted to determine the pore size and pore distribution of MOF nanoparticles at 77 K. For light-triggered deformation, a lamp (Flash Torch) was used to irradiate the samples, and the light intensity was measured using a power meter (TURNER, gentec-co Company).

4.4 Supporting Information

Supporting Information is available from the Wiley Online Library or from the author.

4.5 Acknowledgements

Y. Zhao acknowledges the financial support from the Natural Sciences and Engineering Research Council of Canada (NSERC), le Fonds de recherche du Québec: Nature et technologies (FRQNT), and The Centre québécois sur les matériaux fonctionnels. J. Jiang is grateful to China Scholarship Council (CSC) for providing her with a scholarship to study and live in Canada. Dr. Fortin is acknowledged for assisting the XRD measurements. Dr. Blais is acknowledged for helping the XPS measurements. Dr. St-Louis is acknowledged for conducting the BET test.

4.6 Conflicts of Interest

There are no conflicts to declare.

4.7 Author Contributions

J. J. and Y. Z. conceived the ideas. J. J. fabricated samples and collected data. Y. R. M. collected data. R. D. C. discussed and analyzed the XPS results. J. J. and Y. Z. wrote the manuscript.

4.8 References

[1] a) M. A. Stuart, W. T. Huck, J. Genzer, M. Muller, C. Ober, M. Stamm, G. B. Sukhorukov, I. Szleifer, V. V. Tsukruk, M. Urban, F. Winnik, S. Zauscher, I. Luzinov, S. Minko, *Nat. Mater.* **2010**, *9*, 101-113; b) M. Pilz da Cunha, Y. Foelen, T. A. P. Engels, K. Papamichou, M. Hagenbeek, M. G. Debije, A. P. H. J. Schenning, *Adv. Opt. Mater.* **2019**, *7*, 1801604.

[2] a) F. Xia, L. Jiang, *Adv. Mater.* **2008**, *20*, 2842-2858; b) M. Ilami, H. Bagheri, R. Ahmed, E. O. Skowronek, H. Marvi, *Adv. Mater.* **2020**, e2003139; c) F. Ge, Y. Zhao, *Adv. Funct. Mater.* **2019**, *30*, 1901890.

[3] a) J. E. Stumpel, E. R. Gil, A. B. Spoelstra, C. W. M. Bastiaansen, D. J. Broer, A. P. H. J. Schenning, *Adv. Funct. Mater.* **2015**, *25*, 3314-3320; b) L. Hu, Q. Zhang, X. Li, M. J. Serpe, *Mater. Horizons* **2019**, *6*, 1774-1793.

[4] a) T. J. White, D. J. Broer, *Nat. Mater.* **2015**, *14*, 1087-1098; b) T. H. Ware, J. S. Biggins, A. F. Shick, M. Warner, T. J. White, *Nat. Commun.* **2016**, *7*, 10781; c) L. Yin, L. Han, F. Ge, X. Tong, W. Zhang, A. Soldera, Y. Zhao, *Angew. Chem. Int. Ed.* **2020**, *59*, 15129-15134; d) D. Mistry, N. A. Traugutt, B. Sanborn, R. H. Volpe, L. S. Chatham, R. Zhou, B. Song, K. Yu, K. N. Long, C. M. Yakacki, *Nat. Commun.* **2021**, *12*, 6677.

[5] a) Y. Y. Xiao, Z. C. Jiang, J. B. Hou, Y. Zhao, *Nat. Commun.* **2021**, *12*, 624; b) M. Pilz da Cunha, Y. Foelen, R. J. H. Raak, J. N. Murphy, T. A. P. Engels, M. G. Debije, A. P. H. J. Schenning, *Adv. Opt. Mater.* **2019**, *7*, 1801643; c) M. Liu, L. Jin, S. Yang, Y. Wang, C. B. Murray, S. Yang, *Adv. Mater.* **2023**, *35*, e2208613.

[6] M. O. Saed, A. Gablier, E. M. Terentjev, *Chem. Rev.* **2022**, *122* (5), 4927-4945.

[7] Z. C. Jiang, Y. Y. Xiao, J. B. Hou, X. S. Chen, N. Yang, H. Zeng, Y. Zhao, *Angewandte Chemie* **2022**.

[8] Z. Liu, H. K. Bisoyi, Y. Huang, M. Wang, H. Yang, Q. Li, *Angew. Chem. Int. Ed.* **2022**, *61*, e202115755.

[9] Z.-C. Jiang, Y.-Y. Xiao, R.-D. Cheng, J.-B. Hou, Y. Zhao, *Chem. Mater.* **2021**, *33*, 6541-6552.

[10] J. Hu, Z. Nie, M. Wang, Z. Liu, S. Huang, H. Yang, *Angew. Chem. Int. Ed.* **2023**, *62*, e202218227.

[11] Z. Z. Nie, B. Zuo, M. Wang, S. Huang, X. M. Chen, Z. Y. Liu, H. Yang, *Nat. Commun.* **2021**, *12*, 2334.

[12] a) H. P. C. van Kuringen, G. M. Eikelboom, I. K. Shishmanova, D. J. Broer, A. P. H. J. Schenning, *Adv. Funct. Mater.* **2014**, *24*, 5045-5051; b) C. L. Gonzalez, C. W. M. Bastiaansen, J. Lub, J. Loos, K. Lu, H. J. Wondergem, D. J. Broer, *Adv. Mater.* **2008**, *20*, 1246-1252.

[13] D. Dasgupta, I. K. Shishmanova, A. Ruiz-Carretero, K. Lu, M. Verhoeven, H. P. van Kuringen, G. Portale, P. Leclere, C. W. Bastiaansen, D. J. Broer, A. P. Schenning, *J. Am. Chem.l Soc.* **2013**, *135*, 10922-10925.

[14] a) Y. Zhan, D. J. Broer, D. Liu, *Adv. Mater.* **2023**, *35*, e2211143; b) Y. Zhan, S. Calierno, J. Peixoto, L. Mitzer, D. J. Broer, D. Liu, *Angew. Chem. Int. Ed.* **2022**, *61*, e202207468.

[15] Y. Shang, J. Liu, M. Zhang, W. He, X. Cao, J. Wang, T. Ikeda, L. Jiang, *Soft Matter* **2018**, *14*, 5547-5553.

[16] M. E. Prevot, H. Andro, S. L. M. Alexander, S. Ustunel, C. Zhu, Z. Nikolov, S. T. Rafferty, M. T. Brannum, B. Kinsel, L. T. J. Korley, E. J. Freeman, J. A. McDonough, R. J. Clements, E. Hegmann, *Soft Matter* **2018**, *14*, 354-360.

[17] J. Jiang, L. Han, F. Ge, Y. Xiao, R. Cheng, X. Tong, Y. Zhao, *Angew. Chem. Int. Ed.* **2021**, *61*, e202116689.

[18] J. Jiang, Y. Zhao, *Small* **2023**, e2301932.

[19] a) M. Kalaj, K. C. Bentz, S. Ayala, Jr., J. M. Palomba, K. S. Barcus, Y. Katayama, S. M. Cohen, *Chem. Rev.* **2020**, *120*, 8267-8302; b) Q. Qian, P. A. Asinger, M. J. Lee, G. Han, K. Mizrahi Rodriguez, S. Lin, F. M. Benedetti, A. X. Wu, W. S. Chi, Z. P. Smith, *Chem. Rev.* **2020**, *120*, 8161-8266.

[20] a) P. Kanti Chattopadhyay, N. Ranjan Singha, *Coord. Chem. Rev.* **2021**, *446*, 214125; b) C. Serre, F. Millange, S. Surble, G. Ferey, *Angew. Chem. Int. Ed.* **2004**,

43, 6285-6289; c) C. Mellot-Draznieks, C. Serre, S. Surblé, Audebrand N., G. Férey, *J. Am. Chem.l Soc.* **2005**, *127(46)*, 16273-16278; d) C. M. D. C. Serre, C. Mellot-Draznieks, S. Surblé, N. Audebrand, Y. Filinchuk, G. Férey, *Science* **2007**, *315(5820)*, 1828-1831.

[21] X. Cai, J. Lin, M. Pang, *Cryst. Growth Des.* **2016**, *16*, 3565-3568.

[22] a) J. Troyano, A. Carne-Sanchez, J. Perez-Carvajal, L. Leon-Reina, I. Imaz, A. Cabeza, D. Maspoch, *Angew. Chem. Int. Ed.* **2018**, *57*, 15420-15424; b) N. Alipanah, H. Yari, M. Mahdavian, B. Ramezanzadeh, G. Bahlakeh, *J. Ind. Eng. Chem.* **2021**, *97*, 200-215.

[23] R. Yang, Y. Zhao, *Angew. Chem. Int. Ed.* **2017**, *56*, 14202-14206.

[24] S. Lv, L. Shuai, W. Ding, W. Ke, B. Wang, J. Wan, *Adv. Fiber Mater.* **2021**, *3*, 107-116.

[25] a) A. K. Tiwari, J. P. Goss, P. R. Briddon, N. G. Wright, A. B. Horsfall, R. Jones, H. Pinto, M. J. Rayson, *Phys. Rev. B* **2011**, *84*, 245305; b) Q. Zhao, J. W. Dunlop, X. Qiu, F. Huang, Z. Zhang, J. Heyda, J. Dzubiella, M. Antonietti, J. Yuan, *Nat. Commun.* **2014**, *5*, 4293.

[26] J. Troyano, A. Carne-Sanchez, D. Maspoch, *Adv. Mater.* **2019**, *31*, e1808235.

[27] A. D. Bokare, W. Choi, *J. Hazard. Mater.* **2014**, *275*, 121-135.

[28] Darminto, M. N. Cholishoh, F. A. Perdana, M. A. Baqiya, Mashuri, Y. Cahyono, Triwikantoro, F. Iskandar, M. Abdullah*, Vol. 1415(1)*, **2011**, pp. 234-237.

[29] S. Kaya, H. Ogasawara, A. Nilsson, *Catal. Today* **2015**, *240*, 184-189.

[30] S. Tiwari, R. Prakash, R. J. Choudhary, D. M. Phase, *J. Phys. D Appl. Phys.* **2007**, *40*, 4943-4947.

[31] W. W. A. Barbieri, M.A. Van Hove, G.A. Somorjai, *Surf. Sci.* **1994**, *302(3)*, 259-279.

[32] a) F. Ge, R. Yang, X. Tong, F. Camerel, Y. Zhao, *Angew. Chem. Int. Ed.* **2018**, *57*, 11758-11763; b) Y. Yu, L. Li, E. Liu, X. Han, J. Wang, Y.-X. Xie, C. Lu, *Carbon* **2022**, *187*, 97-107; c) Y. Yang, W. Zhan, R. Peng, C. He, X. Pang, D. Shi, T. Jiang, Z. Lin, *Adv. Mater.* **2015**, *27*, 6376-6381.

[33] Y. Wu, S. Zhang, Y. Yang, Z. Li, Y. Wei, Y. Ji, *Sci. Adv.* **2022**, *8 (25)*, eabo6021.

CHAPTER 5. GENERAL DISCUSSION AND CONCLUSION

To broaden the class of the liquid crystal polymer only based on the dense structure and explore the new actuation behavior in response to stimuli, in this thesis, we put forward two specific approaches to develop porous LCEs with additive filling-based reconfigurable functions, and explore their applications in deformable electronic devices and MOF-based multi-stimuli responsive actuation behaviors. In this chapter, we will discuss the strengths and limitations of porous LCEs-based systems, emphasizing the key concepts and strategies developed in these works.

5.1 General Discussion

5.1.1 Porous LCNs with Reconfigurable Functions and Their Application in Deformable Electronic Sensor

In the first part of research works, a new class of porous LCNs was found to exhibit peculiar actuation functions, namely, hydrogel-like actuation behavior (Chapter 2), and their interesting application in deformable electronic sensor by filling ionic liquid (IL) was explored (Chapters 2 and 3). On the one hand, a simple and efficient direct templating approach is employed to fabricate LCNs with pore structure. The creation of porosity makes the initially hydrophobic LCN behave like conventional hydrogel, capable of absorbing a large volume of water. However, different from conventional hydrogel undergoing isotropic swelling in water, the porous LCN actuator exhibits anisotropic swelling upon a relatively low swelling ratio of about 100 %. Meanwhile, the retained uniaxial alignment of mesogens ensures a thermally induced shape change associated with LC-isotropic phase transition. In addition, this swelling behavior of porous LCN also depends on the crosslinking density of liquid crystal polymer network, which determines both the water-absorption-induced and order-disorder phase transition-induced shape transformation of the actuator. Although the similar swelling behaviors of nanoporous smectic liquid crystalline polymer have been found to change the membrane's capillary properties, (1, 2) the larger pores

generated by our template approach endow the LCN actuator with unexpected water absorption and diverse shape transformations, which is the highlight of this approach.

On the other hand, we explore the porous LCN actuator for reconfigurable functions. This is possible because the pores in the actuator can be used to load an active filler for a specific function and later on, after washing out the filled additive, reload another active filler for a different function, thus reconfiguring the function of the porous actuator. We have demonstrated this functionality with different functional fillers, including butyl-3-methylimidazolium tetrafluoroborate ($BMIMBF_4$) – an IL for electrical response, Vis523A - a dye for photothermal effect, and tetraphenylethylene (TPE) – a dye for blue fluorescence emission. This function reconfigurability allows for one single actuator system to possess different functions beyond actuation, which is different from the reconfigurability of shape change usually reported in the literature. (3) An important point to emphasize is that our porous LCN actuator has reconfigurable functions due to the presence of voids and the capability of water absorption, which neither non-porous LCN nor hydrogel alone can possess.

Furthermore, we discuss the question why the formation of pores in the hydrophobic LCNs makes it absorb a large amount of water like hydrogel. The mechanisms involve two aspect explanations. First, the observed contact angle change implies that the porous LCN becomes rather hydrophilic, leading to the absorption of water. And meanwhile, the SEM cross-section and surface images show that the porous LCN samples embed interconnected pore channels whose large surfaces with improved affinity with water molecules favor water uptake by capillary effect. Secondly, after etching treatment, a significant amount of residual ions (Ca^{2+} and Cl^-) trapped in the porous LCN sample helps absorb water.

For deformable electronic application, the effective loading of ionic liquids in porous LCE actuators makes this material potentially interesting. In the thesis, we have demonstrated the presence of separate or collective use of PLCE-IL as sensor and actuator. For sensing, electrical resistance variation resulting from multi-mode mechanical deformation (large

elongation, bending, twisting and vibration) and change in environment conditions (temperature, humidity) can be measured. In particular, the collective use of PLCN-IL as an active sensing and actuating component inside the structure of a device is appealing, with one of the two functions in action according to the need and necessity. This is the main difference from the few electric field-responsive LCE actuators reported in the literature. Those actuators, containing conduction additives like liquid metal, (4, 5) metal wire, (6) metal, (7) use Joule heating effect to induce the order-disorder phase transition and thus deformation/movement, while some systems can use the electrical feedback to correlate with the deformation in the same time.

Despite these advances and advantages, there are limitations of porous LCN actuator in terms of functions and applications that requires improvement through future research. Firstly, the porous LCN-based swelling is slow as compared to conventional hydrogel, due to the different mechanisms for water absorption, leading to the smaller shape deformations. Although in our study, we have tuned the porosity, crosslinking density for controlling degree of swelling, the observed time scale still limits the further applications of this actuator in the field of fast-response soft robotics. Therefore, to obtain fast swelling behavior of PLCN, new strategies for rational molecular/polymeric/material design need to be developed. New approaches for introducing controlled pore structures are also of interest to explore. Secondly, even though PLCE-IL based sensor could sense various kinds of mechanical deformation and changing environment conditions the achieved performance (sensitivity and especially selectivity) is not sufficient enough for monitoring and distinguishing various real-time motions in wearable devices. To address this issue, both innovative material design and ingenious devices fabrication need to be pursued. Thirdly, when non-actuating elements are created or introduced in the LCN actuator to endow the actuator with new functions or properties, such as the pores and ionic liquid in our porous LCN system, inevitably the actuation performance (reversible deformation) is most often, if not always, reduced to a certain degree. Therefore, achieving a good trade-off between the sought-after

new function and the actuation performance depending on the targeted application is essential. To this regard, in future studies it is certainly of great interest to find ways that allow LCE actuator to exhibit new functions while preserving the actuation performance.

5.1.2 Multi-stimuli-responsive LCE Actuators Using MOF as Active Porogen

In the second part of the research work (Chapter 4), we investigated a new "active porogen" strategy by incorporating metal-organic framework (MOF) crystals (MIL-88A) into LCE to form nanopores with the presence of MOF and macropores after MOF removal through chemical etching. The resulting actuator is multi-stimuli-responsive and can reversibly deform via two different mechanisms: upon water absorption/desorption and order-disorder phase transition. In this approach, MOF crystals not only serve as swellable nanoparticles but also act as a removable template for the formation of microporous structure. This combination of multiple advantages by loading one additive endows the LCE-based actuator with new functions, which is a significant advance in this field. In addition, compared to other inorganic additives, such as carbon nanotubes, graphene, liquid metal, and Fe_3O_4 nanoparticles, (6-11) MOFs crystals have better compatibility with polymer matrix, (12) which ensures their dispersion.

The macroporous LCE actuator after MOF removal can swell in water, which is similar to the use of other templates like $CaCO_3$. With MOF, the kinetics of the acid etching can be used to control the depth of the region where macropores appear, with an apparently rather sharp interface between the MOF-removed (macroporous) layer and the MOF-present (nanoporous) layer. Given their different water absorption amounts and rates, the possibility of spatially selected or patterned etching of the LCE-MOF actuator can be exploited for unusual shape changes both in water or combining water and heating/cooling. This has been demonstrated using actuator strips exposed to one-side etching.

After etching, the macroporous LCE-MOF actuator becomes magnetically responsive by reacting to a nearby magnet. This unexpected finding makes the LCE-MOF actuator more

interesting, as it can be driven by a magnet to move on water surface. On the basis of our characterization results and especially the control test showing the absence of this phenomenon if the LCE-MOF film is not irradiated by UV light for photo-crosslinking, we proposed the in situ formation of magnetic Fe_3O_4 nanoparticles in the etched actuator. At this point, the movement of the actuator is solely due to the attractive force towards the moving magnet, i.e., dragged to follow the magnet. In future studies, it would be interesting to use an alternating magnetic field to activate the LCE-MOF actuator through LC-isotropic phase transition. However, whether or not the magnetothermal effect is sufficient for heating remains to be seen. Another benefit of having Fe_3O_4 nanoparticles in the actuator is the enhanced photothermal effect. Although this effect can be provided by MOF particles (before etching), Fe_3O_4 nanoparticles absorb more light and generate more heat. We showed how the enhanced photothermal effect can be used in inducing light-driven movement through reversible deformation.

5.2 General Conclusion

The research works reported in this thesis focused on developing a new class of LCE actuators, namely porous LCE actuators, and exploring new functions and potential applications that distinguish them from conventional non-porous LCE actuators. The obtained results help to gain fundamental knowledge and improve understanding of porous LCEs. Two main achievements are as follows.

On the one hand, we demonstrated the preparation of porous LCEs actuator through simple templating method and found a peculiar actuation function, namely hydrogel-like water absorption of the initially hydrophobic LCE. The characterization results suggest that the remaining ions after etching increase the affinity of the LCE with water, and that the pore channels provide the diffusion path for water, which promote the ability of porous LCE to absorb water. This property enables 3D shape transformations driven by water absorption, in addition to the LCE actuation based on order-disorder phase transition. More

interestingly, we showed how to endow the actuator with reconfigurable functions through loading, removal and reloading of different active fillers in the same LCE actuator. Furthermore, we investigated the application of porous actuator filled with an ionic liquid (PLCE-IL) as a potential platform for two classes of functional materials: electrically responsive, deformable materials for sensing based on electrical resistance change and soft active materials for stimuli-triggered actuation based on reversible deformation. We demonstrated separate and collective use of the two functions with a single actuator, suggesting possible ways for merging deformable electronic and actuation applications.

On the other hand, we demonstrated the use of MOF as active porogens for making porous LCE actuators. The idea of loading MOF particles in LCE actuator offers new possibilities: 1) MOFs are porous materials in their own capacity and can play a role in forming molecular-scale pores in LCE. 2) The MOF used, MIL-88A, is flexible and deformable upon absorption of water molecules into the cavity. 3) MOF can also be removed by chemical etching like other passive inorganic particles. Indeed, our study revealed interesting actuation features. After removal of MOF, the actuator also exhibits hydrogel-like swelling in water while retaining the alignment of mesogens, which enables reversible deformation either through water absorption/desorption or order-disorder phase transition. Unexpectedly, the porous LCE-MOF actuator after etching becomes magnetically responsive, likely due to the in-situ formation of Fe_3O_4 nanoparticles in the actuator induced by acid etching and UV irradiation used for photocrosslinking. We showed magnet-directed movements of the actuator on water surface as well as light-fueled locomotion of LCE-MOF-based bilayer actuator using enhanced photothermal effect. The concept of active porogen may instigate more interests in developing porous LCE actuators.

To the best of our knowledge, this thesis is the first dedicated to developing the new class of porous LCE actuators and exploring their unusual actuation behaviors for applications. The methodologies and results, as well as the insights into the actuation mechanisms

reported in the thesis represent a significant contribution to the advancement of fundamental knowledge on LCE actuators. The strategy of making advanced LCE actuators with no need for designing and synthesizing new LCEs is of great interest and worth being pursued.

5.3 References

1. Zhan, Y., Broer, D. J., Liu, D. Perspiring Soft Robotics Skin Constituted by Dynamic Polarity-Switching Porous Liquid Crystal Membrane. *Adv. Mater.*, **2023**, *35* (12): e2211143.

2. Zhan, Y., Calierno, S., Peixoto, J., Mitzer, L., Broer, D. J., Liu, D. Light- and Field-Controlled Diffusion, Ejection, Flow and Collection of Liquid at a Nanoporous Liquid Crystal Membrane. *Angew. Chem. Int. Ed.*, **2022**, *61* (38): e202207468.

3. Gao, J., Tian, M., He, Y., Yi, H., Guo, J. Multidimensional-Encryption in Emissive Liquid Crystal Elastomers through Synergistic Usage of Photorewritable Fluorescent Patterning and Reconfigurable 3D Shaping. *Adv. Funct. Mater.*, **2022**, *32* (4):2107145.

4. Kotikian, A., Morales, J. M., Lu, A., Mueller, J., Davidson, Z. S., Boley, J. W.,Lewis, J. A. Innervated, Self-Sensing Liquid Crystal Elastomer Actuators with Closed Loop Control. *Adv. Mater.*, **2021**, *33* (27): e2101814.

5. Liao W, Yang Z. The Integration of Sensing and Actuating based on a Simple Design Fiber Actuator towards Intelligent Soft Robots. *Adv. Mater. Techno.*, **2021**, *7* (6): 2101260.

6. Zhao, L., Tian, H., Liu, H., Zhang, W., Zhao, F., Song, X., Shao, J. Bio-Inspired Soft-Rigid Hybrid Smart Artificial Muscle Based on Liquid Crystal Elastomer and Helical Metal Wire. *Small*, **2023**: e2206342.

7. Kim, H., Gibson, J., Maeng, J., Saed, M. O., Pimentel, K., Rihani, R. T.,Ware, T. H. Responsive, 3D Electronics Enabled by Liquid Crystal Elastomer Substrates. *ACS Appl. Mater. Interfaces*, **2019**, *11* (21): 19506-13.

8. Jiang, Z. C., Xiao, Y. Y., Cheng, R. D., Hou, J. B., Zhao, Y. Dynamic Liquid Crystalline Networks for Twisted Fiber and Spring Actuators Capable of Fast Light-Driven Movement with Enhanced Environment Adaptability. *Chem. Mater.*, **2021**, *33* (16): 6541-52.

9. Ford, M. J., Ambulo, C. P., Kent, T. A., Markvicka, E. J., Pan, C., Malen, J., Majidi, C. A Multifunctional Shape-morphing Elastomer with Liquid Metal Inclusions. *PNAS*, **2019**, *116* (43): 21438-44.

10. Goh, S. H., Lau, H. S., Yong, W. F. Metal-Organic Frameworks (MOFs)-Based Mixed Matrix Membranes (MMMs) for Gas Separation: A Review on Advanced Materials in Harsh Environmental Applications. *Small*. **2022**, *18* (20): e2107536.

11. Zhang, J., Guo, Y., Hu, W., Soon, R. H., Davidson, Z. S., Sitti, M. Liquid Crystal Elastomer-Based Magnetic Composite Films for Reconfigurable Shape-Morphing Soft Miniature Machines. *Adv. Mater.*, **2021**, *33* (8): e2006191.

12. Yang, Y., Zhan, W., Peng, R., He, C., Pang, X., Shi, D. Tao, J., Zhiqun, L. Graphene-Enabled Superior and Tunable Photomechanical Actuation in Liquid Crystalline Elastomer Nanocomposites. *Adv. Mater.*, **2015**, *27* (41): 6376-81.

APPENDIX A: Supporting Information (Chapter 2)

A.1 Supporting Information

Electronic Supporting Information

Porous Liquid Crystalline Networks with Hydrogel-Like Actuation and Reconfigurable Function

Jie Jiang,[a] Li Han,[ab] Feijie Ge,[a] Yaoyu Xiao,[a] Ruidong Cheng[a], Xia Tong,[a] Yue Zhao[a]*

Table of Contents

1. Experimental Procedure

1.1 Materials

4,4'-Dichloromethane (99%) was purchased from Fisher Scientific; p-coumaric acid (99%), 6-chlorohexanol (96%), phenylsuccinic acid (98%), $CaCO_3$ particles (size: ~0.8 μm and ≤ 50 μm), 1-Butyl-3-methylimidazolium tetrafluoroborate ($BMIMBF_4$, ≥98%), and 1,1,2,2-Tetraphenylethylene (98%) were purchased from Sigma Aldrich. Small size $CaCO_3$ nanoparticles (size: 15~40 nm, 97.5%) was purchased from SkySpring Nanomaterials, Inc.,

Vis523A was purchased QCR Solutions Corp. They were used directly without further purification.

1.2 Preparation of porous LCN actuators

The preparation of nonporous actuator, LCN-0, with uniaxially orientated mesogens consists in three steps. First, a film (180 μm in thickness) was obtained by compression-molding of the liquid crystalline polymer; secondly, it was uniaxially stretched in LC phase (53 ^{o}C) to 330% strain; thirdly, the stretched film was exposed to UV light on both sides for photocrosslinking. Based on this process, we selected an easy approach of direct templating for preparing the porous LCP actuators, using $CaCO_3$ as template. The multi-step process is as follows. $CaCO_3$ powders (average size 0.8 μm unless otherwise stated) with different contents (10 wt %, 20 wt %, 40 wt%) were dispersed in THF by an ultrasonator for 1 h. The solution was then added dropwise into a THF solution of the liquid crystalline polymer. After intense stirring for 12 h to prevent the aggregation of $CaCO_3$ powders, a homogenous viscous mixture was obtained. The solution was cast on a Teflon plate (PTFE) and put into an oven for quickly evaporating the solvent completely. Thin films (180 μm in thickness) of the polymer/$CaCO_3$ mixture were then obtained by hot compressing at 90 ^{o}C, followed by cooling to room temperature. To prepare the porous LCN actuators, the compressed films were cut into strips of 10 mm x 4 mm in length and width, respectively, which were then stretched at 51 ^{o}C in water to 40 mm x 2 mm x 80 μm, with the final strain at 330% after removal of external stress. The stretched films were first exposed to UV light (320-480 nm filter, 90 mW cm^{-2}) on both side (80 min for each side) for full and uniform crosslinking. Afterwards, the crosslinked films were soaked into an aqueous solution of hydrochloric acid (12 M) for 48 h in order to remove the $CaCO_3$ nanoparticles, and then rinsed by DI water for 10 min (unless otherwise stated), followed by drying in vacuum oven at 40 ^{o}C for 12 h.

1.3 Test of porosity

The porosity of films was tested through n-butanol uptake method and was calculated according to the following equation[1]:

$$porosity = \frac{M_{BuOH}/\rho_{BuOH}}{M_{BuOH}/\rho_{BuOH} + M_f/\rho_p}$$

Where M_{BuBOH} is the mass of the absorbed *n*-butanol by films, ρ_{BuBOH} is the density of n-butanol (0.81 g/cm^3), M_f is the mass of corresponding films, ρ_P is the overall density of used raw materials (1.1779 g/cm^3).

2. Characterizations

UV-Vis-NIR spectrometer (Varian) was used to measure the absorption spectra of the composite films from 190 nm to 1100 nm. Phase transition temperatures were determined by using a differential scanning calorimeter (DSC, TA) in the range of -20 to 120 ºC at a rate of 10 ºC min^{-1}, under protection of nitrogen flowing at 50 ml min^{-1}. Laser power was measured using a power meter (TURNER, gentec-co). Wide-angle X-ray scattering (WAXS) were performed on a Bruker AXS Nanostar system with a microfocus copper anode, MONTAL OPTICS and a VANTEC 2000 2D detector at 90 mm from the samples. The X-ray wavelength was 0.154 nm. Transmission FTIR spectra were recorded on a Nicolet Avatar 370 spectrometer with an infrared polarizer, with resolution 4 cm^{-1}. The surface and cross-sectional morphology as well as the measurements of energy-dispersive X-ray (EDX) and energy-dispersive spectroscopy (EDS) for LCN-40 subjected to different treatments were examined or recorded using a Hitachi S-4700 field-emission-gun scanning electron microscope (SEM) operating at 1-10 kV. Electrical resistance of porous LCN-40 containing ionic liquid were measured using a digital multimeter (RIGOL, DM3058E). Electrochemical Impedance Spectroscopy (EIS, Bio-Logic VMP-300) measurements were performed at open cell voltage, and frequency ranging from 1 Hz to 1 MHz.

3. Supporting Figures and Discussion

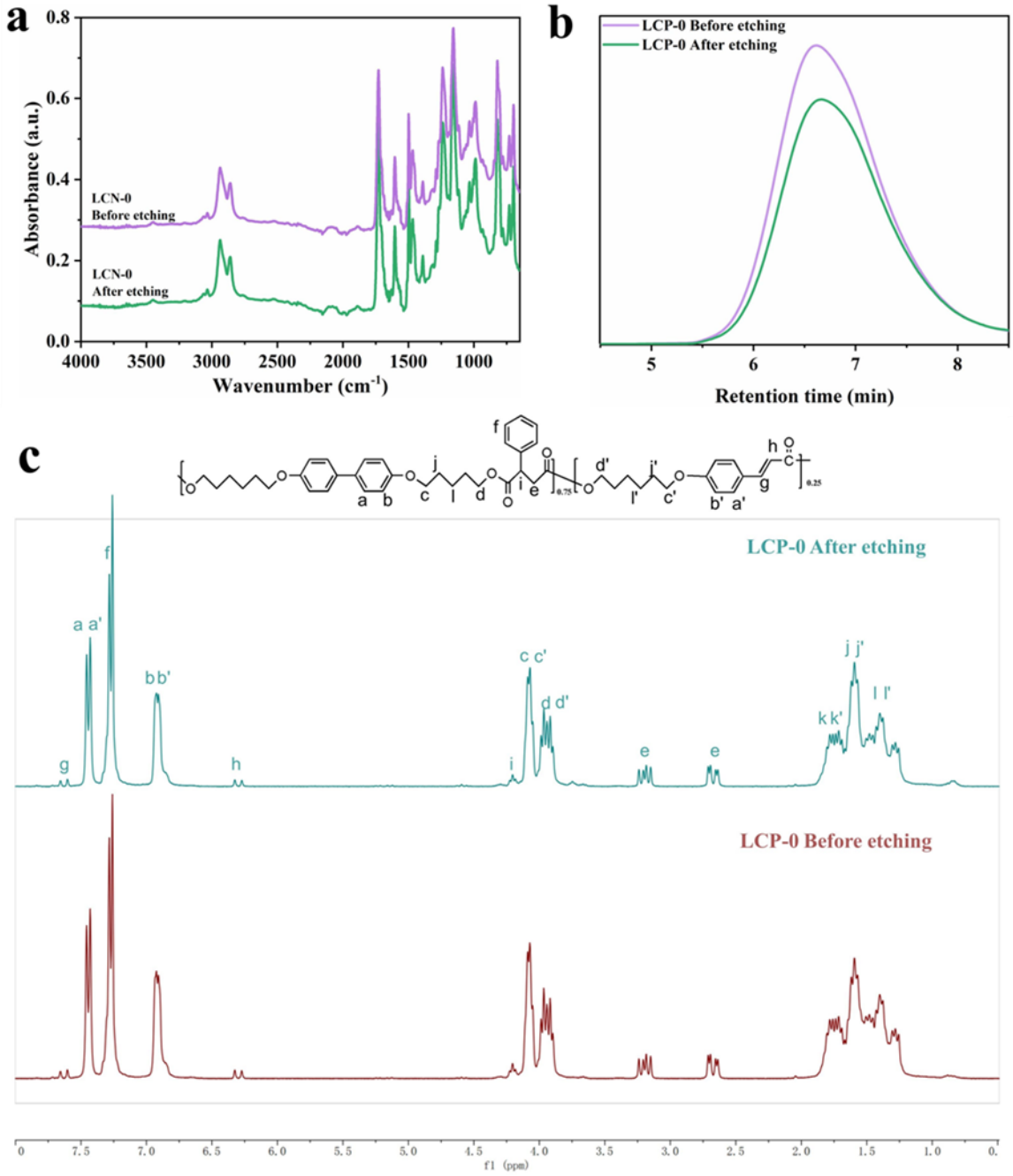

Figure S1. (a) FTIR-ATR spectra, (b) GPC traces, and (c) H^1 NMR spectra (in $CDCl_3$) for either liquid crystalline network (LCN-0) or non-crosslinked liquid crystalline polymer (LCP-0) before and after chemical etching using 12M HCl.

Comparing the results before and after etching, FTIR-ATR spectra show no new peak and no shift of the carboxylate peak; GPC traces show that the average molecular weights remain the (M_w: 53080 g/mol and M_n: 27690 g/mol); and H^1 NMR spectra show no changes neither.

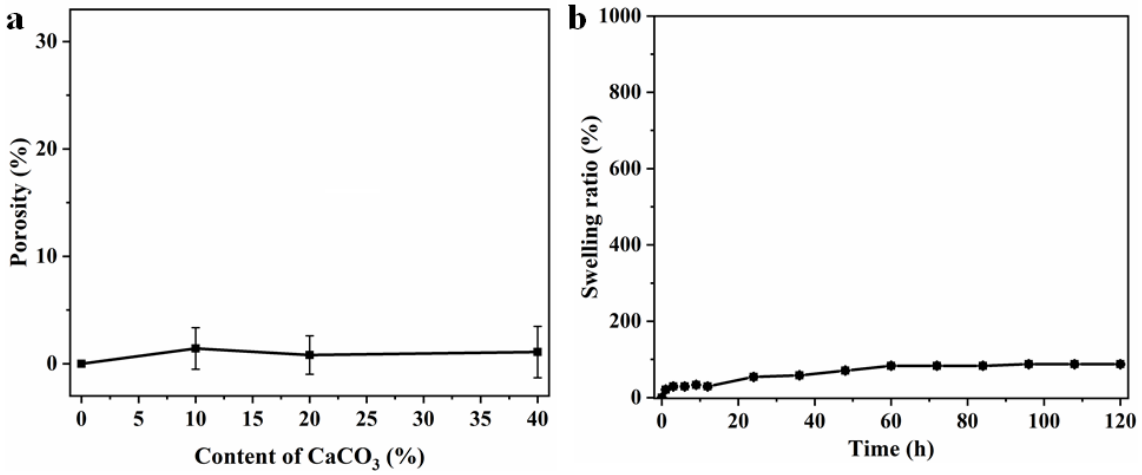

Figure S2. (a) Porosity of LCN films (etching before photocrosslinking) with different contents of $CaCO_3$, (b) LCN-40 prepared with etching before photocrosslinking.

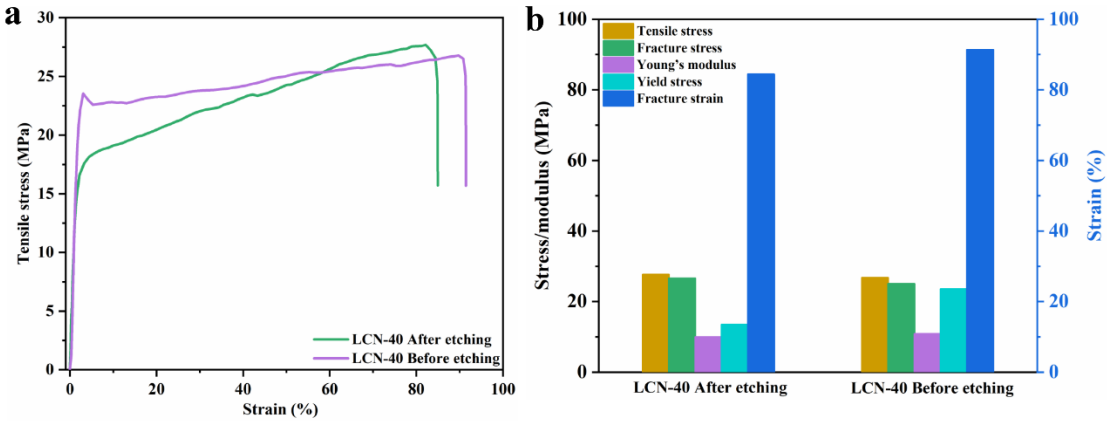

Figure S3. (a) Tensile stress and strain curves at room temperature and (b) mechanical properties of LCN-40 before and after chemical etching.

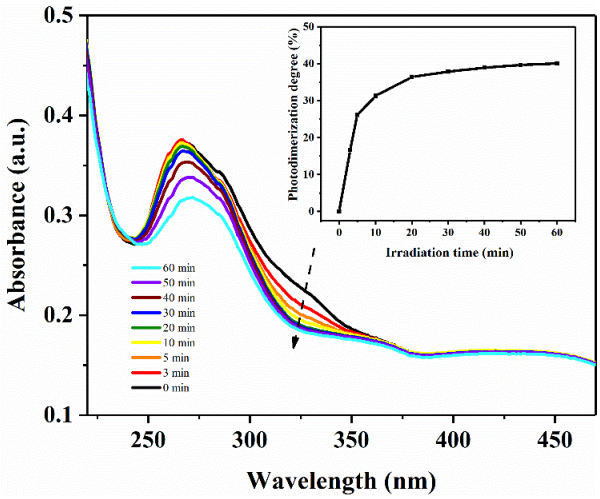

Figure S4. UV-Vis absorption spectra of LCN-40 films (thickness ca. 10 µm) spin-coated on quartz recorded after UV irradiation for different times for photocrosslinking. The UV light intensity was 90 mW cm^{-2} (inset: increase in photodimerization degree of cinnamyl groups from decrease in absorbance at 325 nm.)

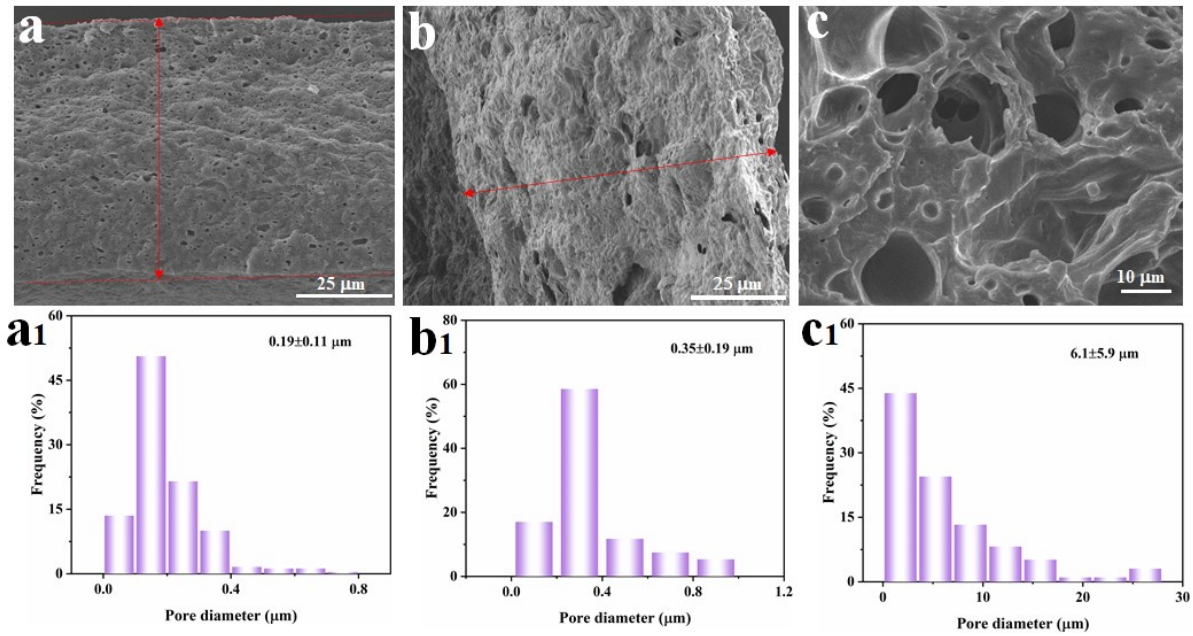

Figure S5. SEM observation and measurement: Cross-section image and distribution of pore sizes for LCN-40 samples prepared using $CaCO_3$ powders of different sizes (data

provided by supplier): (a) 15~40 nm, (b) 0.8 μm, and (c) ≤ 50 μm. The arrow indicates the thickness of the film. The results show that the average pore size in LCN-40 increases with increasing the size of $CaCO_3$ particles, but not in a proportional manner.

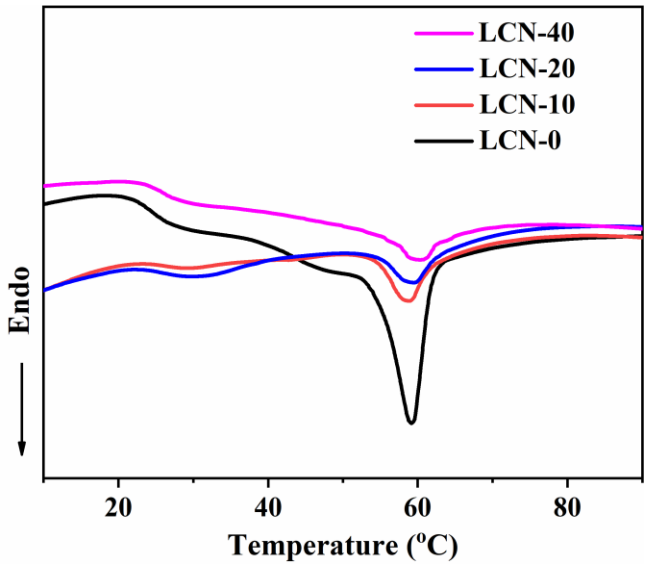

Figure S6. DSC traces (second heating) for porous and non-porous LCN samples. The characterization data of thermal phase transitions of the samples are summarized in Table S1.

Table S1. Thermal parameters of samples obtained from DSC measurement.

Sample	T_g (°C)	T_{NI} (°C)	$\triangle H_{NI}$ ($J\ g^{-1}$)
LCN-0	24	54.8	7.0
LCN-10	25	54.6	4.0
LCN-20	24	54.8	3.9
LCN-40	25	56.5	3.2

T_g: glass transition temperature; T_{NI}: nematic-isotropic phase transition temperature; $\triangle H_{NI}$: nematic-isotropic phase transition enthalpy.

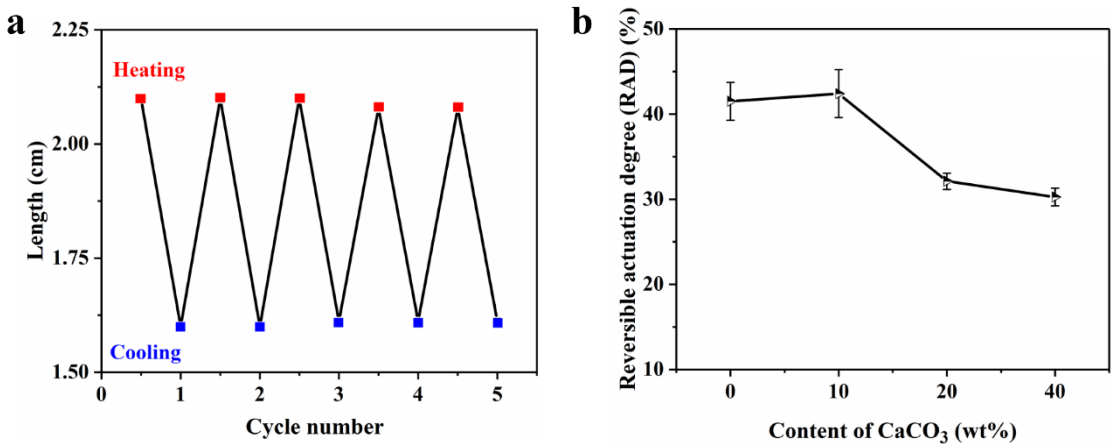

Figure S7. (a) Reversible change in the length of an LCN-40 strip upon order-disorder phase transition (heating temperature: 65 °C; cooling temperature: room temperature) (b) Reversible actuation degree of porous LCN actuator strip actuators. In all cases, the uniform crosslinked strip contracts upon heating into the isotropic phase and extends after cooling to the LC phase, which is characterized using the reversible actuation degree (RAD) defined as, $RAD=(L-L_0)/L_0 *100\%$, where L is length of strip in LC phase (room temperature) and L_0 the length of strip in isotropic state.

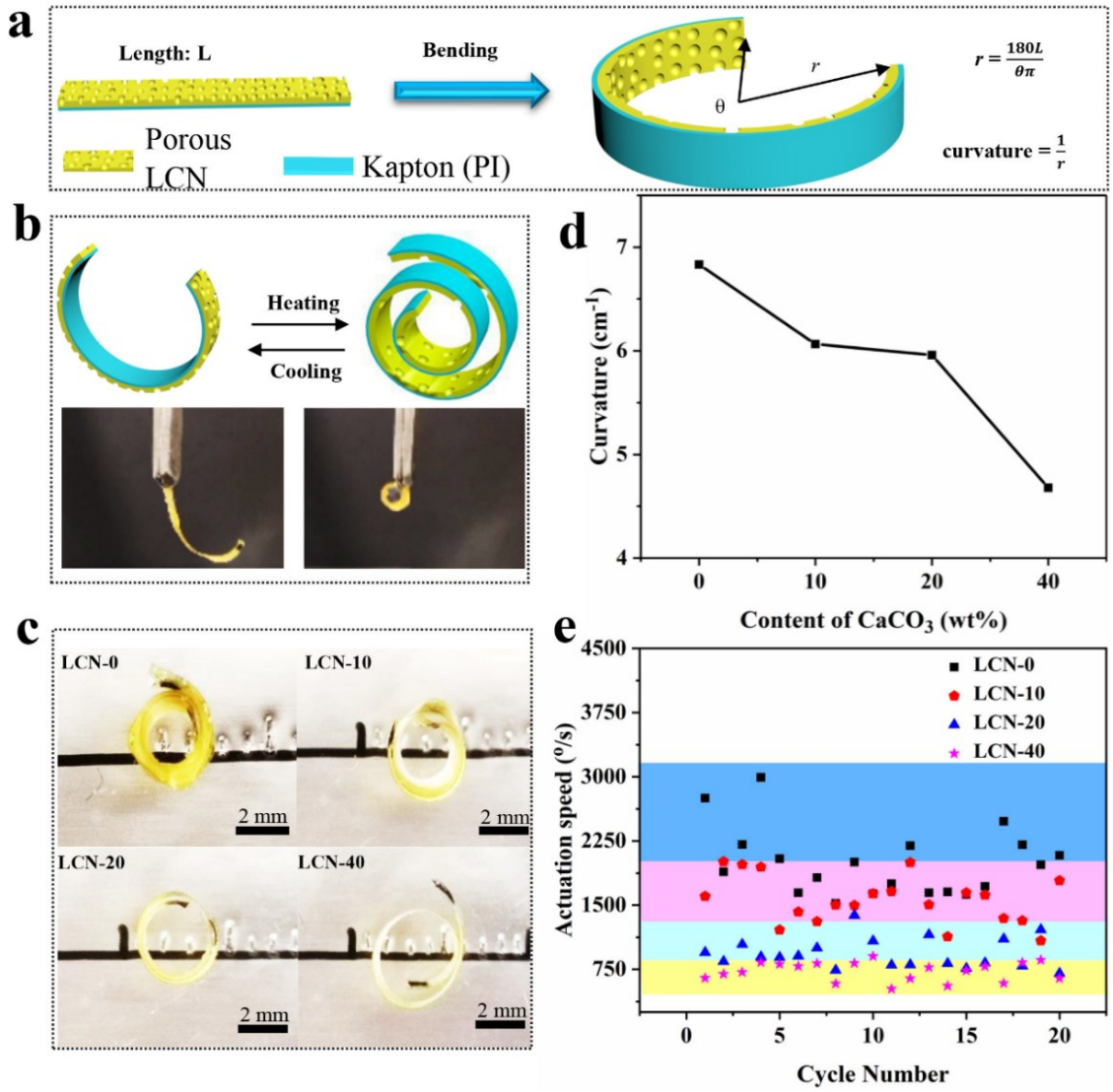

Figure S8. Actuation behaviors of bilayer actuator using porous LCN: (a) Schematic illustration for the characterization of the bending behavior (bending angle θ). (b) Schematic illustration of the reversible bending behavior of LCN-0, LCN-10, LCN-20, LCN-40. (c) Photos of the final bending states of LCN-0, LCN-10, LCN-20, LCN-40 at 65 ºC (scale bar is 2 mm). (d) Curvature of the LCN-0, LCN-10, LCN-20, LCN-40 at 65 ºC. (e) Actuation speed obtained for 20 cycles of bending for LCN-0, LCN-10, LCN-20, LCN-40.

Actuation behaviors of bilayer actuator using porous LCN were shown in Figure S8. Figure S8a shows a schematic illustration for the characterization of the bending behavior,

characterized by the bending angle (θ) and curvature. In order to obtain large deformation, the bilayer structure can be obtained for generating asymmetrical actuation behavior. The thermally stable Kapton (polyimide) film can be stuck on the side of porous LCNs films. In this case, the used strip has a size of 20 mm x 2 mm x 80 μm. Heating in hot water induces the contraction of the porous LCN layer and thus leads to the bending actuation of the bilayer towards the porous LCN side. After cooling down to room temperature (below T_{NI}), the extension of the LCNs layer caused the film to bend towards the opposite direction (the Kapton side) and generate a curled shape (Figure S8b, c). What's more, the curvature exhibits a decrease with increasing the number of pores due to a decrease of the order parameter and RAD (Figure S8d). Specifically, the actuation speed is defined as the change in angle when just entering the hot water to bend into the final shape divided by the time spent in this process. we defined the actuation speed for 20 cycles, showing that the superfast actuation speed of LCN-0, LCN-10, LCN-20, and LCN-40 is 1991.6 ± 395.1 °/s, 1561.2 ± 276.2 °/s, 934.5 ± 174.6 °/s and 726.9 ± 108.6 °/s, respectively (Figure S8e), which gradually decreases with an increase of porosity. Apart from this observation, it should be emphasized that the bilayer porous LCN films have a good reversible shape change when thermally triggered.

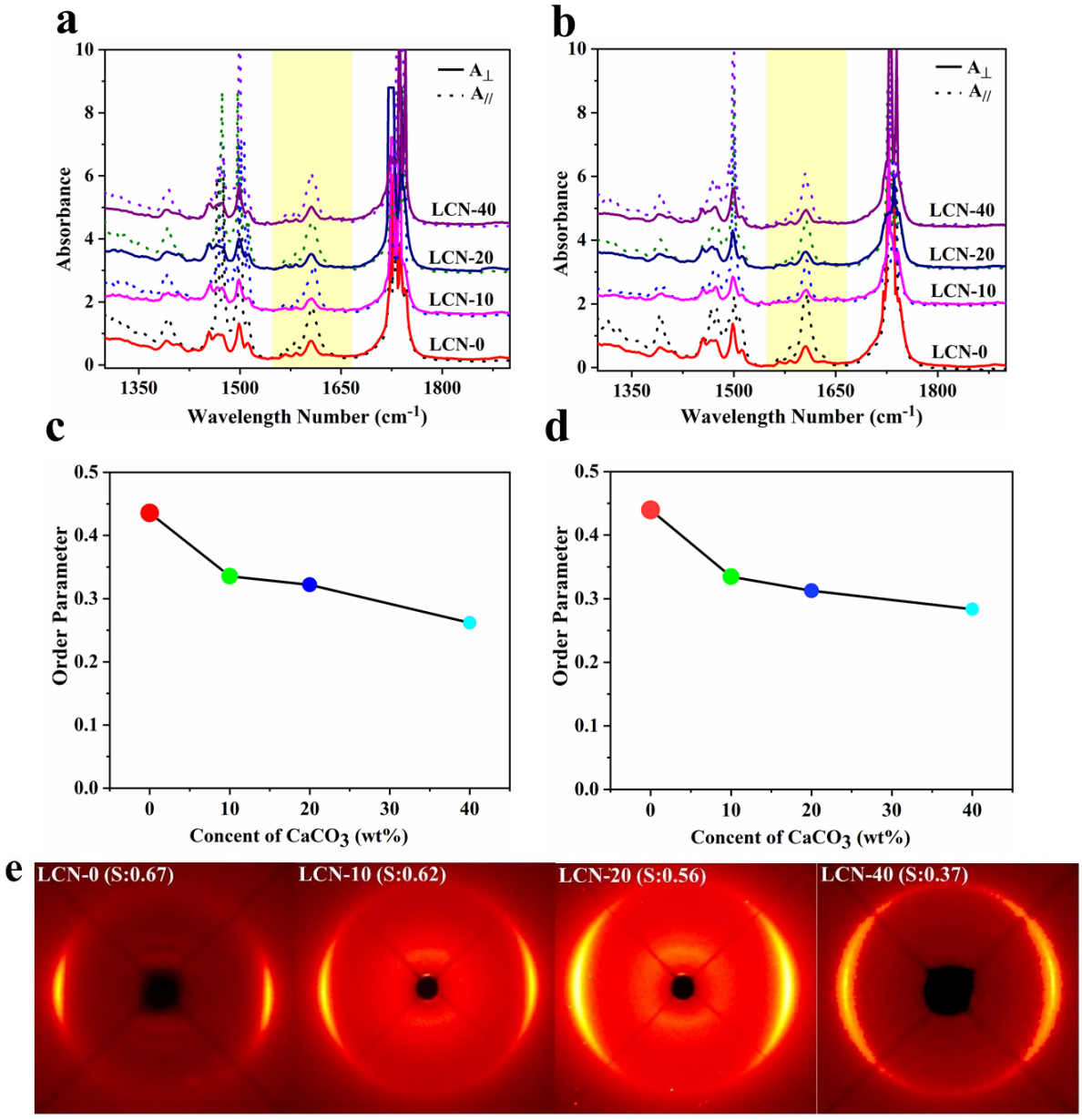

Figure S9. (a)-(d) Polarized infrared spectra and calculated order parameter of LCN samples with different contents of $CaCO_3$ before etching (a, c), and after etching (b, d). (e) 2D XRD patterns of LCN samples after etching (calculated order parameter shown in brackets).

The orientation of mesogens in the porous LCN films at 330% strain were measured using infrared dichroism. Figure S9 shows the polarized infrared spectra of the LCN films before

and after etching to remove $CaCO_3$. The parallel dichroism of the peak at around 1606 cm^{-1} (C=C bending vibrations of the biphenyl unit) indicates orientation of mesogens along the stretching direction. the order parameter S, which is a measure of the average orientation of all mesogens, can be calculated from the dichroic ratio R, according to $S = (R - 1)/(R + 2)$ with $R=A_{II}/A_{\perp}$, $A_{//}$ and $A_{\perp}$ being the measured absorbance with the infrared beam polarized parallel (0^0) and perpendicular (90^0) to the film stretching direction, respectively. Two observations can be made from the results in Figure S5. First, the chemical etching does not change the order parameter, meaning that this process does not disrupt crosslinked chains with oriented mesogens and that a shape change due to order-disorder phase transition could be retained. Secondly, the orientation of mesogens in porous LCN is smaller than in the nonporous LCN, but the decrease is relatively limited. And among the prepared porous LCNs, increase in porosity results in a slight decrease in order parameter. The results of infrared spectroscopy were confirmed by XRD measurements showing the same trend (Figure S9e). The apparently different order parameter values could be caused by the different sample preparation for the two techniques (films used for polarized infrared analysis are much thinner than those prepared for XRD).

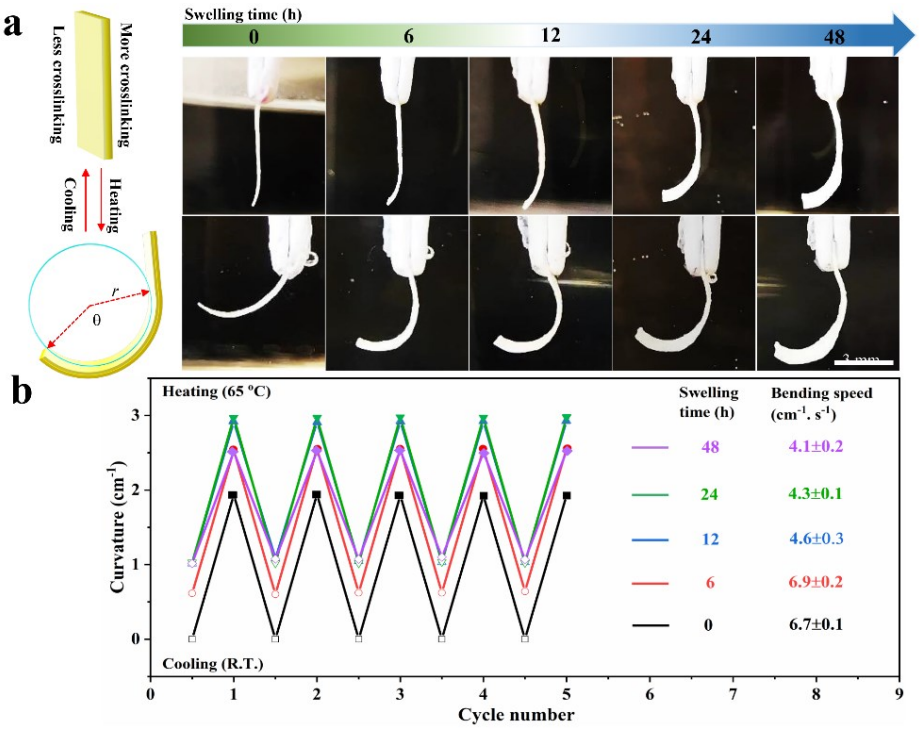

Figure S10. (a) Schematics and photos of a porous LCN-40 strip swollen in water for different times (for different amounts of absorbed water) upon heating to 65 °C followed by cooling to room temperature. The strip has asymmetrical crosslinking along the thickness direction (higher crosslinking degree on the right side), and its curling extent can be approximately measured by the curvature k of a traced circle with radius r. (b) Reversible shape changes as revealed by changes in curvature k=1/r (r=180*L/θ*π) for the LCN-40 strip containing various amounts of water upon four consecutive cycles of heating/cooling. The apparent bending speed is indicated.

The experiment in Figure S10 shows how thermally induced order-disorder transition in the hydrogel-like LCN could still lead to a macroscopic shape change and how the LCN-based actuation is affected by the presence of water. An LCN-40 film (10 mm x 1 mm x 80 μm) with asymmetrical photocrosslinking was prepared. The two sides of the film were exposed to UV light for 60 and 80 min, respectively, to impart different crosslinking densities. Figure S10a shows photos of the thermally induced reversible shape change

behaviors of this porous LCN actuator before and after absorption of different amounts of water. Prior to water absorption, the planar film bends towards the less crosslinked side when heated to the isotropic state (dipping in 65 ºC hot water for observation) due to an asymmetrical crosslinking effect[2], and unbends on cooling to room temperature (in air). After immersion in water for 6h, the strip is slightly bent as a result of asymmetrical swelling of the two sides. In preparing the porous LCN-40, the used photocrosslinking time, which determines the crosslinking density, affects the water swelling ratio. Indeed, as shown in Figure S11, the LCN-40 sample exposed to UV light for 80 min photocrosslinking absorbs more water than the sample photocrosslinked for 60 min. Upon heating to 65 ºC, the strip curls further towards the less crosslinked side, revealing the order-disorder transition induced shape change in the presence of water. By increasing the absorption of water in the porous LCN, the asymmetrical swelling induced bending of the film becomes more prominent, but the subsequent heating-cooling can still generate a reversible shape change, which is the manifestation of the order-disorder phase transition-based actuation of the hydrogel-like LCN actuator. As shown by the schematics in Figure S10a, from the photos, an approximate circle can be traced on the curled strip and a curvature k, which is the reciprocal of the circle's radius r ($r=180*L/\theta*\pi$), can be calculated for each sample before and after heating. Their reversible changes in curvature over four cycles of heating/cooling are plotted in Figure S10b. While the porous LCN strip before water absorption changes its shape only based on the order-disorder phase transition of the mesogens, the strips with different amounts of water change their shapes based on the interplay of volume variation due to water absorption like hydrogel and shape changing arising from order-disorder phase transition of mesogens like LCN. For all samples, when the strip was immersed in hot water (65 ºC), the bending was very fast, taking less than 1 second. From the video, the apparent bending speed of the porous LCN strip was also measured and the result, also shown in Figure S10b, indicates an effect of absorbed water on the actuation speed.

The bending speed becomes slower when the swelling time in water is 12 h or longer, corresponding to a swelling ratio range of about 100-200%.

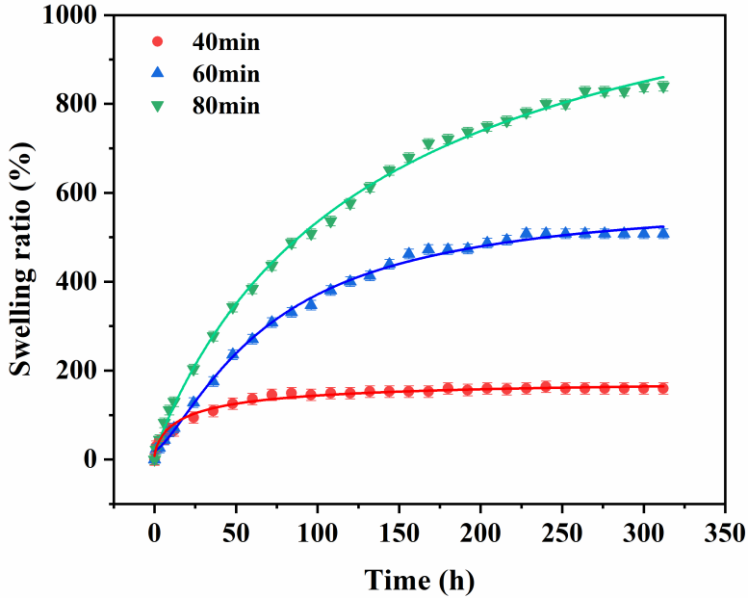

Figure S11. Swelling ratio of LCN-40 prepared using different UV light crosslinking times prior to etching (the times used in the experiments reported).

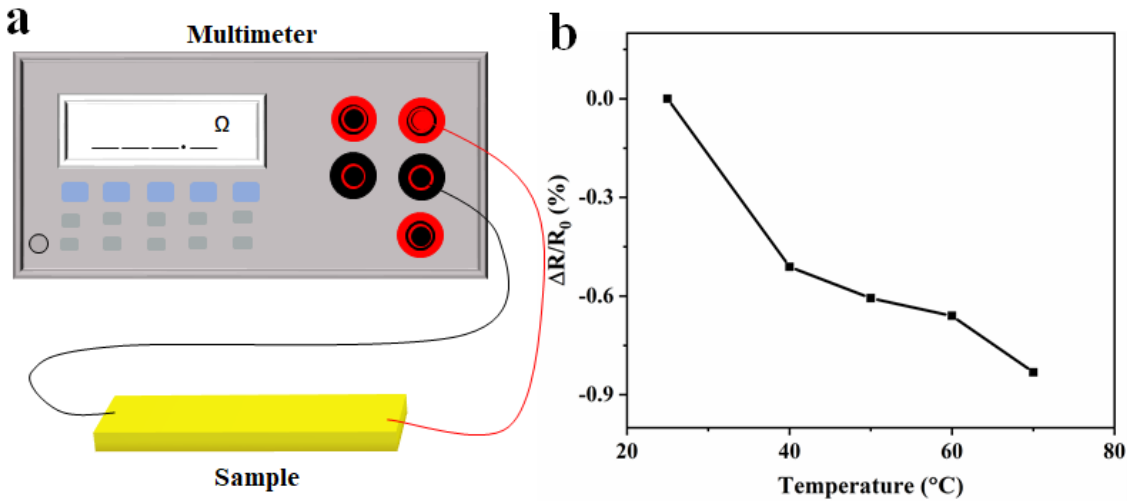

Figure S12. (a) Schematic of the setup used for the measurement of the conductivity of LCN strips. (b) Relative resistance changes of LCN-40-IL.

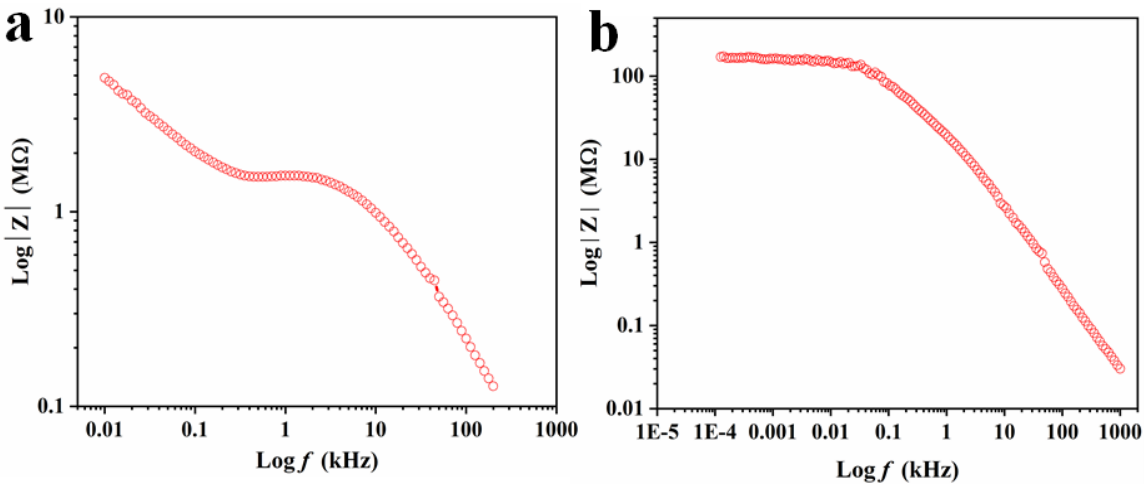

Figure S13. The typical Bode impedance plots of LCN-40-IL (a) and LCN-40 (b) measured for the impedance with varying different frequency. (|Z| mean the module value of impedance under different frequency)

The impedance of sample was measured by Electrochemical Impedance Spectroscopy (EIS) performed at open circuit potential between two metal electrodes. Figure S13 showing a typical Bode diagram, impedance measurement was executed to characterize the resistance of LCN-40-IL and LCN-40 under different frequency. It is clear that the impedance module value of LCN-40-IL is much smaller than that of LCN-40 without IL sample at both low and high frequency due to presence of IL.

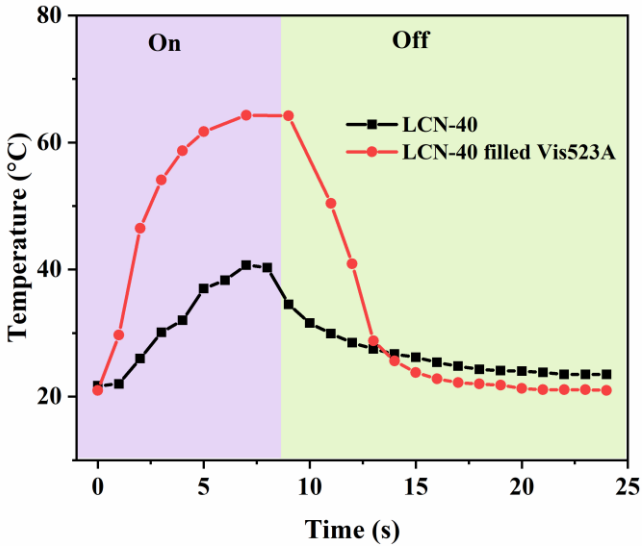

Figure S14. Temperature profile at light-on (532 nm, 616 mW/cm^2) and light-off of LCN-40 filled Vis523A and LCN-40 containing no dye. The filling of the photothermal dye is required for light-induced LC-isotropic phase transition.

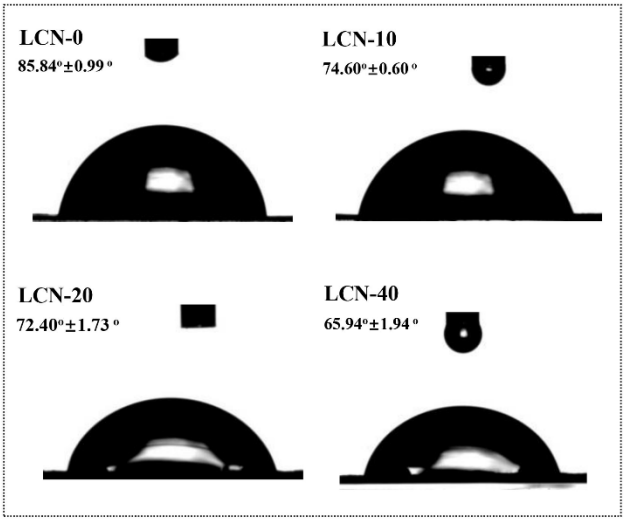

Figure S15. Photos showing the contact angle of water on films of LCN-0, LCN-10, LCN-20, and LCN-40.

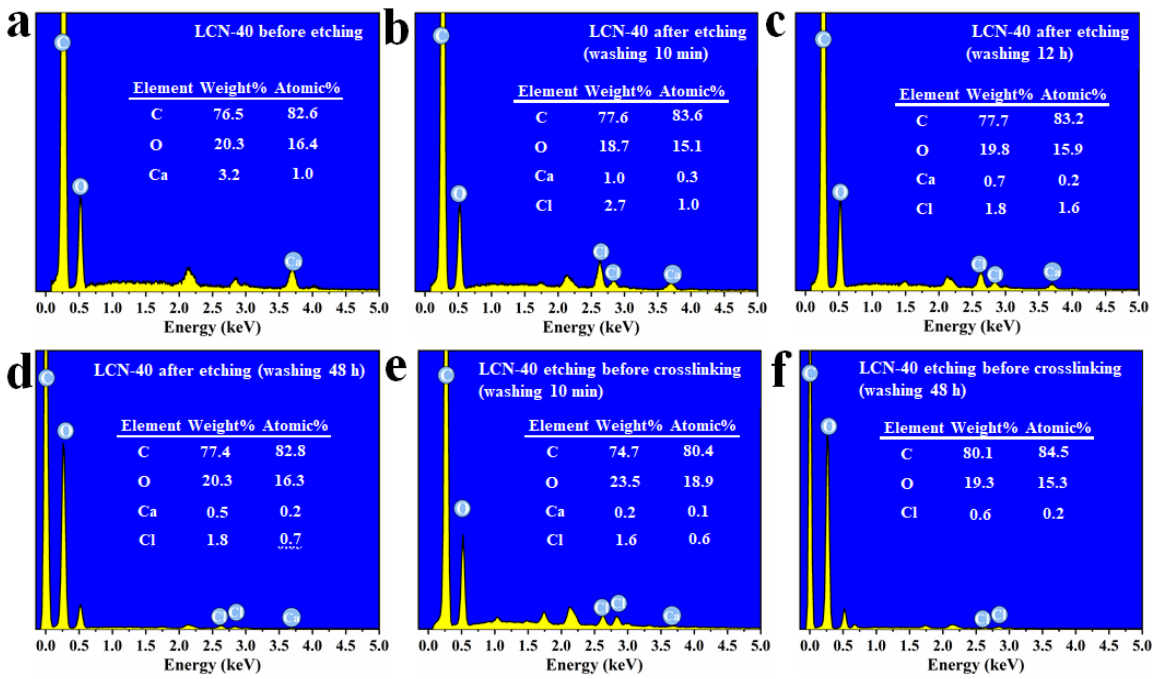

Figure S16. Energy-dispersive X-ray (EDX) spectra for: (a) LCN-40 before etching; (b-d) LCN-40 after etching followed by 10 min, 12h and 48h washing respectively; (e and f) LCN-40 prepared with etching before photocrosslinking, washed for 10 min and 48h, respectively.

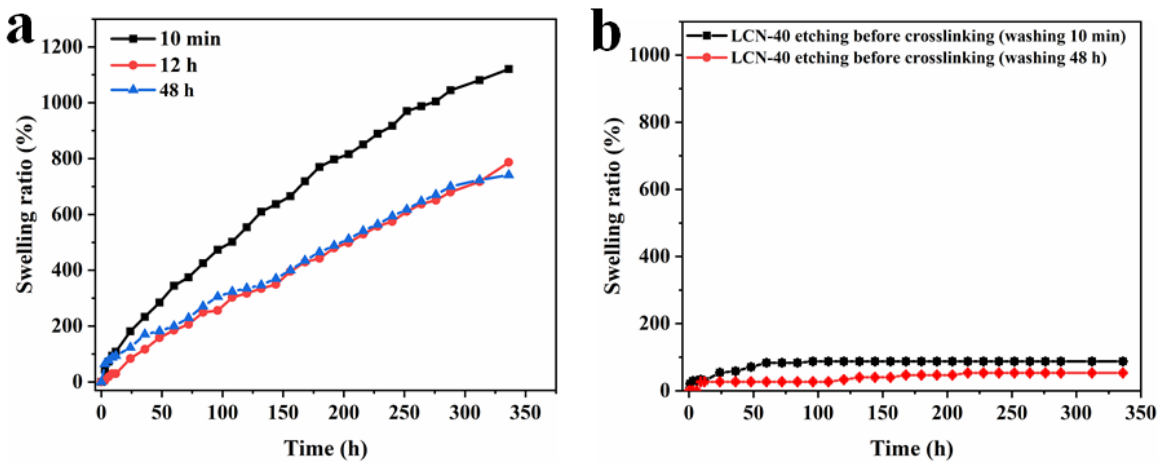

Figure S17. Swelling ratio vs. time (in water, at room temperature) for: (a) LCN-40 washed for different times (10 min, 12h and 48h) following etching. and (b) LCN-40 prepared with etching before photocrosslinking, washed for two different times (10 min and 48h).

A couple of observations can be made from Figures S16 and S17. First, from the spectra (a)-(d), which are for LCN-40 before etching, after etching with 10 min, 12h and extended 48h washing time, respectively. it is clear that the amount of Ca (II) present in the LCN-40 sample decreases after etching, and the drop is more prominent with a longer washing time (no significant decrease between 12h and 48h washing though). However, in the samples after washing, the Ca(II) residual is significant, just under a third of the initial amount (wt% or atomic%) with 10min washing and a quarter after 12h washing. At the same time, after etching, Cl appears from the used acid for etching (through diffusion into the sample during etching), longer washing time helps removing the ions, but a residual remains. Given that the LCN-40 sample subjected to 12h and 48h washing swells less, though still substantial, than the sample washed only for 10min (Figure S17a), the effect of remaining ions on the swelling of the porous LCN in water is clear. Secondly, for LCN-40 samples subjected to etching before photocrosslinking. It is no surprise to see less residual ions as compared to the sample crosslinked before etching (no Ca ions was detected after 48h washing), because crosslinked polymer chains make the removal of ions through diffusion more difficult. Nevertheless, the amounts of residual ions in the LCN-40 with etching before crosslinking are still quite significant. These two samples swell little in water (Figure S17b). The EDX results and the swelling behaviors of the corresponding samples shed light on the mechanism of water absorption by hydrophobic porous LCN actuators. Essentially, the absorption of water requires the existence of interconnected pore channels with large interfaces and an affinity (favorable intermolecular interactions) between pore surfaces and water molecules, while the presence of residual ions help increasing the affinity.

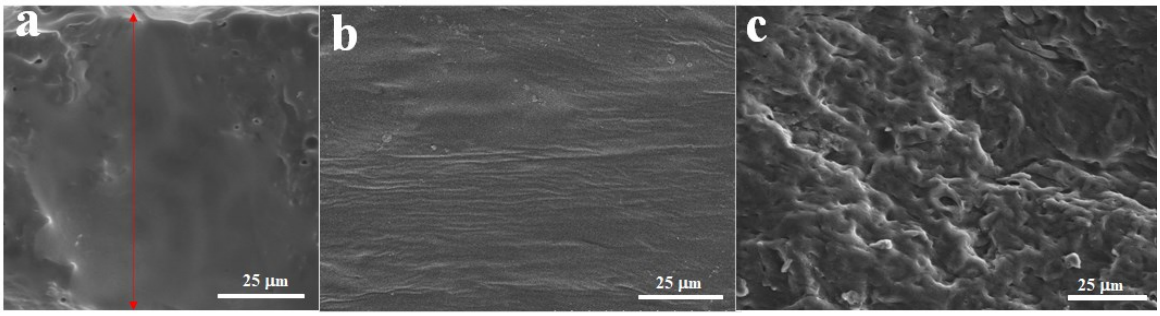

Figure S18. (a) and (b) SEM cross-section and surface image, respectively, for LCN-40 subjected to etching before crosslinking, showing basically absence of pores. (c) SEM surface image of porous LCN-40 (crosslinking before etching).

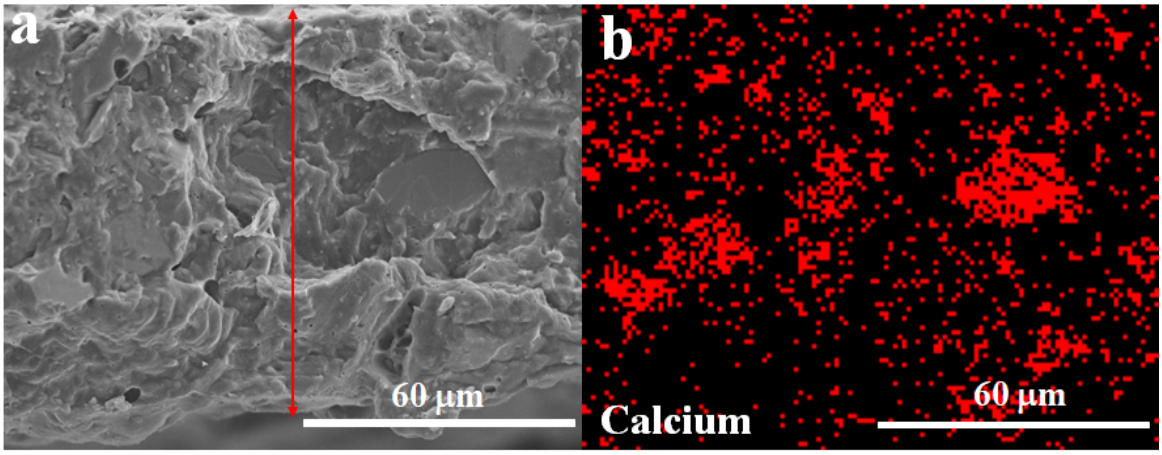

Figure S19. SEM-EDS cross-section image (a) and elemental mapping of Ca (b) for LCN-40 before etching. The arrow in (a) indicates the cross-section thickness.

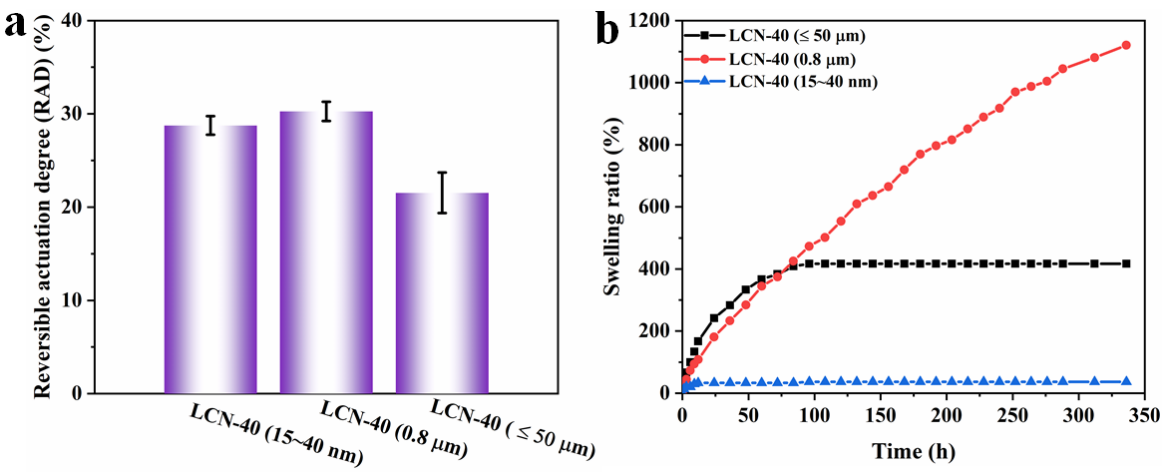

Figure S20. Effect of $CaCO_3$ particle size on reversible actuation degree (a) and swelling in water (b).

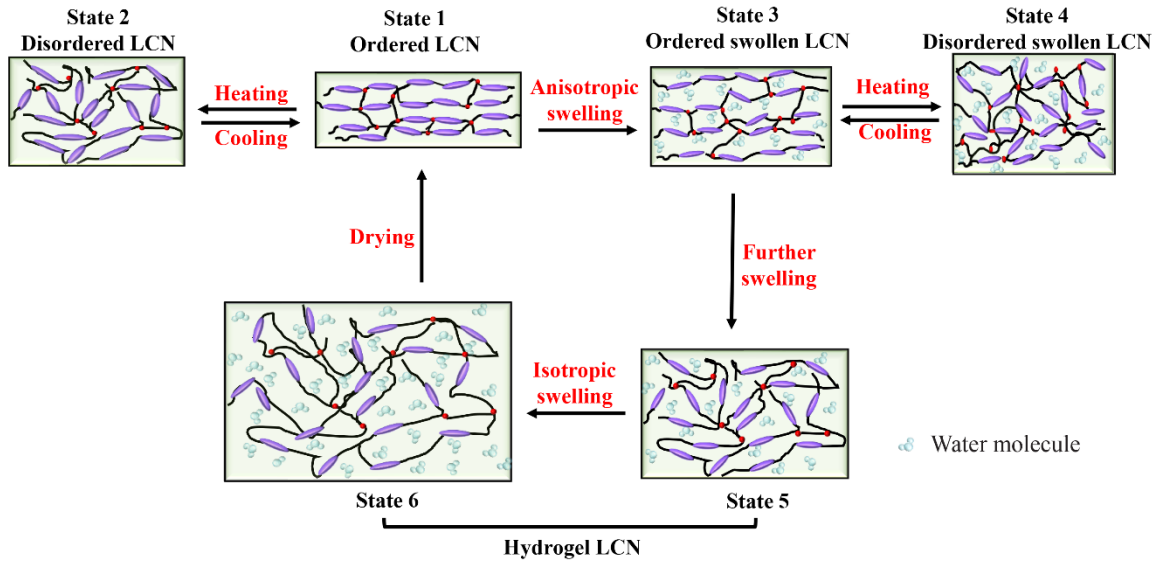

Figure S21. Schematic recapitulation of the shape changing features of porous LCN actuator that combines the mechanisms of both thermally induced reversible order-disorder phase transition of mesogens and water absorption induced reversible shape change including anisotropic and isotropic swelling.

LCN- and hydrogel-based actuators display shape change through order-disorder phase transition and water absorption, respectively. Thanks to the hydrogel-like swelling, porous LCN actuator can act by means of the two mechanisms. This interesting feature is schematically recapitulated in Figure S21. First, without water absorption, porous LCN basically behaves like non-porous LCN (between state 1 and state 2). It can change shape reversibly upon LC-isotropic phase transition by heating and cooling (Figure S7a). Secondly, when immersed in water, porous LCN swells anisotropically in the early stage of water absorption (between state 1 and state 3). While permeating the polymer, water molecules can more easily overtake the weaker intermolecular interactions in the direction perpendicular to the oriented mesogens and chain backbone (*i.e.* van der Waals and π-π stacking), leading to expansion in width and contraction in length. In the anisotropic swelling stage, since a substantial degree of orientation of mesogens remains, the swollen porous LCN actuator can undergo reversible shape change associated with order-disorder phase transition (between state 3 and state 4). In other words, both actuation mechanisms of phase transition and water absorption are effective. While upon further swelling as water absorption goes on, aligned mesogens and chain backbone increasingly relax, resulting in a transition from ordered to disordered state (state 3 to state 5). Beyond this point, the isotropic porous LCN undergoes isotropic swelling in water, giving rise to a similar expansion in all directions, as revealed by the essentially constant length to width aspect ratio (state 5 to state 6). In this isotropic swelling stage, the shape change is only governed by the amount of absorbed water like hydrogel. Finally, after evaporation of water, the porous LCN returns to the original state by recovering the macroscopic orientation of mesogens (state 6 to state 1) (Figure S22). Altogether, the porous LCN behaves like a new kind of actuator whose shape change can be triggered by either order-disorder phase transition like LCN or water absorption like hydrogel.

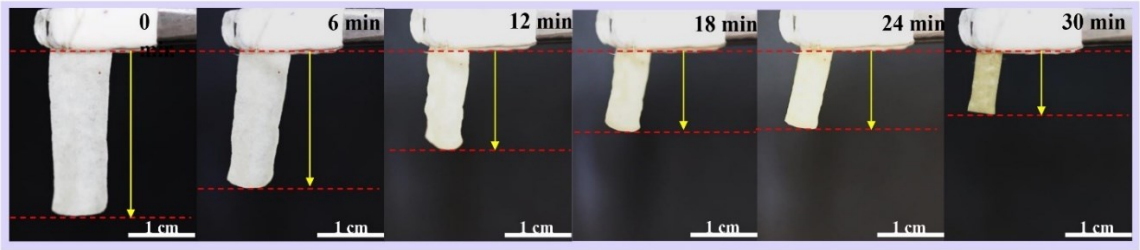

Figure S22. Photos showing the shrinking of a swollen LCN-40 over drying time (the oven temperature is 60 °C).

4. Supporting Movie Captions

Movie S1. Swollen tube upon heating to 65 °C.

Movie S2. Light-induced movement of a microwalker through cycles of arching-up (light-on) and flattening-down (light-off) (light intensity: 616 $mW.cm^{-2}$).

5. Supporting References

[1] X. Yu, Y. Li, Yin, X. Yin, X. Wang, Y. Han, Y. Si, B. Ding, *ACS Appl. Mater. Interfaces* **2019**, *11*, 39324-39333.

[2] Y. Y. Xiao, Z. C. Jiang, J. B. Hou, Y. Zhao, *Nat. Commun.* **2021**, *12*, 624.

(Download at: https://doi.org/10.1002/anie.202116689)

APPENDIX B: Supporting Information (Chapter 3)

B.1 Supporting Information

Electronic Supporting Information

Liquid crystalline elastomer for separate or collective sensing and actuation functions

*Jie Jiang, Yue Zhao**

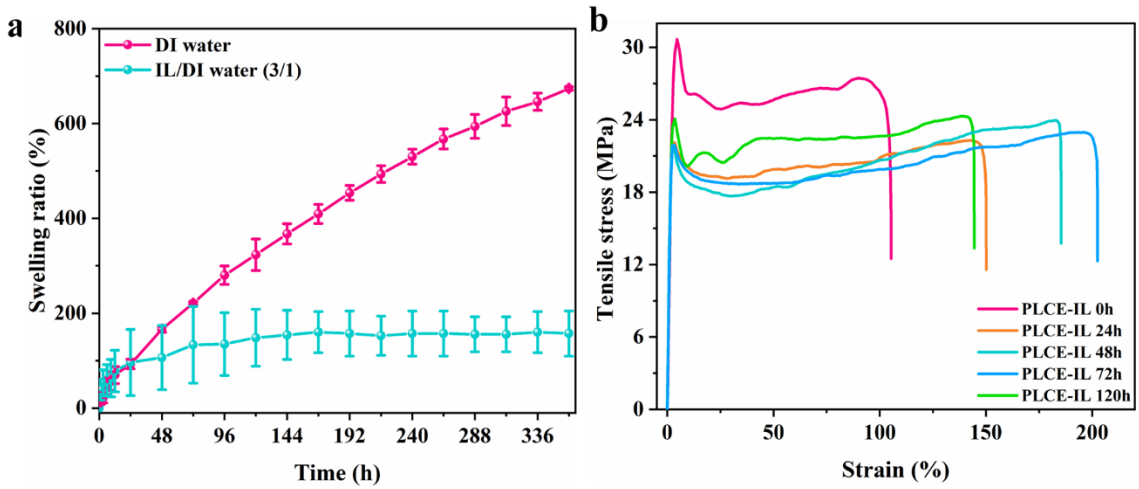

Figure S1. (a) Swelling ration vs. time for porous LCE films immersed in DI water and IL/DI water (3/1) at room temperature. (b) Tensile stress-strain curves at room temperature for PLCE-IL prepared with different soaking time (different IL contents).

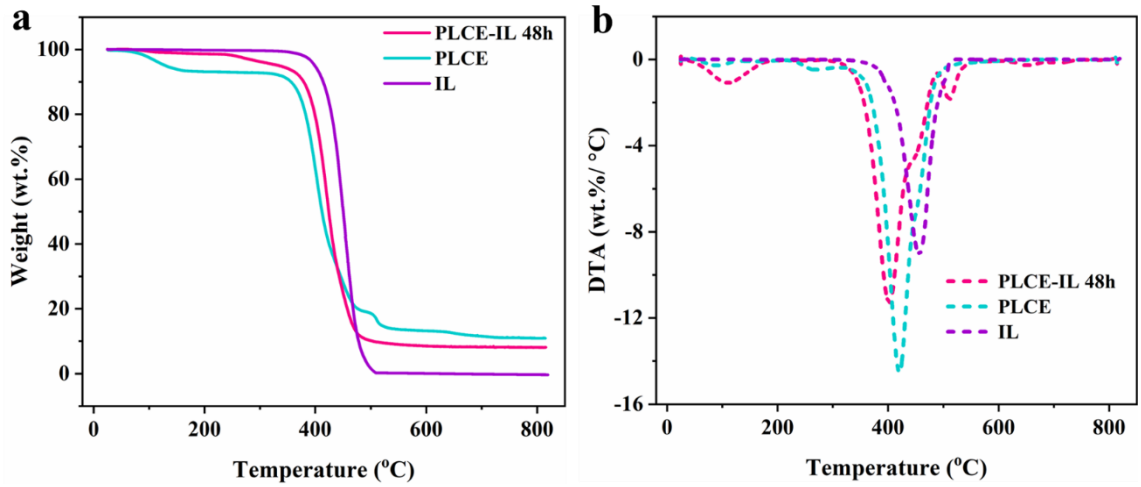

Figure S2. TGA curves (a) and DTA (b) for PLCE-IL, PLCE, and IL.

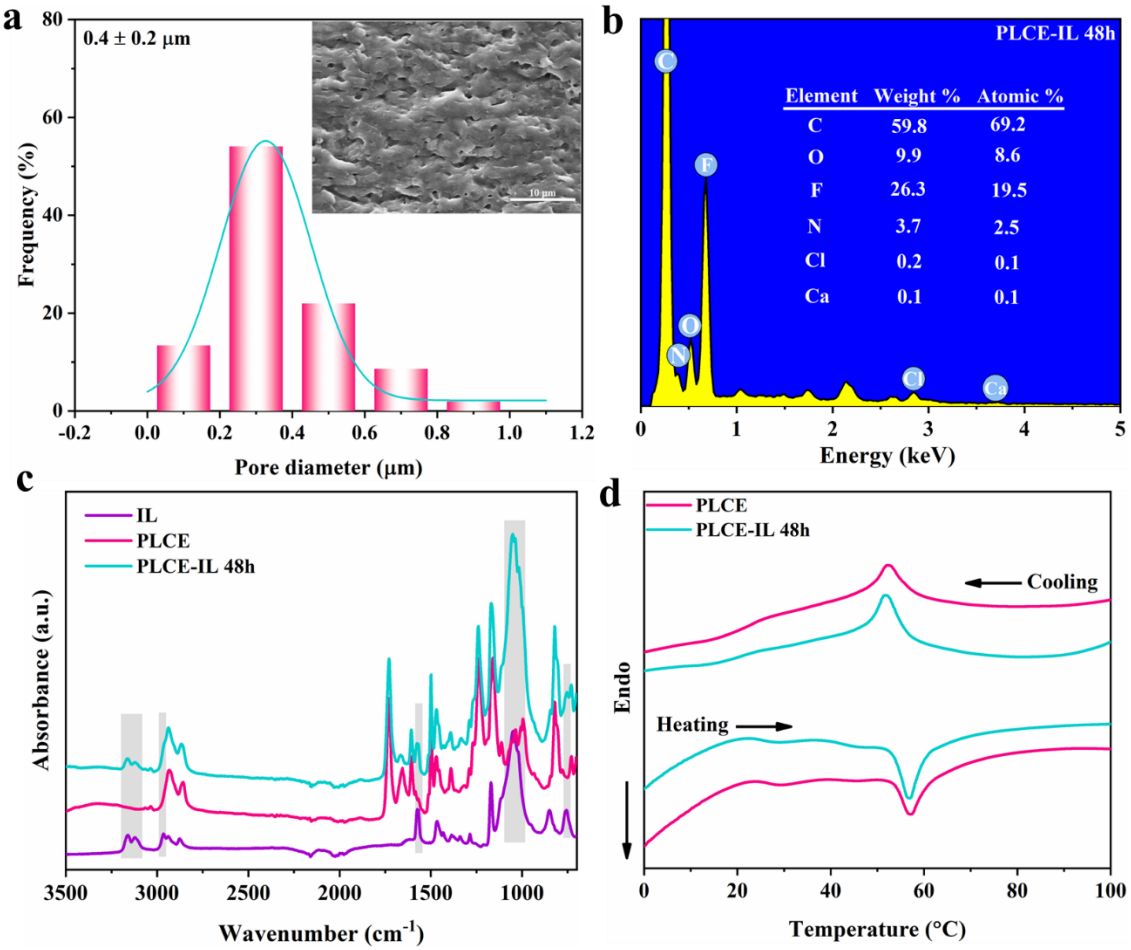

Figure S3. (a) The distribution of pore diameters of PLCE sample, measured using the inset SEM image. (b) Energy-dispersive X-ray (EDX) spectra for PLCE-IL after soaking 48h. (c) ATR-FTIR spectra of IL, PLCE, and PLCE-IL 48h (highlighted characteristic peaks of IL appear). (d) DSC traces of cooling (first scan) and heating (second scan) of PLCE-IL 48h and PLCE.

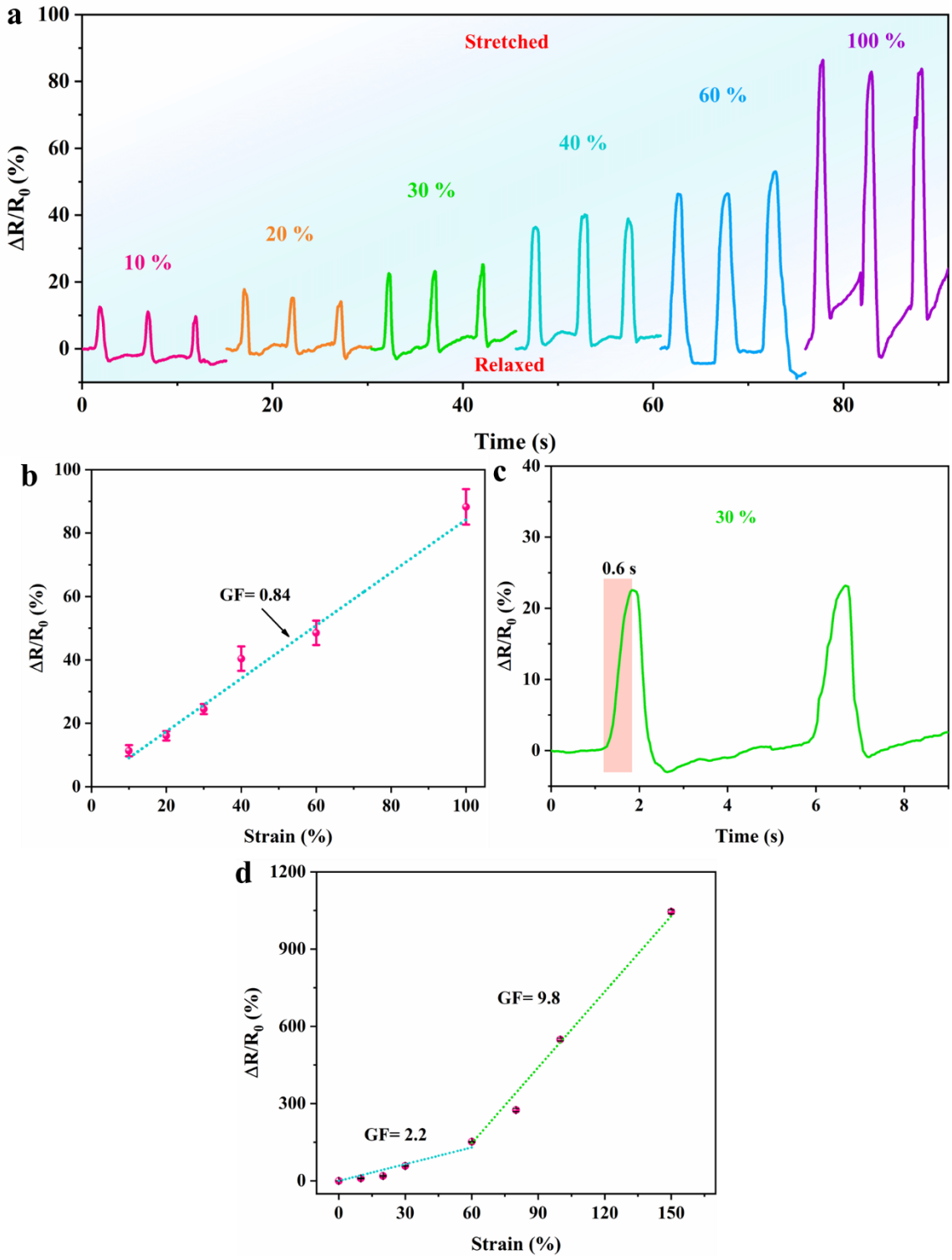

Figure S4. PLCE-IL film subjected to cyclic stretching/relaxation at 45 ºC: (a) Relative resistance variation in response to different strains. (b) Peak values in (a) plotted as a

function of strain, the slope of the linear fitting is the gauge factor (GF) defined as the ratio of relative change in resistance to that in strain. (c) Relative resistance rises and drops in response to strain (30%) and relaxation of the film. (d) The plot of plateau resistance changes in Figure 2b as function of strain, with the linear fitting used to measure the gauge factor (GF).

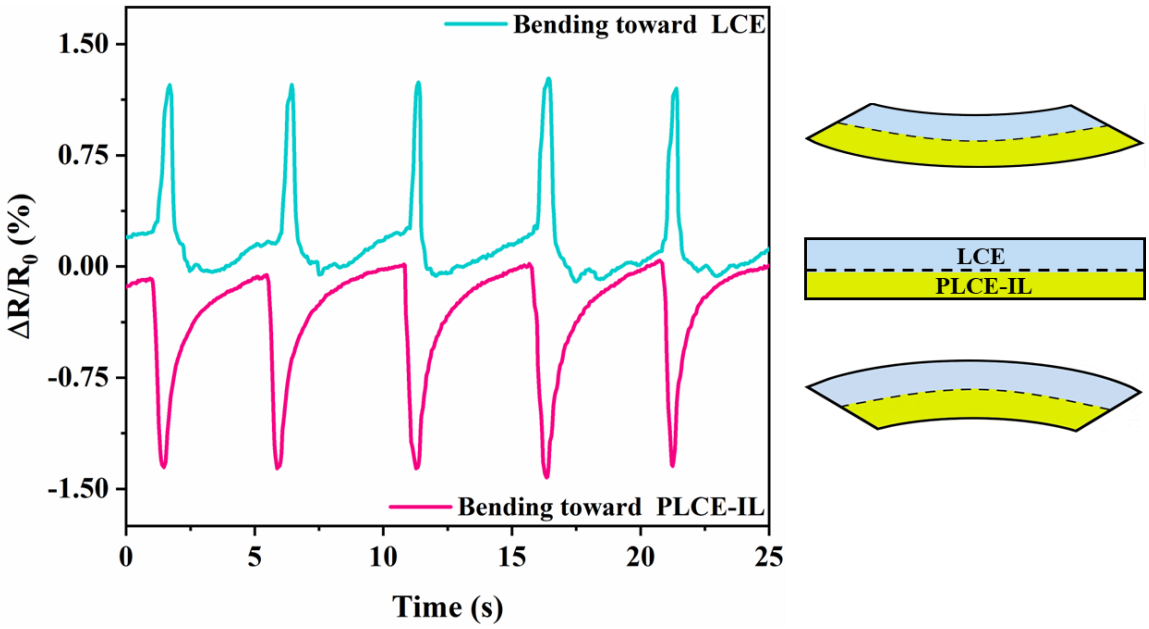

Figure S5. Relative resistance changes of a PLCE-IL/LCE bilayer upon bending towards the two sides at 90º angle (see schematics). The two films of PLCE-IL and LCE used for to the bilayer have the same size: 1.5 cm × 2 mm × 40 μm.

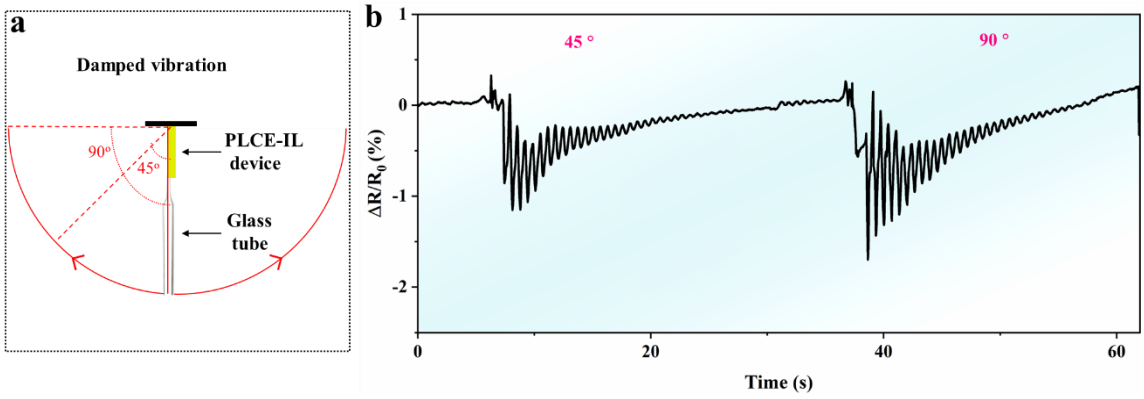

Figure S6. (a) Schematics showing the setup for damped vibration testing. (b) Relative resistance changes of PLCE-IL sensor when vibrating with different releasing angles (45° and 90°). (Description of testing setup: one end of PLCE-IL sensor device clamped by laboratory tweezers and fixed it, and another free end of device attached with glass tube was released at different angles 45° and 90°.)

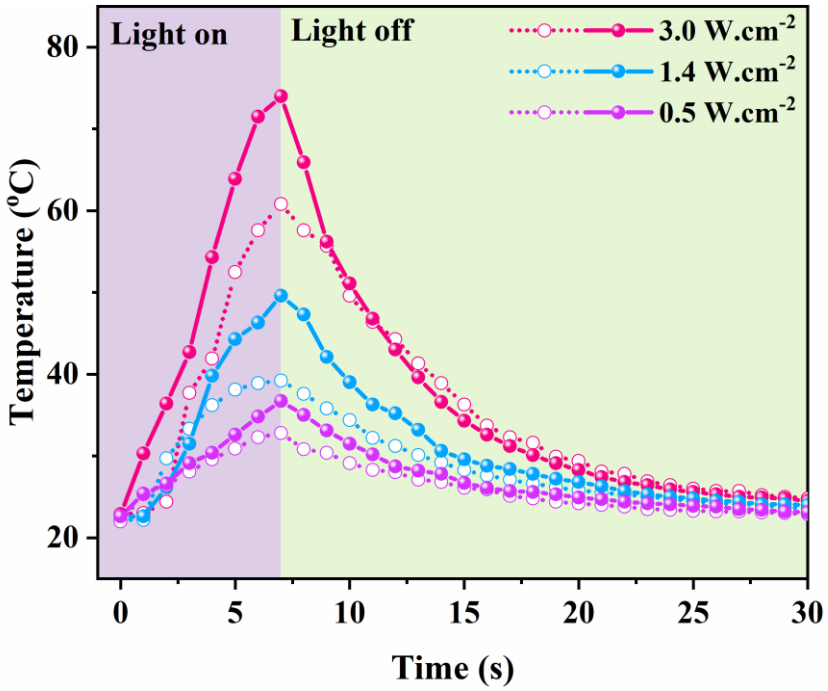

Figure S7. Temperature profile of heating under light irradiation of different intensities and cooling without light for PLCE-IL films with ink painted on surface (solid symbols and lines) and for the same PLCE-IL films without ink painting (open symbols and dotted lines).

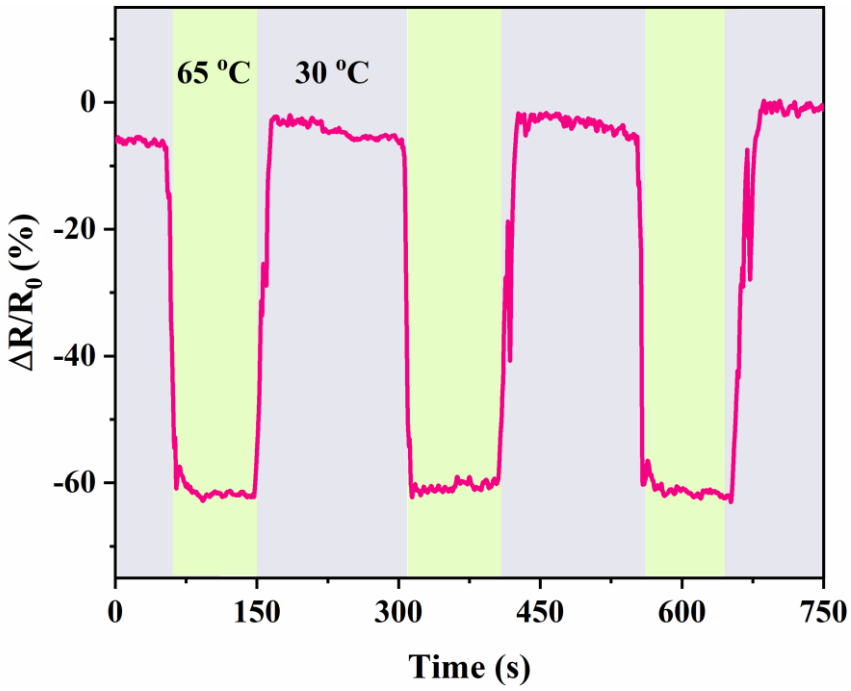

Figure S8. The reversible relative resistance variation of PLCE-IL strip upon cyclic heating (65 ºC) and cooling (30 ºC).

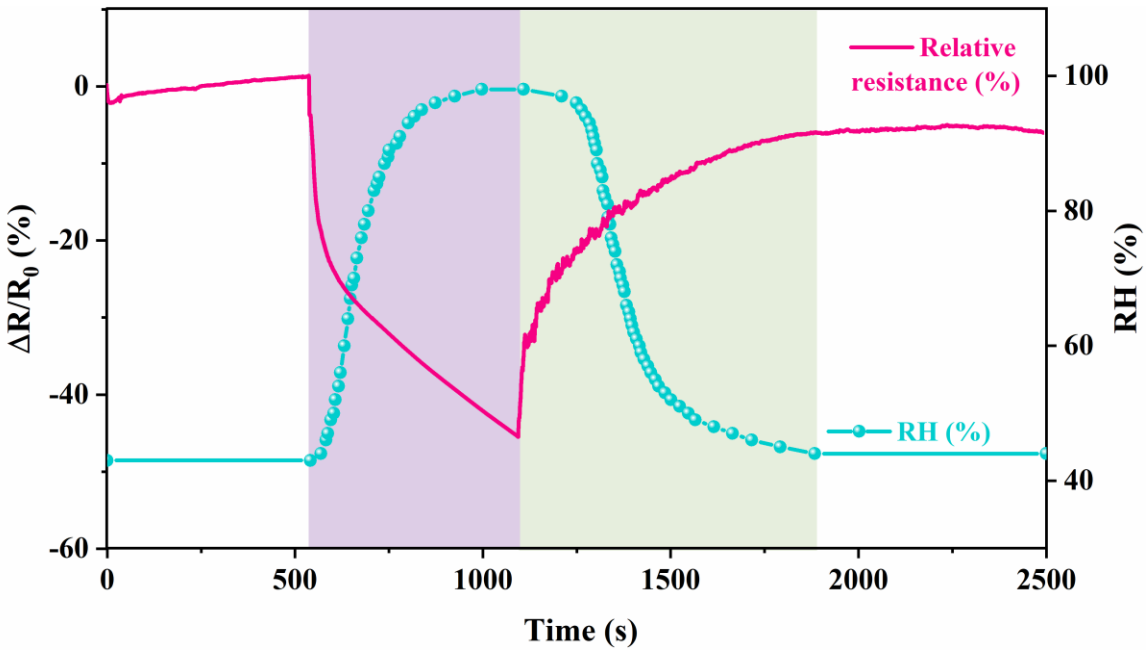

Figure S9. Relative resistance changes of PLCE-IL in response to changing relative humidity (ranging from 43% to 98%) at room temperature.

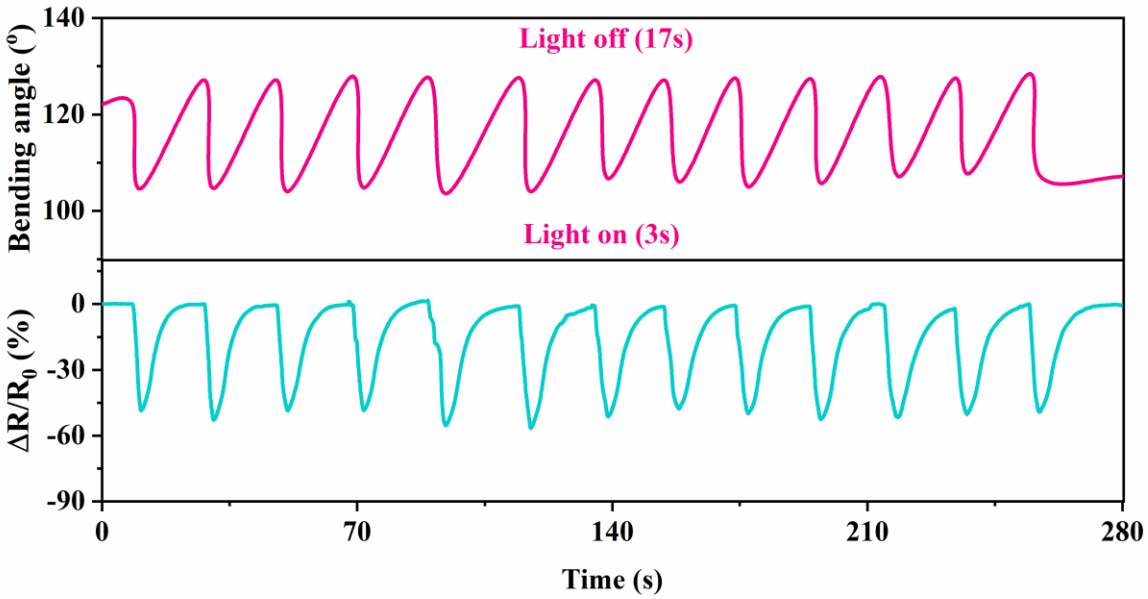

Figure S10. Elbow bending angle switch and relative resistance changes of PLCE-IL strip upon light-on (3 s) and light-off (17 s) cycles (light intensity: 3 W/cm^2).

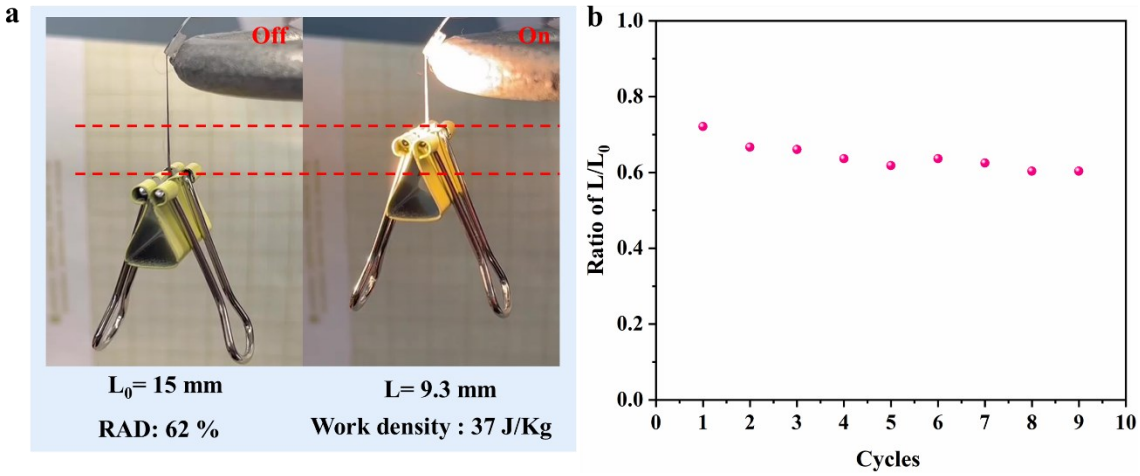

Figure S11. (a) Photograph showing the light driven weight lifting of an PLCE-IL strip (actuator weight: 2.3 mg; weight of the clip: 2877.7 mg); the lift height corresponds to a

reversible actuation degree (RAD) of about 62%. (b) The L/L_0 length ratio of the PLCE-IL strip under nine consecutive light on and off cycles.

Supporting movie captions

Movie S1. Light-driven locomotion of a PLCE-IL based walker crawling on the two different surrounding temperatures (21 and 38 ºC) upon cyclic light on/off (light intensity: 3 $W.cm^{-2}$)**.**

Movie S2. A PLCE-IL based weight-lifting artificial arm undergoes a bending and unbending movement powered by cyclic light on/off (light intensity: 3 $W.cm^{-2}$).

(Download at: DOI 10.1002/smll.202301932)

APPENDIX C: Supporting Information (Chapter 4)

C.1 Supporting Information

A Porous Multi-stimuli Responsive Liquid Crystal Elastomer Actuator Enabled by MOF Loading: Water uptake, Magnet-Guided Navigation, and Light-Driven Locomotion

*Jie Jiang, Yaru Ma, Ruidong Cheng, Yue Zhao**

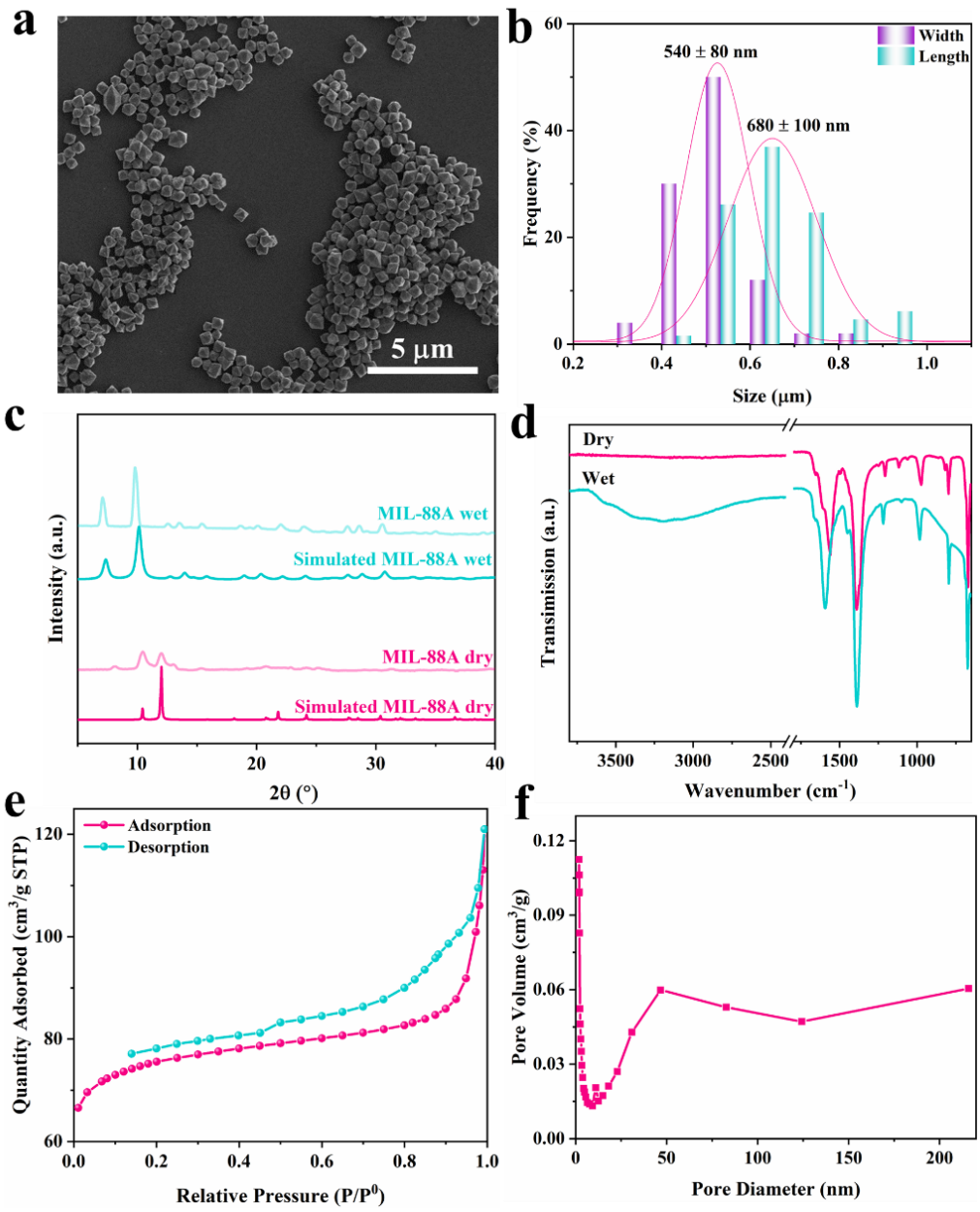

Figure S1. (a) SEM images of MIL-88A crystals showing elongated hexagonal bipyramidal shape. (b) Size distribution in length and width of MIL-88A crystal as revealed from SEM images. (c) XRPD diffractograms of MIL-88A powder after drying at 120 °C (red) and after immersion in water (blue), compared with the simulated patterns from the single-crystal diffraction of MIL-88A. (d) FT-IR spectra of dry and wet MIL-88A. (e) N_2

adsorption-desorption isothermal of the MIL-88A at 77 K. (f) Pore size distribution of MIL-88A crystals.

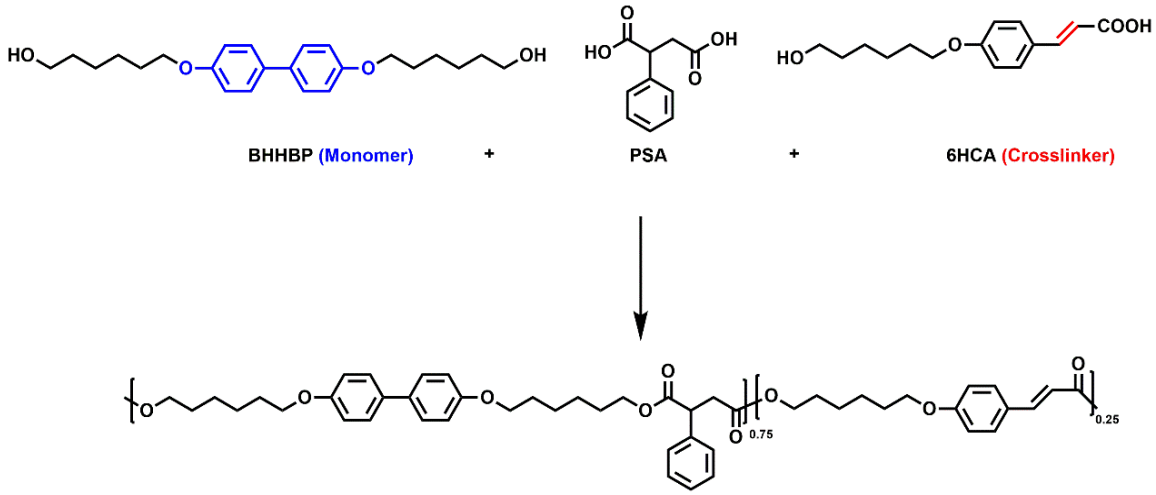

Figure S2. Synthesis of the used main-chain liquid crystal polymer.

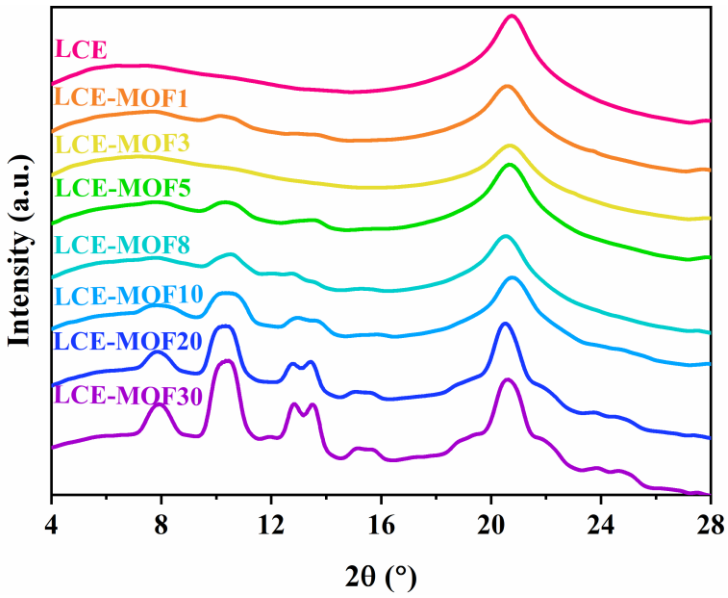

Figure S3. 1D-XRD diffractograms of MOF-loaded LCE with different MIL-88A contents (wt.% indicated by the number in the acronym).

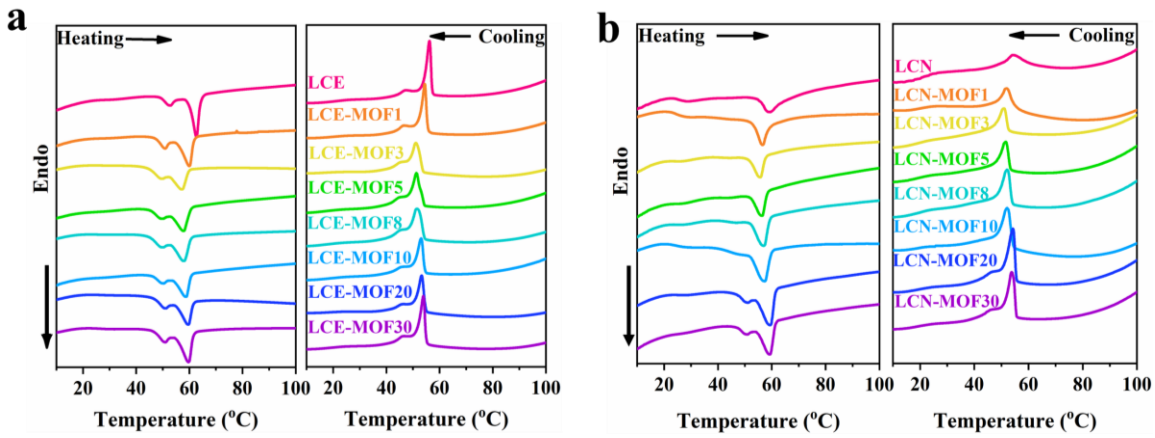

Figure S4. DSC scans (seconding heating and first cooling) for LCE-MOF with different amounts of MIL-88A particles before (a) and after photo-crosslinking (b).

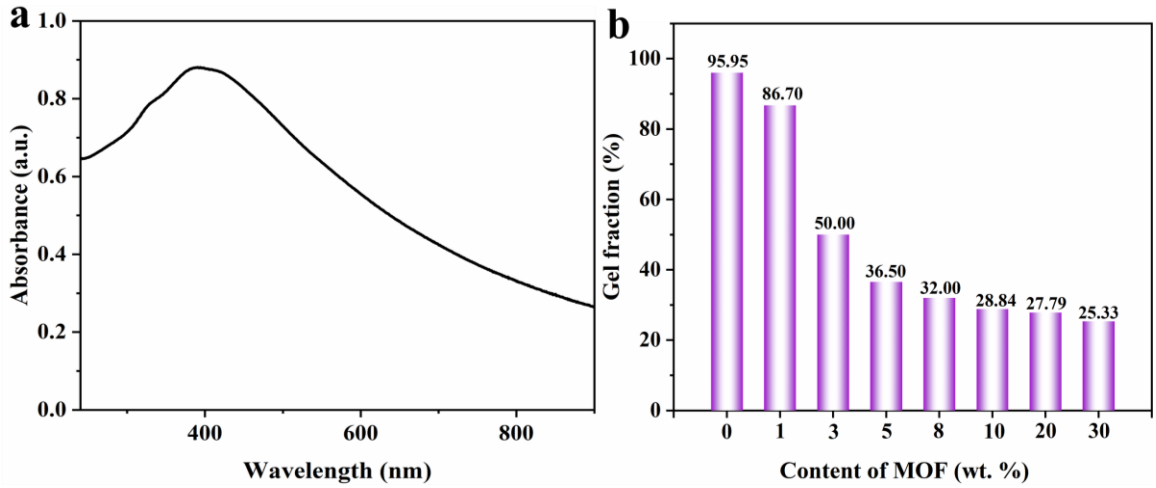

Figure S5. (a) UV/Vis absorption spectrum of the MIL-88A in water solution (10^{-4} mg/ml). (b) Plot of gel fraction vs. MOF content for LCE-MOF actuators (obtained by removal of uncrosslinked LCE chains in THF 20 ml solution at 40 ºC, repeated three times before drying).

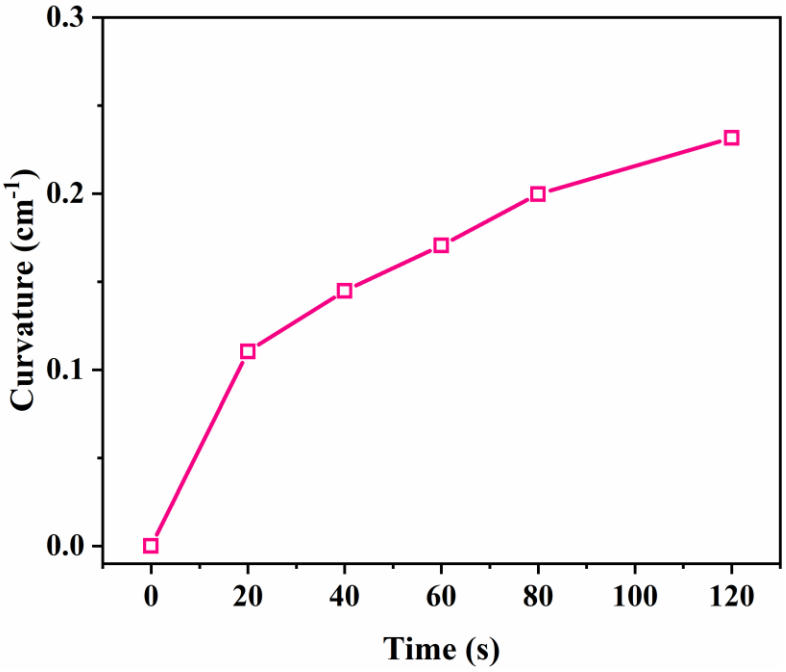

Figure S6. Uncrosslinked LCE-MOF20 film bending angle vs. time. (the inset photos showing the asymmetric bending of LCE-MOF20 film)

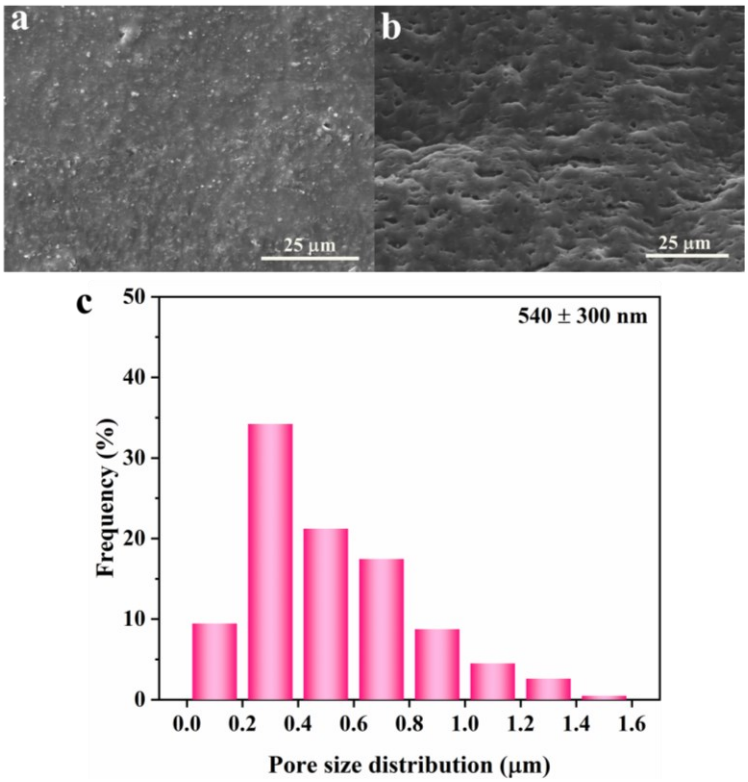

Figure S7. (a) and (b) SEM images showing surface morphology of LCE-MOF20 film before and after acid etching. (c) Pore size distribution of the LCE-MOF20 film etched for 6 h at room temperature.

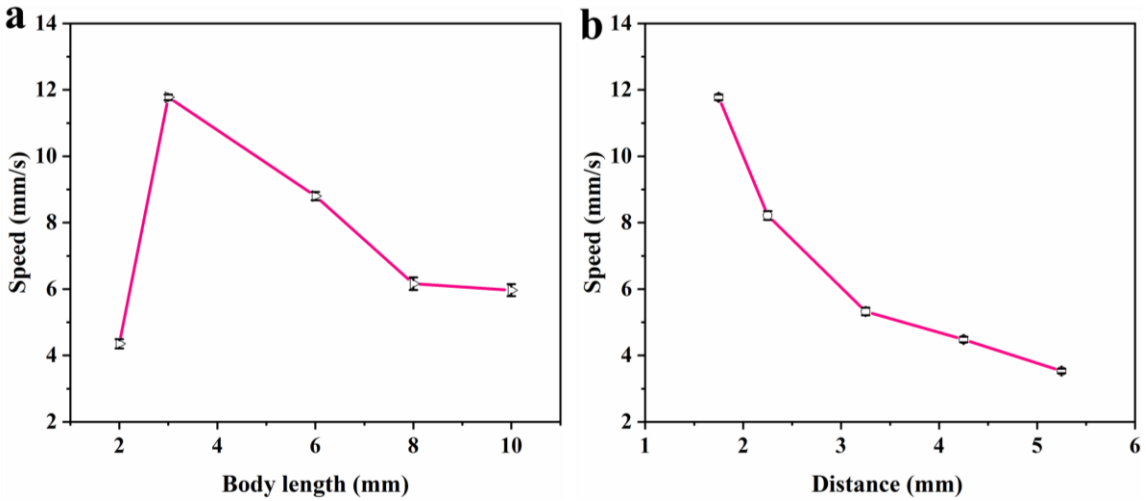

Figure S8. Speed of swimming as function of body length (a) and distance (b) (body length, 3 mm) between navigator and magnet.

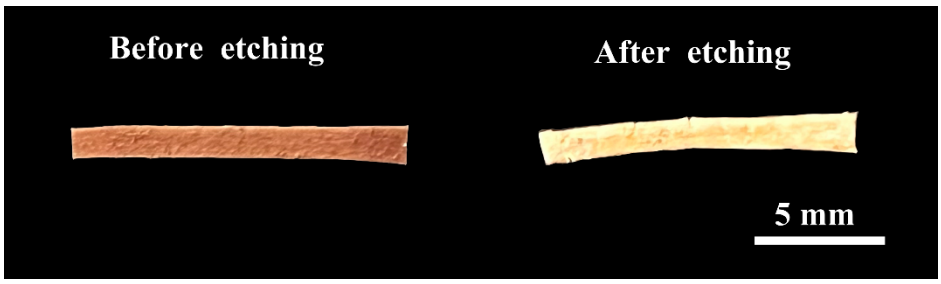

Figure S9. Photos showing appearance of LCE-MOF20 samples prepared without UV photo-crosslinking before and after etching.

Movie Captions

Movie S1. The motion of an LCE-MOF20 actuator at dry state and swollen state movement directed by magnet. The distance between the actuator and magnet is 1.75 mm. Maintaining the relative motion between the actuator and the magnet at 0.

Movie S2. The Swimming of the dry actuator in multiple directions guided by magnet, tracing shapes of “S”, round and “zigzag”. Maintaining the relative motion between the actuator and the magnet at 0.

Movie S3. Light-driven locomotion of an LCE-MOF20 before etching or after etching microwalker through cycles of arching-up (light-on) and flattening-down (light-off) (Light intensity: 3 $W \cdot cm^{-2}$, light on 2s /off 8s).